UNIVERSIDAD NACIONAL AUTÓNOMA
DE MÉXICO

POSGRADO EN ASTROFÍSICA
ASTROFÍSICA TEÓRICA

Numerical simulations of structured Short/Long Gamma Ray Bursts and their off-axis emission

T E S I S

QUE PARA OPTAR EL TÍTULO DE:

Doctor en Ciencias (Astrofísica)

PRESENTA:

Gerardo Urrutia Sánchez

TUTOR

Dr. Fabio De Colle
Instituto de Ciencias Nucleares

Ciudad de México, Enero 2023

Universidad Nacional Autónoma de México
UNAM
Biblioteca Central
Dirección General de Bibliotecas de la UNAM

UNAM – Dirección General de Bibliotecas
Tesis Digitales
Restricciones de uso

DERECHOS RESERVADOS ©
PROHIBIDA SU REPRODUCCIÓN TOTAL O PARCIAL

Todo el material contenido en esta tesis esta protegido por la Ley Federal del Derecho de Autor (LFDA) de los Estados Unidos Mexicanos (México).

El uso de imágenes, fragmentos de videos, y demás material que sea objeto de protección de los derechos de autor, será exclusivamente para fines educativos e informativos y deberá citar la fuente donde la obtuvo mencionando el autor o autores. Cualquier uso distinto como el lucro, reproducción, edición o modificación, será perseguido y sancionado por el respectivo titular de los Derechos de Autor.

print,"Hello World"*

Agradecimientos

Tiempo de supercómputo científico:

- DGTIC UNAM en la supercomputadora Miztli (proyecto LANCAD-UNAM-DGTIC-281).

Financiamientos Recibidos

- UNAM-PAPIIT proyectos AG100820 y IG100422
- Programa Nacional de Becas de Doctorado de CONACyT con el número de Becario 742744.

Reconocimiento a personas:

- Agradezco mucho el apoyo del Dr. Fabio De Colle, mi director de tesis, quien desde la maestría dedicó mucho tiempo para mi formación. Las discusiones científicas con Fabio son las más divertidas. Además de su amabilidad, tiene la habilidad de explicar de forma sencilla los fenómenos más complejos. Agradezco su paciencia y sobre todo su disposición para desarrollar e impulsar el trabajo contenido en esta tesis.
- A los miembros de mi comité académico por estar al tanto de mi formación durante el doctorado: Dr. Diego López-Cámara y Dr. Alan Watson.
- Mi agradecimiento a los sinodales por dedicar tiempo a la revisión de mi tesis y aportar con valiosos comentarios: Dr. Yuri Cavecchi, Dr. Aldo Batta, Dr. Simone Dichiara, Dr. Diego López-Cámara y Dra. Rosa Becerra.
- A los profesores del grupo de Astrofísica de Altas Energías, quienes mantuvieron activo tanto el journal club como los seminarios muy interesantes donde también he aprendido mucho: Rosa Becerra, Fabio De Colle, Diego López-Cámara, y Enrique Moreno. También a mis compañeros y amigos: Felipe

Vargas, Rogelio Medina, Leonardo García, Minerva Muñoz, y Ana Juárez quien contribuyó mucho a mi curso en la facultad.

- A los profesores del grupo de astro-plasmas del ICN-UNAM.
- A Bertha Vázquez, secretaria del posgrado en Astrofísica por su invaluable apoyo en todos los procesos burocráticos y por permitirme participar muchas veces en su carpa de la noche de las estrellas, claro, no poniendo de lado la recomendación de Rosa.
- A los colaboradores de los proyectos contenidos en esta tesis. Artículo contenido en el capítulo 2: Ariadna Murguía-Berthier y Enrico Ramírez-Ruíz. Artículo contenido en el capítulo 3: Diego López Cámara. Artículo contenido en el capítulo 4: Ramandeep Gill y Jonathan Granot. Artículo contenido en el capítulo 5: Claudia Moreno y Michelle Zanollin.
- El apoyo de mis amigos fuera de la academia: A Lizbeth Cervantes, Carlos Hernández, Asael Porfirio y muy especialmente agradezco a mi amigo Enrique Hernández.
- Por último, no menos importante, el apoyo y cariño infinito de mi familia, a quienes dedico este trabajo: Magda y Gerardo mis padres, Judith y Moisés mis hermanos, Gisel y Samuel mis sobrinos.

Resumen

Los destellos de rayos gamma (GRBs, por sus siglas en inglés) son eventos transitorios muy luminosos, con una luminosidad isotrópica $L_{\rm GRB} \sim 10^{50} - 10^{54}$ erg s^{-1} (e.g., Kumar & Zhang, 2015). Los GRBs son clasificados de acuerdo a su duración (e.g., Salafia & Ghirlanda, 2022), la cual depende fuertemente del progenitor. Los destellos de rayos gamma cortos (SGRBs) tienen una duración típica $t \lesssim 2$ s mientras que los largos (LGRBs) $t \gtrsim 2$ s. Los SGRBs están asociados a la fusión de dos estrellas de neutrones (o una fusión de estrella de neutrones con agujero negro) y los LGRBs al colapso de estrellas masivas (e.g., Levan et al., 2016). La emisión de un GRB es producida por la disipación de energía de un jet relativista que se mueve con factores de Lorentz $\Gamma_j \sim 100 - 500$ (e.g., Kumar & Zhang, 2015). La radiación gamma emitida durante los primeros segundos es llamada *la prompt emission* (e.g., Perley et al., 2014). También, los GRBs tienen una segunda etapa de emisión llamada el *afterglow*. Esta se observa días e incluso años después de la *prompt emission*, debido a que el jet continúa expandiendose en el medio interestelar. Como consecuencia de su desaceleración y la radiación de sincrotrón (Sari et al., 1998), el *afterglow* es emitido en un espectro multifrecuencia que se observa desde rayos-X hasta radiofrecuencias (e.g., Perley et al., 2014).

En agosto de 2017 se detectó el GRB 170817A que es el más cercano a nuestra galaxia, a una distancia de ~ 40 Mpc (Margutti et al., 2018; Troja et al., 2018; Mooley et al., 2018). Este, es el primer GRB corto visto *off-axis* y también el primero en detectarse conjuntamente con la emisión de ondas gravitacionales (GW) producidas por la fusión de dos estrellas de neutrones (Abbott et al., 2017b; Margutti et al., 2018; Troja et al., 2018; Mooley et al., 2018; Granot et al., 2018; Lazzati et al., 2018). El evento GRB/GW 170817A cambió el paradigma sobre la dinámica de los GRBs. El modelo convencional del jet top-hat fué insuficiente para explicar las observaciones de dicho GRB. Sin embargo, modelos de jets estructurados han explicado exitosamente las observaciones *off-axis* del GRB 170817A (e.g., Lazzati et al., 2018; Mooley et al., 2018; Granot et al., 2018; Makhathini et al., 2020; Urrutia et al., 2021). La estructura del jet está conectada con los procesos dinámicos que sufre el jet desde su lanzamiento en el motor central hasta su propagación en el

medio externo. Una nueva generación de telescopios como el "Vera Rubin Observatory" (Gao et al., 2022a) podrán detectar contra-partes en óptico de GRBs *off-axis*, y proporcionarnos información sobre la estructura de estos jets. Estudiar la dinámica y los procesos radiativos asociados a jets estructurados puede ayudarnos a interpretar futuras observaciones y a entender el comportamiento físico de los GRBs.

Esta tesis está enfocada en el estudio numérico de jets estructurados. La simulaciones se hicieron por medio del código *Mezcal* (De Colle et al., 2012a), el cual resuelve las ecuaciones de la hidrodinámica relativista. Se estudió la propagación de jets estructurados en el contexto de GRBs cortos y largos. La evolución del jet se siguió dentro y fuera del ambiente del progenitor (es decir, el viento empujado por neutrinos en el caso de GRBs cortos o la estrella progenitora en el caso de GRBs largos). Se realizaron simulaciones SRHD en tres dimensiones para estudiar los primeros segundos de propagación del jet estructurado para long GRBs. También, se realizaron simulaciones numéricas SRHD en dos dimensiones (axisimétricas) de jets estructuradas en el contexto de la fase *afterglow*. Los datos arrojados en cada simulación fueron usados para estudiar la evolución de la estructura del jet a través de su distribución angular de energía y velocidad. También se obtuvo la radiación del *afterglow* en radio frecuencias y se calculó la señal en ondas gravitacionales producida por los jets mismos.

En estos estudios encontramos que, tanto para SGRBs como para LGRBs, la estructura inicial del jet y la estructura del medio alrededor del motor central juegan un papel importante en la dinámica. Cuando el medio ambiente es poco denso, la estructura inicial del jet se preserva (parcialmente). Por otro lado, cuando el medio es muy denso, la estructura inicial del jet no se preserva y la interacción con el medio determina su estructura final. La propagación del jet es regulada por los parámetros iniciales del jet tales como su luminosidad L_j, tiempo de inyección t_j, factor de Lorentz inicial Γ_j y el ángulo de apertura del jet θ_j. En la mayoría de los casos, la estructura final del jet tiene una dependencia angular que sigue una ley de potencia. La estructura de los jets determina la forma de las curvas de luz *off-axis* de la radiación *afterglow*. Esto implica que a partir de observaciones *off-axis* se puede inferir la estructura del jet y su dinámica.

El jet se acelera cuando sale de la estrella, hasta que, alrededor de los 300 segundos de evolución, su aceleración termina, el jet entra en una fase de expansión libre y su estructura se mantiene inalterada. Por otro lado, nuestras simulaciones a grandes escalas muestran que, en la fase de desaceleración, la estructura del jet cambia abruptamente durante su evolución y no preserva su estructura inicial. Esto implica que despreciar la expansión lateral y considerar una estructura constante como función del tiempo, como se ha hecho en la mayoría de los trabajos publicados, no es una aproximación válida y puede llevar a conclusiones equivocadas.

Durante la fase de desaceleración, las simulaciones numéricas son necesarias para una descripción adecuada de la dinámica y de la radiación resultante.

Además de la radiación electromagnética, como parte de esta tesis he calculado la señal de ondas gravitacionales (GW) producida por los jets asociados a GRBs. Las GWs presentan picos característicos que están relacionados con etapas importantes de la dinámica del jet. El primer pico característico corresponde al tiempo en el que el jet se apaga. El segundo corresponde al tiempo cuando el jet sale de la estrella progenitora. Finalmente, el tercer pico es observado cuando el jet alcanza su máxima aceleración. Dado que la radiación gravitacional depende de su velocidad y energía, se espera también otro pico cuando comience la etapa de desaceleración.

Nuestras estimaciones revelan que observatorios espaciales como el Deci-Hertz Interferometer Gravitational wave Observator (DECIGO) y el Big Bang Observer (BBO) podrán detectar señales de ondas gravitacionales producidas por GRBs hasta distancias de 1 Gpc (es decir, observarán GWs emitidas por decenas/cientos de GRBs por año). Entonces, futuras observaciones de GWs producidas por jets de GRBs nos permitirán conocer las propiedades del progenitor y del jet mientras se propaga a través del medio denso alrededor del progenitor (donde el medio es muy opaco y la radiación producida es despreciable). Esto implica que en un futuro cercano podremos tener medidas directas del jet y su interacción con el medio circundante del progenitor.

List of publications

- **Urrutia, G.**, De Colle, F., Moreno, C., Zanolin, M. Gravitational Waves from Long Gamma-Ray Bursts and Supernovae, MNRAS, Submitted, July 2022.

- **Urrutia, G.**, De Colle, F., & López-Cámara, D. Three-dimensional numerical simulations of structured GRB jets, MNRAS, Submitted, July 2022.

- **Urrutia, G.**, De Colle, F., Murguia-Berthier, A., Ramírez-Ruíz, E. What determines the structure of short gamma-ray burst jets? MNRAS, 503, 4363, 2021.

- Gill, R., Granot, J., De Colle, F., **Urrutia, G.** Numerical Simulations of an Initially Top-hat Jet and the Afterglow of GW170817/GRB170817A, ApJ, 883, 15, 2019.

Contents

Chapter 1

Introduction

1.1 General properties and dynamics of GRBs

Gamma-ray bursts (GRBs) are very luminous pulses of γ-radiation (Kumar & Zhang, 2015). GRBs are detected at cosmological distances (Gehrels et al., 2009; Mészáros & Gehrels, 2012) and are distributed isotropically in the sky (Mészáros et al., 2000). The observed gamma radiation lasts a few seconds ($0.1 \lesssim t \lesssim 100\,\mathrm{s}$) and presents a high degree of variability (e.g., Perley et al., 2014). The GRB emission is produced by a relativistic jet which dissipates its kinetic energy. This relativistic jet has a Lorentz factor $\Gamma_j \gtrsim 100$ and a range of isotropic energies $E_{\mathrm{iso}} \sim 10^{50} - 10^{54}$ erg (Kumar & Zhang, 2015). The GRB phenomenon is not only associated with gamma radiation. Once the jet expansion reaches large scales ($r > 10^{16}\,\mathrm{cm}$, far away from the central engine), its deceleration produces a bright *afterglow* (Frail et al., 1997; Sari et al., 1998; Granot & Sari, 2002). This emission is detected as a multi-frequency spectrum, from X-ray to radio frequencies. The afterglow radiation can be observed since days to years after the γ-radiation (e.g., Perley et al., 2014), and is usually modelled as synchrotron radiation.

Two kind of GRB progenitors have been confirmed. The collapse of massive stars produces Type Ic supernovae (e.g., Frail et al., 1997) and, less frequently, a long GRB (LGRB) whose gamma emission has a typical duration $t \gtrsim 2\,\mathrm{s}$. On the other hand, neutron star mergers produce short[1] GRBs (SGRBs) whose typical emission lasts $t \lesssim 2$ s (Abbott et al., 2017b). Studies of the GRB population have revealed variations in their luminosity and duration. For example, a jet with a short duration and low luminosity ($L_{\mathrm{iso}} \lesssim 10^{50}\,\mathrm{erg\ s^{-1}}$), ejected from the magnetosphere of a neutron star, could explain the population of *soft gamma repeaters*.

[1] Short GRBs can also be produced by a merger of a neutron star with a black hole (e.g., Salafia & Ghirlanda, 2022).

Long duration, low luminosity, and possibly failed jets can originate *low luminosity GRBs* (e.g., Levan et al., 2013). In addition, very long and luminous GRBs are associated to tidal disruption events (see Levan et al., 2013, for more details about GRB progenitors). Finally, observations of early afterglow emission reveal a re-brightening and variability, explained as a change in the central engine or magnetic field fluctuations (Becerra et al., 2019, 2021).

The GRB activity is classified in two main stages based on the energy of the radiation observed (Mészáros & Gehrels, 2012; Kumar & Zhang, 2015). During the *prompt* emission ($r \gtrsim 10^{13}$ cm), gamma radiation is observed, accompanied by hard X-rays in some cases. During the *afterglow* emission ($r \gtrsim 10^{16}$ cm), a multi-wavelength spectrum, ranging from X-rays to radio, is observed. This phase is explained through the synchrotron emission of a relativistic jet. In the following, I describe the jet evolution in more detail.

The gamma radiation (in a few cases hard x-rays) is produced once the jet breaks out from the wind or from the massive star progenitor, and becomes optically thin, at $10^{13} \lesssim r \lesssim 10^{16}$ cm. This gamma radiation is explained by synchrotron and photospheric emission (e.g., Nakar, 2007; Berger, 2014; Gottlieb et al., 2018b). The variability in the gamma-ray light curves is possibly produced by internal shocks between several working surfaces of the jet. In the context of LGRBs, at the central engine, the cooling of the accretion disc produces hydrodynamic instabilities that could produce variability in the jet luminosity (Taylor et al., 2011; Batta & Lee, 2013).

1.2 Jet launching

The jet is launched from an accretion disk/compact object system (e.g., Salafia & Ghirlanda, 2022) called the "central engine" (see Figure 1.1). In the case of SGRBs, the jet results from a binary neutron star merger (Abbott et al., 2017b) or the merger of neutron star with a black hole. During the merger, a gravitational wave signal is emitted. After the merger, the debris create a toroidal structure (Rosswog et al., 2003; Rezzolla et al., 2011). Due to a large neutron densities, an intense flux of neutrinos is created, pushing the surrounding material and resulting into a strong wind (Rosswog & Ramirez-Ruiz, 2002a; Lee & Ramirez-Ruiz, 2007; Perego et al., 2014). The jet is probably launched by the Blandford & Znajek (1977) mechanism after the collapse of the remnant neutron star to a black hole. The wind from the accretion disc, the magnetic field of the compact object and the rotation of the central engine determine the initial jet structure (e.g., Kathirgamaraju et al., 2017).

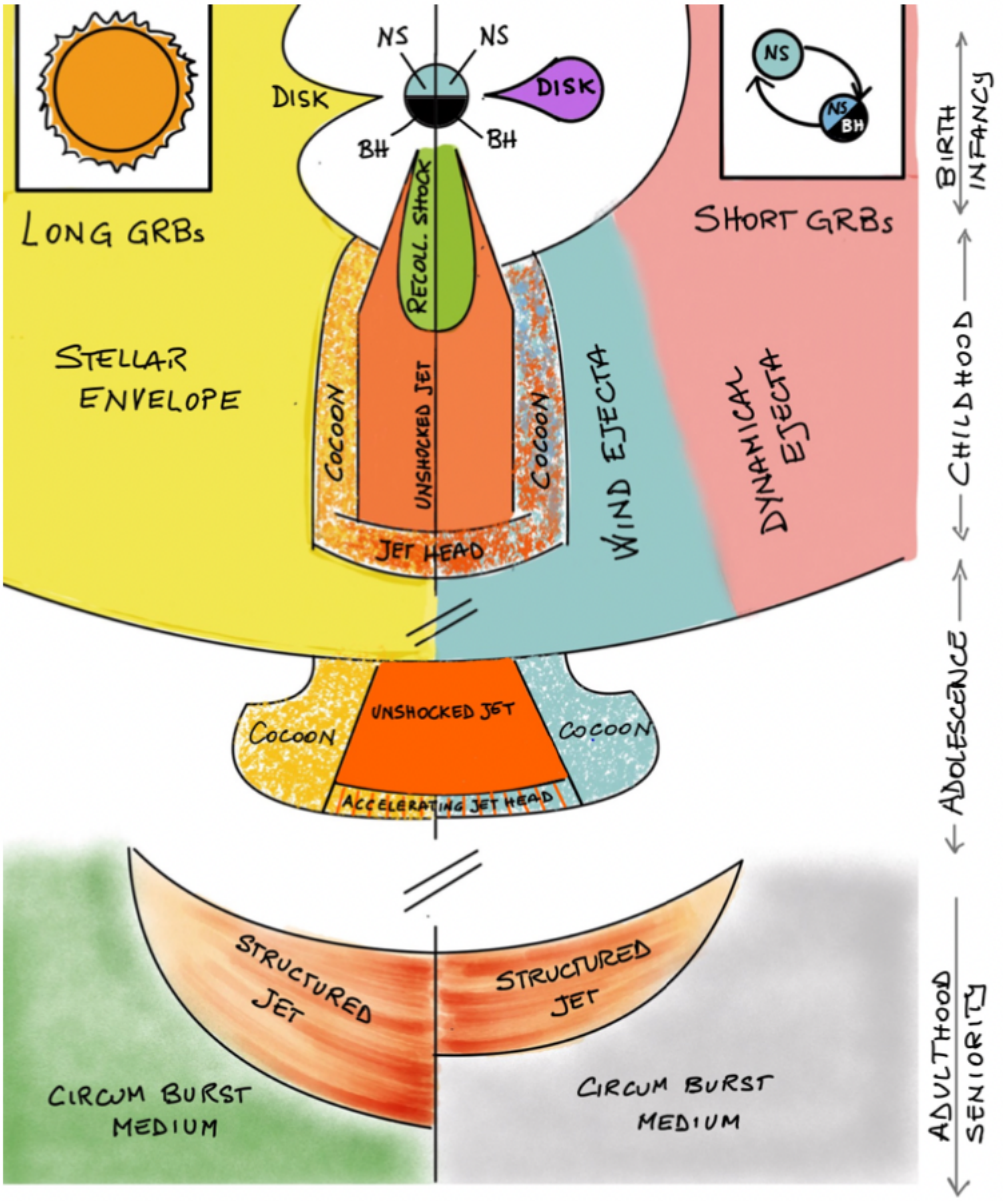

Figure 1.1: Scheme (not to scale) of the evolution of long and short GRBs (taken from Salafia & Ghirlanda 2022).

In the case of LGRBs, the compact object is formed during the collapse of a pre-supernova massive star progenitor (e.g., Frail et al., 1997; Kumar & Zhang, 2015; Mészáros & Gehrels, 2012). While there is strong evidence of the association of LGRBs with broad line, type Ic supernovae, it is not clear if the supernova appears before or after the jet has been launched (see De Colle et al., 2021, for a more detailed discussion). As in the SGRB case, the LGRB initial jet structure is determined by the central engine. Nevertheless, in this case, the jet starts its propagation in the massive star progenitor, which is much denser than the environment of neutron star mergers. (e.g., Morsony et al., 2007; López-Cámara et al., 2013, 2016).

In the following sections, I will describe the main properties of each stage of the GRB evolution.

1.3 Jets propagating through the central engine environment

From this point on, I will assume that the jet has been previously launched and reaches $r \sim 10^8$ cm nearly unperturbed (see for example, Murguia-Berthier et al., 2021a; Lazzati et al., 2021; Pavan et al., 2021). Then, the propagation of the jet through the central engine environment refers to its propagation in the spatial range $10^8 \lesssim r \lesssim 10^{11}$ cm.

In the case of SGRBs, the jet starts its propagation within a neutrino driven wind (NDW), which is the result of a flux of very energetic neutrinos produced mainly in the accretion disk. The cross section of these neutrinos depends strongly on their energy. Neutrinos deposit energy in the region around the neutron stars and drive a wind formed by the debris of the merger. (e.g., Murguia-Berthier et al., 2014, 2017a; Pavan et al., 2021). The shape of the wind modifies the jet structure. Therefore, the final structure of the jet is defined by the wind parameters such as, the density of the wind ρ_w, mass loss rate $\dot{M}$, wind velocity β_w (Murguia-Berthier et al., 2021a) in combination with the initial jet parameters, such as the jet luminosity L_j, the injection time t_j, the Lorentz Factor Γ_j and the jet opening angle θ_j.

In both, SGRBs and LGRBs, radiation emitted in the first seconds of the jet propagation will not be detectable since it occurs in an optically thick environment (nearby the neutron star merger or inside the stellar progenitor), because the progenitor (the environment of the neutron star merger or the massive stellar progenitor) is optically thick. The first detectable radiation is produced when the jet breaks out of these environments. In addition, there are other components launched from the progenitor that could emit radiation: the dynamical ejecta in the case of SGRBs, or the supernova in the case of LGRBs, whose emission can be detected once the surrounding material becomes optically thin.

1.3.1 Special relativistic hydrodynamics equations

GRB jets are a relativistic fluid described by the special relativistic hydrodynamics equations (SRHD)[2]. In this section, we describe the SRHD equations.

The special relativistic hydrodynamics (SRHD) equations describe the conservation of rest mass density $D = \rho\Gamma$, momentum $\vec{S} = Dh\Gamma\vec{v}$ and energy $e = Dh\Gamma c^2 - p - Dc^2$ for a relativistic fluid with Lorentz Factor $\Gamma = (1-\beta^2)^{-1/2}$. In conservative form, the SRHD equations are:

$$\frac{\partial D}{\partial t} + \nabla\cdot(D\vec{v}) = 0\,, \tag{1.1}$$

$$\frac{\partial \vec{S}}{\partial t} + \nabla\cdot(\vec{S}\vec{v} + pI) = 0\,, \tag{1.2}$$

$$\frac{\partial \tau}{\partial t} + \nabla\cdot(e\vec{v} + p\vec{v}) = 0\,, \tag{1.3}$$

being p the thermal pressure, ρ the fluid density, h the specific enthalpy, c the speed of light and $\vec{v} = \vec{\beta}c$ the velocity of the fluid[3]. The physical units used for this thesis are centimetre–gram–second system (cgs), then the units of density $[\rho] = \mathrm{g\ cm^{-3}}$, pressure $[p] = \mathrm{g\ cm^{-1}\ s^{-2}}$, the velocity and speed of light $[v] = [c] = \mathrm{cm\ s^{-1}}$. The Lorentz factor and specific enthalpy (defined in section 1.3.2) are non-dimensional quantities.

The system of equations (1.1)-(1.3) is closed by the equation of state $e = e(p,\rho)$. For example, for an ideal gas, $e = p/(\gamma-1)$. Then, the specific enthalpy h is defined as

$$\rho h = \rho + \frac{p\gamma}{(\gamma-1)\,c^2}\,, \tag{1.4}$$

being γ the specific heat ratio. As the jets will be treated as a relativistic fluid, the solution of the hydrodynamics equations can be solved by numerical methods, in particular in this thesis I use the *Mezcal* code (De Colle et al. 2012a, see Appendix A).

1.3.2 The jet head and terminal velocity

Jets move with very high velocities with respect to the environment. Therefore, the interaction between the collimated flow and the external media produces a strong shock. The post-shock density, pressure and velocities are related to the pre-shock values (in the shock system of reference) by the Taub (1948) adiabats

[2] In this thesis, GRB jets are taken as a non magnetised fluid.

[3] If $\beta \ll 1$ the system of equations (1.1)-(1.2) reduces to the Euler equations.

(i.e., the relativistic shock conditions):

$$\rho_1\Gamma_1\beta_1 = \rho_2\Gamma_2\beta_2 \,, \tag{1.5}$$

$$\rho_1 h_1\Gamma_1^2\beta_1^2c^2 + p_1 = \rho_2 h_2\Gamma_2^2\beta_2^2c^2 + p_2 \,, \tag{1.6}$$

$$\rho_1 h_1\Gamma_1^2\beta_1 = \rho_2 h_2\Gamma_2^2\beta_2 \,, \tag{1.7}$$

being ρ the density, p the thermal pressure, v the velocity of the fluid, c the speed of light and Γ the Lorentz factor. Here, sub-index 1 denotes the unshocked fluid (upstream), while sub-index 2 corresponds to the shocked fluid (downstream). The specific enthalpy is defined as $h_i = 1 + \gamma p_i/(\gamma - 1)\rho_i c^2$, with $i = 1, 2$, and γ the specific heat ratio.

The Taub conditions can be used to determine the jet velocity while it moves through the dense environment of the central engine, and when the jet is accelerated through the low-density medium at larger distances.

From the Taub conditions, the momentum jump condition in the laboratory frame can be rewritten in the system the reference of the shock that in this case is the jet head. Now, the upstream fluid is denoted as the fluid of the jet $_1 \rightarrow_j$ and the downstream fluid as $_2 \rightarrow_h$. As a consequence, in the system of reference of the shock, the downstream velocity $u_2 = \Gamma_2\beta_2 \rightarrow \Gamma_h\beta_h$ that modify the right side of the momentum equation. For the left side, taking the Lorentz transformation of the upstream velocity that depends of shock velocity $u_1 \rightarrow u_j = \Gamma_j\beta_j = \Gamma_j\Gamma_h(\beta_j - \beta_h)$. Then the momentum equation is modified as

$$\rho_j h_j\Gamma_j^2\Gamma_h^2(\beta_j - \beta_h)^2c^2 + p_j = \rho_a h_a\Gamma_h^2\beta_h^2c^2 + p_a \,, \tag{1.8}$$

where the sub-indexes $_j$ and $_h$ refer to the jet and head velocities. In strong shocks $p_a \ll \rho_a c^2$, which implies $p_a \rightarrow 0$ and $h_a \rightarrow 1$. Then

$$\rho_j h_j\Gamma_j^2\Gamma_h^2(\beta_j - \beta_h)^2c^2 + p_j = \rho_a\Gamma_h^2\beta_h^2c^2 \,. \tag{1.9}$$

In general, the kinetic term $\rho_j h_j\Gamma_j^2\Gamma_h^2$ is dominant with respect to p_j. Then, we can simplify the last equation obtaining

$$\rho_j h_j\Gamma_j^2(\beta_j - \beta_h)^2 = \rho_a\beta_h^2 \,. \tag{1.10}$$

Defining $\widetilde{L} \equiv \rho_j h_j\Gamma_j^2/\rho_a$ (Bromberg et al., 2011b) and taking the square root on both sides of the equation, we obtain the velocity of the jet head as,

$$\beta_h = \frac{\beta_j}{1 + \widetilde{L}^{-1/2}} \,. \tag{1.11}$$

In the case of large densities of the ambient medium (i.e. $\widetilde{L} \ll 1$), the velocity of the jet head is $\beta_h \ll \beta_j$. In the case of low densities (i.e. $\widetilde{L} \gg 1$), the velocity of the jet head is $\beta_h \approx \beta_j$.

Once the jet breaks out from the dense environment, it starts accelerating through the low density environment. The expression of the terminal velocity is obtained from the Taub conditions:

$$\rho_j \Gamma_j v_j = \rho_a \Gamma_\infty v_\infty \,, \tag{1.12}$$

$$\Gamma_j^2 \rho_j v_j^2 h_j + p_j = \Gamma_\infty^2 \rho_a v_\infty^2 \,, \tag{1.13}$$

where the sub-indexes $_j$ and $_a$ indicate the jet and ambient medium material, and v_∞, Γ_∞ the terminal velocity and Lorentz factor, respectively. In this equations, the ambient medium is considered as a cold gas, i.e., $p_a \ll \rho_a c^2$. From the mass jump condition, the density of environment is described by $\rho_a = \Gamma_j \rho_j v_j / \Gamma_\infty v_\infty$. This expression is replaced in the momentum jump condition. By considering $v_j \approx v_\infty \approx c$ and Lorentz factor $\Gamma_j \rho_j v_j v_\infty \gg p_j$, it is possible to find a relation between Γ_∞ and Γ_j, this is, the terminal Lorentz factor as

$$\Gamma_\infty = h_j \Gamma_j \,. \tag{1.14}$$

1.3.3 Nature of the jet

Relativistic jets can be described mainly by the density ρ_j, pressure p_j and velocity $v_j = \sqrt{1 - 1/\Gamma_j^2}$. The Lorentz factor of the jet Γ_j, terminal Lorentz factor Γ_∞, and jet luminosity L_j are assumed as fixed quantities. The total energy density of the jet is given by,

$$e_j = \rho_j h_j \Gamma_j^2 c^2 - p_j - \rho_j \Gamma_j c^2 \,. \tag{1.15}$$

Jets can be kinetic- or thermal- energy dominated (Matsumoto & Masada, 2013). In the first case, they accelerate close the the central engine (in which case, most thermal energy will be quickly converted into kinetic energy), or they can be launched (and propagate) with a large amount of thermal energy (i.e., much larger than the kinetic component), and the acceleration can be negligible during the early evolutionary phases.

For pressure dominated jets (e.g., Matsumoto & Masada, 2013), the specific enthalpy in equation (1.15) plays an important role. By substituting the definition of specific enthalpy $h_j = 1 + 4p_j/\rho_j c^2$ in equation (1.15), we get

$$e_j = \rho_j \Gamma_j \left(\Gamma_j - 1\right) c^2 + p_j \left(4\Gamma_j - 1\right) \,. \tag{1.16}$$

The luminosity of the jet is given by,

$$L_j = \frac{dE_j}{dt} = \frac{d}{dt}\int_V e_j \, dV \, . \tag{1.17}$$

On the other hand, the luminosity of the jet can be described as

$$L_j = \Gamma_\infty \dot{M} c^2 = \Gamma_\infty c^2 \frac{d}{dt}\int_V \Gamma_j \rho_j \, dV = \frac{d}{dt}\int_V \Gamma_\infty \Gamma_j \rho_j c^2 \, dV \, , \tag{1.18}$$

being $M = \int_V \Gamma_j \rho_j dV$. To obtain an expression for the pressure, we consider $\Gamma_\infty \gg \Gamma_j$. By combining equations (1.17) and (1.18), the pressure reads

$$p_j = \frac{\rho_j c^2}{4}\left(\frac{\Gamma_\infty}{\Gamma_j} - 1\right) \, . \tag{1.19}$$

By taking a constant luminosity, the density of the jet ρ_j can be obtained by equation (1.18) as

$$L_j = \frac{d}{dt}\int_V \Gamma_\infty \Gamma_j \rho_j c^2 \, dV = \frac{d}{dt}\int_S \Gamma_\infty \Gamma_j \rho_j c^2 \, v_j dt dS \, , \tag{1.20}$$

therefore

$$\rho_j = \frac{L_j}{\Gamma_\infty \Gamma_j c^2 v_j S} \, , \tag{1.21}$$

being $S = \int dS$ the jet surface, which depends on the geometry of the jet, i.e. conical/spherical or cylindrical. Pressure dominated jets are considered for example in Lopez-Camara et al. (2009); López-Cámara et al. (2016); Harrison et al. (2018); Gottlieb et al. (2020c)

In kinetic dominated jets the pressure is negligible $P_j \ll 1$ (e.g., Matzner, 2003), which implies that the specific enthalpy $h_j \to 1$. Then the energy density (1.16) reduces to

$$e_j \approx \rho_j \Gamma_j \left(\Gamma_j - 1\right) c^2 \, , \tag{1.22}$$

and the luminosity is modified as

$$L_j = \frac{d}{dt}\int_S \rho_j \Gamma_j \left(\Gamma_j - 1\right) \, v_j dt dS \, , \tag{1.23}$$

then the density is given as

$$\rho_j = \frac{L_j}{\Gamma_j \left(\Gamma_j - 1\right) c^2 v_j S} \ . \tag{1.24}$$

The pressure is simply taken as a small quantity,

$$p_j \sim 10^{-10} \rho_j c^2 \ . \tag{1.25}$$

Kinetic dominated jets have been considered for example by Murguia-Berthier et al. (2014, 2017a); Matsumoto & Masada (2019); De Colle et al. (2018a,b); Urrutia et al. (2021); Murguia-Berthier et al. (2021a).

Since the density and pressure of the jet are derived directly from the total energy and the Taub conditions, these quantities can be modified by the presence of magnetic fields. However, in this thesis magnetic fields are not considered.

The dynamics of weekly magnetised jets has been studied for example by Komissarov et al. (2007); Mignone et al. (2009, 2013); Nathanail et al. (2020); Gottlieb et al. (2020b). Matematically, magnetic fields contributes to the total gas pressure in addition to thermal pressure $p_{\rm tot} = p_{\rm thermal} + p_{\rm magnetic}$, being the magnetic pressure $p_{\rm magnetic} = (B^2 + E^2)/8\pi$ and $\vec{E} = -\vec{v} \times \vec{E}$ (Mignone et al., 2009, 2013). As a consequence, the equation that contain the pressure will be modified as $p \rightarrow p_{\rm tot}$, i.e., the momentum (1.7), and energy (1.15) equation. In the context of GRBs, (Nathanail et al., 2020; Gottlieb et al., 2020b), the effect of magnetic field on the jet propagation is to modify the structure of the core of the jet due to the dissipation of magnetic energy. In addition, magnetic fields can lead to pinch and kink instabilities which can increase the amount of turbulence present in the system. The effect produced by magnetic field is left to future studies.

1.4 Decelerating phase

At a distance $r \gtrsim 10^{16}$ cm the jet head piles-up enough mass from the interstellar medium and it starts its deceleration stage (Sari et al., 1998; Granot & Sari, 2002; Zhang & MacFadyen, 2009; De Colle et al., 2012a; Mészáros & Gehrels, 2012; Kumar & Zhang, 2015). The self similar solution describing the deceleration of a relativistic blast wave was described by Blandford & McKee (1976). The cooling of electrons spiralling around magnetic field lines and accelerated by the blast wave produces the afterglow radiation (e.g., Sari et al., 1998). The multi-frequency afterglow emission is described by the standard synchrotron model (Sari et al., 1998; Granot & Sari, 2002) in different spectral shapes. In the case of *off-axis* GRBs, due to the cocoon

structure, the synchrotron emission observed off-axis is different from the on-axis observed emission (e.g. Lazzati et al., 2018; Mooley et al., 2018; Salafia, O. S. et al., 2020).

Several open questions about the GRB dynamics and emission can be answered by modelling GRBs using the relativistic hydrodynamics equations. In the next sections, I will describe the standard methods employed for GRB modelling.

1.4.1 Post-shock conditions

To find the jump conditions and the structure of the post/shock region (with respect to r) during the deceleration stages, we assume that radiative losses are negligible and the number of particles is conserved throughout the shock. The shocked gas is heated to relativistic temperatures (Thorne, 1973). This means that $\gamma_2 = 4/3$ and $h_2 \approx 4p_2/\rho_2 c^2$. On the other hand, in the upstream gas $\Gamma_1 \gg 1$ and $\beta_1 \approx 1$ and $h_1 \longrightarrow 1$. The jump conditions in the post/shock region (indicated by the sub-index $_{\rm ps}$) are related to the pre-shock values by

$$\Gamma_{\rm ps} = \frac{1}{\sqrt{2}}\Gamma_{\rm sh} , \tag{1.26}$$

$$\rho_{\rm ps} = \sqrt{8}\rho(r)\Gamma_{\rm sh} , \tag{1.27}$$

$$p_{\rm ps} = \frac{2}{3}\rho(r)c^2\Gamma_{\rm sh} . \tag{1.28}$$

Here, the unshocked medium can be stratified, i.e., $\rho(r) = \rho_0(r/r_0)^{-k}$, such that $\rho_0 = nm_p$, and $k = 0, 2$ corresponds to a constant density medium or a wind respectively. One important quantity is the energy of the shell which determines the time evolution of the Lorentz factor $\Gamma(t)$. The total energy of the shell is $E = \Gamma Mc^2$. The shell starts its deceleration stage when its ratio E/Γ is of order of the rest-frame energy of the mass accumulated from the environment. Since the shell mass is $dM = 4\pi r^2\rho(r)\Gamma dr$, the energy can be written as

$$dE = 4\pi\Gamma^2 c^2 r^2 \rho_0 \left(\frac{r}{r_0}\right)^{-k} dr . \tag{1.29}$$

By integrating this equation, we obtain the energy as $E \propto \Gamma^2(r/r_0)^{3-k}$. Assuming $r = ct$, the temporal evolution of Lorentz factor reduces to

$$\Gamma(t) \propto \left(\frac{t}{t_0}\right)^{-(3-k)/2} . \tag{1.30}$$

The jump conditions (1.26)-(1.28) are valid only at the shock front, while the post-shock region is non stratified for a static media and stratified for a stellar wind.

1.4.2 The Blandford & McKee (1976) solution

Our aim is to determine the radial structure of the shell behind its shock front. The ultra relativistic limit for the velocity is $v_{\rm sh}(t) = c(1-1/\Gamma_{\rm sh}^2)^{1/2} \approx c\left(1-1/2\Gamma_{\rm sh}^2\right)$, obtained by a Taylor expansion. Taking the temporal dependence of the Lorentz Factor (1.30), the shock radius is given by

$$r_{\rm sh}(t) = \int_0^t v_{\rm sh}(t')dt' \approx \int_0^t c\left(1-\frac{1}{2\Gamma_{\rm sh}^2(t)}\right)dt' = ct\left(1-\frac{1}{2(4-k)\Gamma_{\rm sh}^2}\right) . \tag{1.31}$$

In the last equation, once can observe that $r_s - ct = -ct/2(4-k)\Gamma_{\rm sh}^2$, which suggest a scaling relation $r_{\rm sh} - r = A(\chi)r_{\rm sh}/\Gamma_{\rm sh}^2$. Blandford & McKee (1976) found an expression for $A(\chi) = (\chi-1)/2(4-k)$, then,

$$r_{\rm sh} - r = \frac{\chi-1}{2(4-k)}\frac{r_{\rm sh}}{\Gamma_{\rm sh}^2} . \tag{1.32}$$

We note that the self-similar variable χ, is such that, when $\chi = 1$, the last equation $r_{\rm sh} = r$, the position r corresponds to the position of the shock $r_{\rm sh}$. By reordering the terms in this equation, it is possible to obtain the self-similar variable in terms of r and $r_{\rm sh}$, as

$$\chi = 1 + 2(4-k)\Gamma_{\rm sh}^2\left(1-\frac{r}{r_{\rm sh}}\right) . \tag{1.33}$$

The post-shock density, velocity and pressure are then a function of the self-similar variable χ, i.e.

$$\Gamma_{\rm ps}^2 = \frac{1}{2}\Gamma_{\rm sh}^2\chi^{-1}, \tag{1.34}$$

$$\rho_{\rm ps} = \sqrt{8}\rho(r)\Gamma_{\rm sh}\chi^{-(17-4k)/(12-3k)}, \tag{1.35}$$

$$p_{\rm ps} = \frac{2}{3}\rho(r)c^2\Gamma_{\rm sh}\chi^{-(17-2k)/(4-k)} . \tag{1.36}$$

The energy can be also determined by using this self-similar solution. As the shell energy is dominated by internal energy, and $e = \rho\Gamma_{\rm ps}(\Gamma_{\rm ps}-1)c^2 + (4\Gamma_{\rm ps}^2-1)p_{\rm ps} \approx 4\Gamma_{\rm ps}^2 p_{\rm ps}$. Then,

$$e = 4\Gamma_{\rm ps}p_{\rm ps} = 4\left(\frac{\Gamma_{\rm sh}^2}{2}g(\chi)\right)\left(\frac{2}{3}\rho(r)c^2\Gamma_{\rm sh}^2 f(\chi)\right) = \frac{4}{3}\rho(r)c^2\Gamma_{\rm sh}^4 g(\chi)h(\chi) , \tag{1.37}$$

being,

$$f(\chi) = \chi^{-1}, \tag{1.38}$$

$$g(\chi) = \chi^{-(17-4k)/(12-3k)}, \tag{1.39}$$

$$h(\chi) = \chi^{-(17-2k)/(4-k)} . \tag{1.40}$$

The total shell energy is obtained by integrating the specific energy over the volume, i.e., $E = \int 4\pi r^2 e\, dr$. This integral is computed by considering the following change of variable (see equation (1.33))

$$dr = -\frac{ct\, d\chi}{2(4-k)\Gamma_{\rm sh}^2} , \tag{1.41}$$

and assuming that the shell extends to $\chi \ll 1$. Then,

$$E = \int_0^{r_{\rm sh}} e\, 4\pi r^2 dr = -\frac{4}{3}\rho(r)c^5\Gamma_{\rm sh}^4 t^3 \int_{-\infty}^{1} \frac{g(\chi)f(\chi)d\chi}{2(4-k)\Gamma_{\rm sh}^2} = \frac{2}{12-3k}\Gamma_{\rm sh}^2\rho(r)c^5t^3\int_1^{\infty}\chi^{-\frac{17-4k}{12-3k}+1}d\chi , \tag{1.42}$$

which reduces to

$$E = \frac{8\pi\rho(r)c^5\Gamma_{\rm sh}^2 t^3}{17-4k} . \tag{1.43}$$

Then the Lorentz factor is

$$\Gamma_{\rm sh}^2 = \frac{(17-4k)E}{8\pi\rho(r)c^5t^3} . \tag{1.44}$$

For a stratified, $\rho(r) = \rho_0(r/r_0)^{-k}$ and $\Gamma_{\rm sh}^2 \propto t^{-(3-k)}$, thus, the time is,

$$t \approx \frac{R}{c} = \frac{1}{c}\left[\frac{(17-4k)E}{8\pi\rho_0 c^2\Gamma_{\rm sh}^2}\right]^{1/(3-k)} . \tag{1.45}$$

1.5 Afterglow Emission

The afterglow emission of GRBs is described by synchrotron radiation (Sari et al., 1998; Granot, 2005). Hereafter, I assume that Compton scattering is negligible. A fraction $\epsilon_{\rm B}$ of the proper energy density ends in the magnetic field, i.e. $B'^2/8\pi = \varepsilon_B e'$. The fraction of energy of accelerated electrons is denoted by ϵ_e. Assuming that Compton scattering is negligible implies that $\varepsilon_B \leq \varepsilon_e$. In the post-shock region, it is assumed that electrons are accelerated with a distribution that depends on Lorentz factor as $N(\Gamma_e) \propto \Gamma_e^{-p}$, for $\Gamma_e > \Gamma_m$.

The minimum Lorentz factor Γ_m is given by

$$\Gamma_m = \epsilon_e \left(\frac{p-2}{p-1}\right) \frac{m_p}{m_e} \Gamma \ , \tag{1.46}$$

where Γ is the Lorentz factor of the blast wave producing the emission. The spectral index typically has a value of $p \simeq 2.2 - 2.5$ (e.g., Makhathini et al., 2020). The magnetic filed strength at the fluid frame is given by

$$B = (32\pi m_p \varepsilon_B n)^{1/2} \Gamma c \ . \tag{1.47}$$

The blast wave amplifies the magnetic field of the external media environment, and the magnetic field lines acquire a random orientation. As a consequence, the electron population is randomly oriented with the Lorentz factor $\Gamma \gg 1$. The power spectrum [$\mathrm{Hz}^{-1}\mathrm{s}^{-1}$] in the observer frame is given by $P(\Gamma_e) = \frac{4}{3}\sigma_T c \Gamma^2 \Gamma_e^2 B^2/8\pi$, and the frequency $\nu(\Gamma_e) = \Gamma\Gamma_e q_e B/2\pi m_e c$, being Γ the Lorentz factor of the fluid. The spectral characteristic peak is given by,

$$P_{\max} \approx \frac{P(\Gamma_e)}{\nu(\Gamma_e)} = \frac{m_e c^2 \sigma_T}{3 q_e} \Gamma B \ , \tag{1.48}$$

which is independent of Γ_e. By combining expressions (1.47) and (1.48) we can compute the characteristic Lorentz factor of cooling electrons as

$$\Gamma_c = \frac{3 m_e}{16 \varepsilon_B \sigma_T m_p c} \frac{1}{\Gamma^3 n t} \ . \tag{1.49}$$

The spectral shape presents two cases: fast cooling for $\Gamma_m > \Gamma_c$ and slow cooling for $\Gamma_m < \Gamma_c$ (Sari et al., 1998; Granot & Sari, 2002). The total number of swept-up electrons in the post shock fluid is $N_e = 4\pi R^3 n/3$. The maximum flux is given by the frequency $\nu_m = \nu(\Gamma_m)$. The observed peak flux at distance D from the source is $F_{\nu,\max} = N_e P_{\nu,\max}/4\pi D^2$. In the fast cooling regime, the spectrum is,

$$F_\nu = \begin{cases} (\nu/\nu_c)^{1/3} F_{\nu,\max} & \text{if} \quad \nu_c > \nu \ , \\ (\nu/\nu_c)^{-1/2} F_{\nu,\max} & \text{if} \quad \nu_m > \nu > \nu_c \ , \\ (\nu_m/\nu_c)^{-1/2} (\nu/\nu_m)^{-p/2} F_{\nu,\max} & \text{if} \quad \nu > \nu_m \ . \end{cases} \tag{1.50}$$

The slow cooling case (used in this thesis) corresponds to $\Gamma_c > \Gamma_m$, due to the fast cooling is used in very early jet emission. Then, only electrons with $\Gamma_e > \Gamma_c$ cool in the time t. The spectrum in this case is

$$F_\nu = \begin{cases} (\nu/\nu_m)^{1/3} F_{\nu,\max}, & \text{if} \quad \nu_m > \nu \ , \\ (\nu/\nu_m)^{-(p-1)/2} F_{\nu,\max}, & \text{if} \quad \nu_c > \nu > \nu_m \ , \\ (\nu_c/\nu_m)^{-(p-1)/2} (\nu/\nu_c)^{-p/2} F_{\nu,\max} & \text{if} \quad \nu > \nu_c \ . \end{cases} \tag{1.51}$$

The evolution of the shock front obtained from the numerical simulations provides information on the energy $E(t)$, the position of the shock front $R_{\rm sh}(t)$, the Lorentz factor $\Gamma(t)$ and density $\rho(t)$ of the emitting electrons, which are necessary to compute the synchrotron radiation. In this thesis, we consider only the case of slow cooling ($\Gamma_c > \Gamma_m$). We use the power-law spectra (PLS) described above (see, Granot & Sari, 2002), labeling the expressions (1.51) as **PLS D** for $F_\nu \propto \nu^{1/3}$ if $\nu_m > \nu$, **PLS G** for $F_\nu \propto \nu^{(1-p)/2}$ if $\nu_c > \nu > \nu_m$, and **PLS H** for $F_\nu \propto \nu^{-p/2}$ if $\nu > \nu_c$, respectively.

The emission of a decelerating blast wave described by the Blandford & McKee (1976) solution is given (in the case of a uniform medium) by

$$F_{\nu,\rm PLS\,D}(t) = 27.9 \frac{p-1}{3p-1} (1+z)^{5/6} \bar{\varepsilon_e}^{-2/3} \varepsilon_B^{1/3} n_0^{1/2} E_{52}^{5/6} t_{\rm days}^{1/2} \frac{\nu_{14}^{1/3}}{d_{L28}^2} \ , \tag{1.52}$$

$$F_{\nu,\rm PLS\,G}(t) = 0.461(p-0.04) e^{2.53p} (1+z)^{(3+p)/4} \bar{\varepsilon_e}^{p-1} \varepsilon_B^{(1+p)/4} n_0^{1/2} E_{52}^{(3+p)/4} t_{\rm days}^{3(1-p)/4} \frac{\nu_{14}^{(1-p)/2}}{d_{L28}^2} \ , \tag{1.53}$$

$$F_{\nu,\rm PLS\,H}(t) = 0.855(p-0.98) e^{1.95p} (1+z)^{(2+p)/4} \bar{\varepsilon_e}^{p-1} \varepsilon_B^{(p-2)/4} E_{52}^{(2+p)/4} t_{\rm days}^{2-3p)/4} \frac{\nu_{14}^{-p/2}}{d_{L28}^2} \ . \tag{1.54}$$

In this thesis, I used these three spectral regions for the afterglow estimation.

1.6 Structured jets

The jet structure is the lateral morphology present after the jet is launched from the central engine and eventually modified during its propagation. The structure of the jet is defined by its energy, pressure, density and velocity as a function of angle, and by their stratification in the post-shock region. The dynamics of structured jets has been studied by solving the hydrodynamics through numerical simulations, or by analytical works, i.e. by using the Blandford & McKee (1976) solution to describe different slices of the expanding blast

wave.

The study of structured jets is motivated by observations of afterglow radiation. Before the detection of GRB 170817A, this technique was focused on the prediction of GRBs viewed slightly *off-axis* or on orphan afterglows (e.g., Granot, 2005; Granot & Ramirez-Ruiz, 2010). Several authors have studied the jet structure at small scales $\sim 10^{10}$ cm (e.g., Mooley et al., 2018; Murguia-Berthier et al., 2021a; Lazzati et al., 2018; Duffell et al., 2015; Morsony et al., 2007). All these works (except Salafia, O. S. et al., 2020; Wu & MacFadyen, 2019) assume that the central engine launches a collimated *top-hat* jet. Then, the jet propagates within the debris of the neutron star merger, i.e., the neutrino-driven wind moving at velocities of $\sim 0.1 - 0.3$ c (or through static massive star in the case of long GRBs). The interaction between the jet and the external media generates a *cocoon*, whose expansion determines the final structure of the jet. The angular distribution of energy is obtained in the cited works by a post-processing treatment of simulation data. The energy distribution is used for calculating the light curves in the *afterglow* phase. Here, the *cocoon* structure is usually extrapolated by assuming homologous expansion (Lazzati et al., 2018; Mooley et al., 2018) to distances $\sim 10^{16}$ cm (left panel of Figure 1.2). The initial structure of the jet at this distance are used as initial conditions in a new simulation (e.g., Mooley et al., 2018) or for direct calculation of *afterglow* in analytical form (e.g., Lazzati et al., 2018).

Analytical models for structured jets (e.g., Kumar & Granot, 2003; Granot & Kumar, 2003; Granot, 2005; Granot & Ramirez-Ruiz, 2010; Salafia et al., 2016; Granot et al., 2018; Gill & Granot, 2018; Ghirlanda et al., 2019; Beniamini et al., 2020) assume an angular distribution of energy $E(\theta) = E_0 \cdot f(\theta)$ and Lorentz Factor $\Gamma(\theta) = 1 + (\Gamma_0 - 1) \cdot f(\theta)$, being $f(\theta)$ a smooth angular function (typically a Gaussian or a power-law). These energy and Lorentz factor profiles are a parametrization of the cocoon which has previously expanded to $r \sim 10^{16}$ cm (right side of Figure 1.2), then starts decelerating. Each angular slice $\Delta\theta$ evolves as an independent element of the fluid which behaves like a relativistic shock wave in the deceleration phase described by (Blandford & McKee, 1976) model. The radiation is calculated by the method discussed in section 1.5.

1.7 Motivation and objectives of this thesis

So far, most GRBs have been detected *on-axis*. In this case, the dynamics and radiation can be in most cases described by a simple top-hat model and standard synchrotron radiation. Nevertheless, the detection of the first unambiguous *off-axis* GRB 170817A, changed the paradigm of our understanding of dynamics and emissions emitted from a GRB. This transient event was not only detected by its electromagnetic counterparts

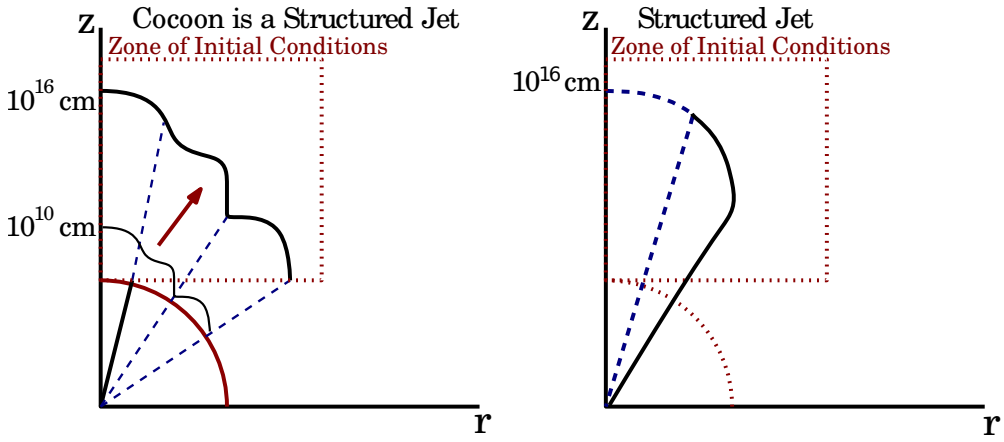

Figure 1.2: Cartoon of structured jets. *Left panel:* Different phases of the jet evolution. First, the jet crosses the neutrino-driven wind or massive star progenitor (red circle). An external cocoon is formed as a result of the jet-wind interaction, which forms a structured jet. To follow the dynamics and emission, the structure of the jet is extrapolated to 10^{16} cm, i.e., the typical scales of *afterglow*. The result of this extrapolation is used to define new initial conditions (dotted square) for new numerical simulations or analytical estimations of the *afterglow* emission by using the Blandford & McKee (1976) model and standard synchrotron emission. *Right panel:* initial conditions of structured jets at large scales. The *cocoon* structure is parametrized trough an angular energy profile $E(\theta)$ and Lorentz factor $\Gamma(\theta)$. This method has been used in the literature to compute simulations at large scales avoiding the previous jet dynamics at small scales.

(e.g., Troja et al., 2018; Margutti et al., 2018; Lazzati et al., 2018; Makhathini et al., 2020), but it was also associated to the gravitational wave signal of a binary neutron star merger (Abbott et al., 2017b). From GRB 170817A, it was possible to get information on the central engine itself, for instance on the time of collapse (e.g., Murguia-Berthier et al., 2021a), the velocity of expansion (e.g., Ciolfi et al., 2017; Ciolfi, 2020) of the dynamical ejecta and the breakout time of the jet (e.g., Lazzati et al., 2020). Several works explored the structure of the jet (e.g., Troja et al., 2018; Margutti et al., 2018; Lazzati et al., 2018; Mooley et al., 2018; Gill et al., 2019; Makhathini et al., 2020) determining that only a structured jet could reproduce the observed *afterglow* emission.

The jet structure is connected with the process of jet launching and the interaction with the external medium. Therefore, understanding how the initial structure of the jet changes by its interaction with the environment can in principle help to constrain the central engine physics, the jet dynamics and the density of the environment. In addition, as gravitational wave (GW) detection will become an increasingly powerful instrument in the near future, it is important to make predictions of GW signals associated to GRBs.

This thesis is focused on understanding how the structure of the jet affects the dynamics and emission of Gamma-Ray Bursts. The studies presented in this thesis were performed by numerical 2D SRHD simulations

of distinct scenarios. At small scales, the propagation of the jet and its interaction with a neutrino-driven wind was studied in the context of short GRBs. The interaction of the jet with a massive star progenitor was studied for long GRBs. At large scales the structure of a blast wave was studied to understand the lateral expansion.

This thesis is divided in five parts:

1. The study of structured jets crossing a spherical neutrino driven wind. The aim of this study is to understand which element is more important for the final structure of the jet, the initial structure of the jet or the interaction with the wind; and to determine how the initial jet structure modifies the afterglow radiation. The results are presented in Chapter 2. A paper concerning this problem was published to the "Monthly Notices of the Royal Astronomical Society".

2. The study of structured jets propagating through a massive stellar progenitor. We implemented structured jets in three-dimensional simulations and study if the initial structure of the jet affect the propagation in a very dense media; how the presence of instabilities in the jet affect the jet propagation; how the jet propagation changes due to the nature of the jet, i.e. for jets dominated by kinetic or thermal energy. The results are presented in Chapter 3. A paper concerning this problem was submitted in the "Monthly Notices of the Royal Astronomical Society".

3. The study of the deceleration of structured jets at large scales. The aim of this study is to study the evolution of the jet structure, its lateral expansion and the resulting afterglow emission. The results are presented in Chapter 4. A paper concerning this problem is in preparation and will be submitted to the "Monthly Notices of the Royal Astronomical Society".

4. The study of the GW signal produced by relativistic jets in the context of long GRBs. The aim of this study is to predict the GW power spectrum produced during the jet propagation and determine if this signal can be detected in the future . The results are presented in Chapter 5. A paper concerning this problem was submitted to the "Monthly Notices of the Royal Astronomical Society".

5. Conclusions in Chapter 6.

Note that before each paper in its specific chapter, a resume highlighting the main results and importance is presented. The abstract, introduction, conclusions and appendixes are the same as the publication.

Chapter 2

What determines the structure of short gamma-ray burst jets?

Este capítulo tiene como contenido el artículo que se publicó como: **Urrutia, G.**, De Colle, F., Murguia-Berthier, A., & Ramírez-Ruíz, E., "What determines the structure of short gamma-ray burst jets?", MNRAS, 503, 4363, 2021.

In this chapter, I present results of numerical simulations of short structured GRBs jets propagating within a spherical Neutrino-Driven Wind (NDW), and how the dynamics modifies the afterglow radiation.

On August 2017, the first detection of a short GRB (the GRB 170817A) accompanied by gravitational wave emission was detected (Abbott et al., 2017b). Since this GRB take place at a short distance from our galaxy ($\sim$ 40 Mpc), the electromagnetic counterparts were observed in detail for several weeks/month on a wide range of frequencies (e.g., Makhathini et al., 2020). The analysis of the light curves revealed that GRB 170817A is the first unambiguous off-axis GRB (Margutti et al., 2018; Troja et al., 2018; Mooley et al., 2018; Lazzati et al., 2018). Furthermore, the light curves revealed an atypical behavior that change our paradigm of the dynamics and emission of GRBs (e.g., Granot et al., 2018). Typically, studies of jet propagation assumed an initial jet with top-hat structure (Lazzati et al., 2018). However, GRB 170817A observations shows that the jet structure plays an important role in the dynamics and emission. So far, several studies, both numerical and analytical, discussed how the structure of the jet determines the observed radiation (e.g., Lazzati et al., 2018; Mooley et al., 2018; Murguia-Berthier et al., 2021a).

Numerical works studied the dynamics of the jet and the evolution of its structure during the interaction of the jet with the debris (e.g., Murguia-Berthier et al., 2021a) from the NS-NS merger (i.e., the dynamical ejecta or the neutrino-driven wind - NDW hereafter). However, the jets involved in these studies were initialized by assuming a top-hat initial structure for the jet. Studies of jet launching show that the physical components of the central engine, such as the magnetic fields, accretion rate, structure of accretion disk, and presence of winds, it leads to a more complex jet structures (e.g., Kathirgamaraju et al., 2017; Janiuk et al., 2021)

The main question of the work presented in this chapter is to determine which element is most important, if the parameters of the dynamical NDW or the initial structure of the jet. The aim of this work is to determine how different initial structures (top-hat, Gaussian and power law) modify the dynamics and radiation of jets.

We run numerical simulations of short GRB jets by employing the *Mezcal* code. The jets are implemented with different luminosities, duration and initial structure. The initial structure is parametrized by defining different angular distributions of the jet luminosity, which modify the energy distribution of the jet, and different angular distribution of the Lorentz factor. We follow the propagation of the jet during its interaction with the merger remnant wind and its propagation in the external ambient medium. By post-processing the output of the simulation, we compute the jet energy distribution at $r \sim 10^{11}$ cm. In addition, by an extrapolation of the final structure to distances $r \sim 10^{16}$ cm, we compute analytically the afterglow light curves for each structured jet.

We found that the initial structure, in addition with the injection time and luminosity, determine the final structure of the jet. The final structure can be distinguished for high luminosity jet and long-lasting time injection. These results have direct consequences in the afterglow emission, which also suffers a modification in the shape of light curves. We compare our light curves with the data of GRB 170817 A and found that our predictions are consistent with the value of observer angle reported in previous works.

2.1 Article abstract

The discovery of GRB 170817A, the first unambiguous off-axis short gamma-ray burst arising from a neutron star merger, has challenged our understanding of the angular structure of relativistic jets. Studies of the jet propagation usually assume that the jet is ejected from the central engine with a top-hat structure and its final structure, which determines the observed light curve and spectra, is primarily regulated by the interaction with the nearby environment. However, jets are expected to be produced with a structure that is more complex than a simple top-hat, as shown by global accretion simulations. We present numerical simulations of short GRBs launched with a wide range of initial structures, durations and luminosities. We follow the jet interaction with the merger remnant wind and compute its final structure at distances $\gtrsim 10^{11}$ cm from the central engine. We show that the final jet structure, as well as the resulting afterglow emission, depend strongly on the initial structure of the jet, its luminosity and duration. While the initial structure at the jet is preserved for long-lasting SGRBs, it is strongly modified for jets barely making their way through the wind. This illustrates the importance of combining the results of global simulations with propagation studies in order to better predict the expected afterglow signatures from neutron star mergers. Structured jets provide a reasonable description of the GRB 170817A afterglow emission with an off-axis angle $\theta_{\rm obs} \approx 22.5°$.

2.2 Introduction

Short gamma-ray bursts (sGRBs) are intense flashes of γ-rays lasting $\lesssim 2$ s. They are produced by the coalescence of neutron stars, accompanied by the ejection of powerful relativistic jets with energies $\approx 10^{51}$ erg and opening angles $\theta_j \lesssim 10°$ (see Kumar & Zhang, 2015, for a review).

The merger of a neutron star binary can produce hyper-massive neutron stars (HMNS) for equations of state that allow a maximum mass for non-rotating neutron stars in the range 2.6-2.8$M_\odot$ (Shibata & Taniguchi, 2006; Baiotti et al., 2008). Otherwise, the remnant will collapse to a black hole. In the former case, angular momentum transport from the inner to the outer regions of the remnant will drive significant mass loss through a neutrino-driven (Rosswog et al., 2003; Lee & Ramirez-Ruiz, 2007; Dessart et al., 2009; Perego et al., 2014), or a magnetically-driven wind (Rezzolla et al., 2011; Siegel et al., 2014; Ciolfi et al., 2017; Ciolfi, 2020). Different mechanisms responsible for the mass-loss naturally lead to different wind structures (e.g, Murguia-Berthier et al., 2017a).

As the jet traverses the wind environment, it decelerates depositing a significant fraction of its kinetic energy

into an extended, hot cocoon (e.g., Ramirez-Ruiz et al., 2002). In this phase, the cocoon pressure helps to collimate the jet. Once the jet and cocoon break out of the dense environment (at a distance $\approx 10^{10}$ cm from the central engine), the cocoon expands laterally. The jet core, with an opening angle $\lesssim 5°$–$10°$, moves at highly relativistic speeds (with Lorentz factors $\Gamma \approx 100$), while the cocoon shows a steep velocity gradient in the polar direction, expanding initially at mildly relativistic speed ($\Gamma \approx$ 2-10) close to the core of the jet and at non-relativistic speeds near the equatorial plane (Kumar & Granot, 2003; Granot, 2005; Bromberg et al., 2011b; Granot, 2012).

The radial and angular structure of the jet and cocoon after the break-out regulates the late dynamics, and it is the key parameter in determining the shape of the light curve at large scales (e.g., Granot, 2005; Duffell et al., 2018; Lazzati et al., 2018; Mooley et al., 2018; Nakar et al., 2018) and the rate of off-axis SGRBs which will be observed by upcoming multi-wavelength surveys (Salafia et al., 2016; Ghirlanda et al., 2019; Gottlieb et al., 2019).

As the GRB prompt and afterglow emission is strongly beamed and the relativistic jets are unresolved, the jet structure is poorly known. Observations of the GRB 170817A have given some insights on the angular structure of short GRBs. The afterglow emission has been interpreted as evidence of a structured jet (nevertheless, see Gill et al. 2019 for an alternative explanation invoking a top-hat structure for the jet), moving $\approx 20°$-$30°$ off-axis with respect to the line of sight, with energy $E_{\rm iso} = 10^{49} - 10^{51}$ ergs, ambient density $n_{\rm ISM} = 10^{-4} - 10^{-3}\,{\rm cm}^{-3}$, and microphysical parameters $\epsilon_e \sim 10^{-2}$ and $\epsilon_B \sim 10^{-4} - 10^{-3}$ (where ϵ_B and ϵ_e are the fractions of post-shock thermal energy ending into the energy of the magnetic field and accelerated electrons, respectively; see, e.g., Murguia-Berthier et al., 2017a; Granot et al., 2018; Lazzati et al., 2018; Mooley et al., 2018; Nathanail et al., 2020), although there is a large degeneracy in the determination of these parameters.

Numerical simulations of the jet propagating through the environment of the central engine have clarified the role that the wind plays in shaping the structure of the jet (Aloy et al., 2005; Murguia-Berthier et al., 2014; Kathirgamaraju et al., 2017; Murguia-Berthier et al., 2017a; Bromberg et al., 2018; Duffell et al., 2018; Granot et al., 2018; Lazzati et al., 2018; Lamb & Kobayashi, 2018; Xie et al., 2018; Gill et al., 2019; Lamb et al., 2019; Lazzati & Perna, 2019; Lazzati et al., 2020; Hamidani et al., 2020; Murguia-Berthier et al., 2021a).[1]

Extrapolating these simulations up to distances $\approx 10^{16}$ cm, one can solve the inverse problem and attempt to constrain the small scale structure of the jet (e.g., Duffell et al., 2018; Lazzati et al., 2018; Mooley et al.,

[1]The wind can also be dense enough to completely shocked the jet.

2018; Nathanail et al., 2020). Thus, the interaction of the jet with the environment and the resulting jet structure can in principle constrain the mechanism leading to both the mass-loss during the merger as well as the initial structure of the jet (Rosswog & Ramirez-Ruiz, 2002b, 2003; Murguia-Berthier et al., 2014, 2017a; Murguia-Berthier et al., 2021a).

Numerical simulations of SGRB typically assume that the jet is launched with a top-hat structure. On the other hand, numerical simulations of the jet formation (Rosswog & Liebendörfer, 2003; Rosswog et al., 2003; Rezzolla et al., 2011; McKinney et al., 2012) show that the jet density and velocity structures are more complex than a simple top-hat. For instance, GRMHD numerical simulations from Kathirgamaraju et al. (2019) show that jet is strongly structured at a distance of $\approx 6 \times 10^8$ cm. Observations of AGN jets also indicate that jets are not homogeneous along the angular direction, with a low-density, fast moving material in the inner region of the jet associated to more dense and slower moving material at large polar angles (see, e.g., Walg et al., 2013, and references therein).

The role played by the intrinsic jet properties (jet opening angle, structure, luminosity, duration and magnetic field at the launching point) in determining the final jet structure has been not been studied yet in detail. Thus, in this paper we present numerical simulations of jets structured along the polar direction, i.e., with a jet luminosity $L_j(\theta)$ and Lorentz factor $\Gamma(\theta)$, and compare the outcome with simulations that assume a top-hat jet. We also explore the effect of changing the injection duration of the jet t_j and the luminosity history $L(t)$, which is expected to decrease with time, as the disk around the merger remnant is viscous drained (e.g., Lee et al., 2005).

This paper is structured as follows: in section 2.3 we describe the code and the initial conditions employed in our simulations. In section 2.4 we present the results of the numerical simulations and the final structure of top-hat and (intrinsic) structured jets. In section 2.5 we discuss the results and their observational implications. Finally, in section 2.6 we summarize our results.

2.3 Methods

We study the propagation of SGRB jets through the pre-collapse merger remnant environment by running a set of special relativistic hydrodynamics (SRHD) simulations. We use the adaptive mesh refinement (AMR) code *Mezcal* (De Colle et al., 2012a). The code employs a second-order Runge-Kutta time integrator, and second-order space interpolation, which reduces to first order by a minmod limiter. We use the HLL method (Harten,

Table 2.1: Initial conditions of the numerical simulations.

Model	$t_{\rm j}$ (s)	$L_{\rm j}$ (erg s^{-1})	jet structure
Low Luminosity TB	0.6	1.5×10^{49}	Top-hat Gaussian Power-law
Low Luminosity TM	1.5	1.5×10^{49}	Top-hat Gaussian Power-law
Low Luminosity TL	3.0	1.5×10^{49}	Top-hat Gaussian Power-law
High Luminosity TB	0.5	1×10^{50}	Top-hat Gaussian Power-law
High Luminosity TM	1.5	1×10^{50}	Top-hat Gaussian Power-law
High Luminosity TL	3.0	1×10^{50}	Top-hat Gaussian Power-law
Time-dependent Luminosity	2.0	$L_{\rm jet}(t)$	Top-hat

1983). Coupling the HLL method with the minmod limiter makes the method very robust, although somehow dissipative. In the relativistic version of the code, the primitive variables (the density ρ, the velocities $\vec{v}$ and the pressure p) are determined from the conservative variables ($D = \rho\gamma$, $\vec{m} = Dh\gamma\vec{v}$, $\tau = Dh\gamma c^2 - p - Dc^2$, where γ is the Lorentz factor and h the enthalpy) by using an iterative Newton-Raphson method for the equation $F(\Theta) = h(\Theta)\gamma(\Theta) - \Theta/\Gamma(\Theta) - 1 - \tau/Dc^2$, being $\Theta = p/\rho c^2$ (see De Colle et al. 2012a for more details).

As detailed below, we explore the effect of changing the jet duration t_j, luminosity $L_j(\theta, t)$ (as a function of time and polar angle θ) and jet angular structure, i.e., the jet density $\rho_j(\theta)$ and velocity $\Gamma_j(\theta)$.[2] The initial conditions of the simulations presented in this paper are listed in Table 2.1.

The simulations are done by using a two-dimensional axisymmetric grid, with 800×800 cells along the r and z direction at the lowest level of refinement and with 6 levels of refinement, corresponding to 25600×25600 cells at the highest level of refinement. The size of the computational box is $(L_r, L_z) = (4.8, 4.8) \times 10^{11}$ cm, with a maximum resolution of 1.8×10^7 cm.

At $t = 0$, the computation box is filled with a static medium with density $\rho_a = n_a m_p$ (with $n_a = 10^{-5}$ cm^{-3}) and a pressure $p_a = 10^{-10}\rho_a c^2$. As the jet and wind are highly supersonic, the results are independent of the pressure of the ambient medium. From an inner boundary located at $r_{\rm in} = 10^9$ cm, we inject a wind, with a velocity $v_w = c/3$ and a wind mass-loss $\dot{M}_w = 10^{-4}$ M$_\odot$ s^{-1} during a time $t_w = 1$ s. At $t > t_w$, the wind density is gradually switched-off by dropping the density as $\rho_w \propto t^{-5/3}$. These wind mass-loss and duration are typical of NS mergers (Qian & Woosley, 1996; Rosswog & Ramirez-Ruiz, 2002a; Lee & Ramirez-Ruiz, 2007). The effect of denser ($\dot{M} \gtrsim 10^{-3}\, M_\odot$) and a spherical wind structures (e.g., Perego et al., 2014) were considered by Murguia-Berthier et al. (2014); Murguia-Berthier et al. (2021a).

Starting at $t = t_w$, and during a time t_j, a jet is launched from a radius $r_j(\theta) = r_w v_j(\theta)/v_{j0}$ (hereafter, the sub-index 0 indicates values computed at $\theta = 0$). We implement three different structures for the jet (see Figure 2.1), changing its luminosity and velocity as a function of the polar angle. The jet structure is defined

[2]The role played by the wind duration t_w and structure has been explored in detail by Murguia-Berthier et al. (2014, 2017a); Murguia-Berthier et al. (2021a) and is not considered here. We also do not consider the jet magnetic field, which can also play an important role in determining the jet structure (Duffell et al., 2018; Gottlieb et al., 2020b; Nathanail et al., 2020).

as

$$f(\theta) = \begin{cases} 1 & \theta \leq \theta_j \\ 0 & \theta > \theta_j \end{cases} \qquad \text{“Top hat” jet ,} \tag{2.1}$$

$$f(\theta) = e^{-\frac{1}{2}\frac{\theta^2}{\theta_j^2}} \qquad \text{“Gaussian” jet ,} \tag{2.2}$$

$$f(\theta) = \left(1 + \frac{\theta^2}{\theta_j^2}\right)^{-3/2} \qquad \text{“Power law” jet ,} \tag{2.3}$$

being $\theta_j = 0.2$ rad the jet core, in which most of the energy is injected.

The jet has a kinetic luminosity

$$L_j(\theta) = L_{j0} f(\theta), \tag{2.4}$$

and a Lorentz factor

$$\Gamma_j(\theta) = 1 + (\Gamma_{j0} - 1) f(\theta) \ , \tag{2.5}$$

where $\Gamma_{j0} = 20$. The jet density is defined as a function of luminosity and Lorentz factor as

$$\rho_j(\theta) = \frac{L_{\rm iso}(\theta)}{4\pi r_j(\theta)^2 \Gamma_j^2(\theta) c^3} \ , \tag{2.6}$$

where the isotropic luminosity is related to the jet luminosity by $L_j = L_{\rm iso}\left(1 - \cos\theta_j\right) \approx L_{\rm iso}\theta_j^2/2$. We assume that the jet is cold, by setting its pressure to $p_j = 10^{-5}\rho_j c^2$. We run simulations by employing typical SGRBs luminosities (e.g., Levan et al., 2016), i.e. $L_j = 10^{50}$ erg s^{-1}, but we also run simulations with lower jet luminosities $L_j = 1.5 \times 10^{49}$ erg s^{-1}.

We run simulations for different jet lifetimes t_j (see Table 2.1). The time $t_j = $ TB corresponds approximately to the break-out time ($t_{\rm bo}$), i.e. $t_j = 0.5$ s and $t_j = 0.6$ s for the high and low luminosity top-hat model (similar values are obtained also for structured jets as the core energy is similar in all our models). The time $t_j = $ TM is taken by considering the typical duration of a SGRB $T_{90} \sim 0.9$ s (e.g., Berger, 2014; Levan et al., 2016) and $t_j = t_{\rm bo} + t_{\rm B}$. We also run simulations by using $t_j = $ TL $= 3$ s, corresponding to SGRB in the tail of the duration distribution.

In addition, we run simulations with a top-hat jet structure considering a luminosity that changes with time.

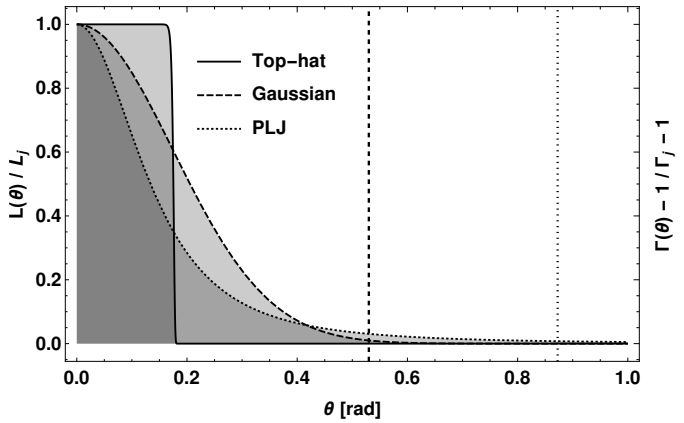

Figure 2.1: Kinetic luminosity and Lorentz factor profiles for the structured jets implemented in the numerical simulations. The top-hat jet (solid line) has a cut-off angle of $\theta_j = 10°$. Gaussian (dashed line) and power-law jet (dotted line) profiles present extended wings moving with Newtonian velocity.

We consider a constant luminosity followed by a power-law decrease,

$$L(t) = \begin{cases} L_0 & t < t_0 \\ L_0 (t/t_0)^{-5/3} & t > t_0 \end{cases} \tag{2.7}$$

which reduces to $L_0 = E_{\rm j}/t_{\rm j}$ when $t = t_j$. We take $t_0 = t_j/10$.

Finally, we caution that two-dimensional simulations are prone to a numerical instability known as the "plug" instability (Lazzati et al., 2015). This instability results from the symmetry used in two-dimensional simulations, and disappears in three-dimensional simulations once the symmetry with respect to the jet axis is broken by taking asymmetric initial conditions (e.g., a small jet precession or asymmetric variations in the ambient medium) or by employing asymmetric numerical methods in the integration of the SRHD equations[3] (e.g., split solvers). In Appendix A, we show how this instabilities can be suppressed by slightly changing the jet velocity direction.

In three-dimensional simulations, instabilities generated at the contact discontinuity extend to the jet axis, mixing baryon-rich material with the baryon poor jet material. The baryonic contamination then reduces the jet velocity (e.g. Gottlieb et al., 2020a; Gottlieb et al., 2020b; Harrison et al., 2018). However, this happens only in dense media, so it affects more LGRBs than SGRBs (which cross a few % of the material than LGRBs). Also (as we will show in the next section), in structured jets the contact discontinuity is pushed away from the

[3]When using unsplit solvers and symmetric initial conditions, three dimensional numerical simulations are identical (at machine precision) to two dimensional simulations.

jet axis, then dropping the amount of baryon-rich material reaching the jet.

2.4 Results

2.4.1 Jet dynamics

Figure 2.2 shows the evolution of top-hat, Gaussian and power-law jets (from left to right in the figure) at time $t = 1.6$ s, $t = 4$ s and $t = 10$ s (top to bottom panels). Each panel is divided into two halves, with the left (right) half showing the low (high) luminosity case. All panels refer to a jet injected during $t_j = 3$ s (TL case, see Table 2.1).

The propagation of a top-hat jet through the environment has been considered by several authors (e.g., Morsony et al., 2007; López-Cámara et al., 2013; Murguia-Berthier et al., 2014; Lazzati et al., 2015; Duffell et al., 2015; López-Cámara et al., 2016; Murguia-Berthier et al., 2017a; De Colle et al., 2018a,b; Lazzati et al., 2018; Duffell et al., 2018; Harrison et al., 2018; Nathanail et al., 2020; Hamidani et al., 2020; Murguia-Berthier et al., 2021a). The shock velocity can be estimated by assuming ram pressure balance (e.g., Begelman & Cioffi, 1989; Ramirez-Ruiz et al., 2002; Bromberg et al., 2011b; De Colle et al., 2012b), and is given as $v_{\rm sh} = v_j/(1 + (\rho_a/\rho_j\Gamma_j^2)^{1/2})$, where $\rho_a \propto r^{-2}$ and $\rho_j(\theta) \propto L_j(\theta)$ the ambient and jet density respectively. The wind and the jet are injected from a radial distance $r_w = 10^9$ cm from the central engine. At this radius, on axis, $\rho_a \ll \rho_j\Gamma_j^2$, then the jet head moves with a velocity $v_{\rm sh} \approx v_j$ in the high luminosity, and $v_{\rm sh} \lesssim 0.9\ v_j$ in the low luminosity case. As $L_j(\theta)$ quickly drops with angle (see Figure 2.1), the wide angle jet component present in structured jets (middle, right top panels) moves at lower speeds.

As the jet transverses the wind medium, the hot shocked gas forms an extended cocoon (figure 2.2, top panels) which expands at mildly relativistic speeds. The heated plasma is made by the dense, shocked wind, and by the rarefied, shocked jet (the dark yellow region close to the jet axis in figure 2.2) separated by a contact discontinuity. The cocoon pressure helps to collimate the jet, which acquires a nearly cylindrical shape (see, e.g., Ramirez-Ruiz et al., 2002; Bromberg et al., 2011b; Duffell et al., 2015).

As the jet core luminosity (i.e., the region corresponding to $\theta \lesssim \theta_j$) is approximately the same for all jet structures, the velocity of the jet as well as the break-out time are nearly independent on the jet structure but depend strongly on its luminosity. The low luminosity jet reaches the wind shock front at $t = 1.6$ s (or $t - t_w = 0.6$), while high luminosity jets reach the boundary at $t - t_w = 0.5$ (see the upper panel of Figure 2.2).

The jet structure at the launching point strongly affects the cocoon structure. The wide angle outflow

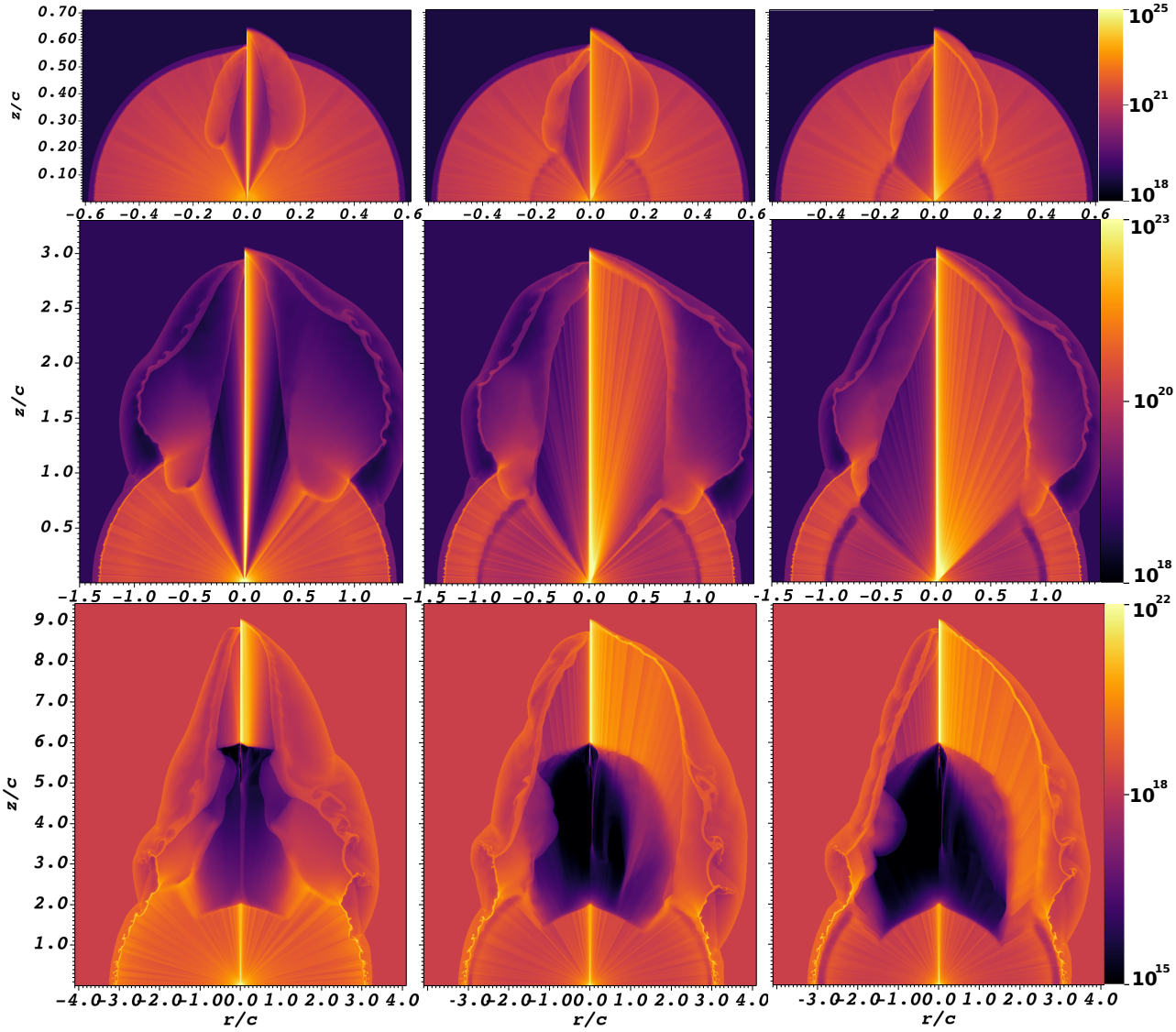

Figure 2.2: Number density maps for jets which time of injection is $t_j = 3$ s. *Left to right panels:* top-hat, gaussian and power-law jet. In each panel, the left (right) half shows the low (high) luminosity jet. *Top to bottom panels:* snapshots at the breakout time $t = 1.6$ s (or $t - t_w = 0.6$ s); 4 s (or $t - t_w = 3$ s), when the jet is switched off; and 10 s (or $t - t_w = 9$ s), corresponding to the final time of the simulations.

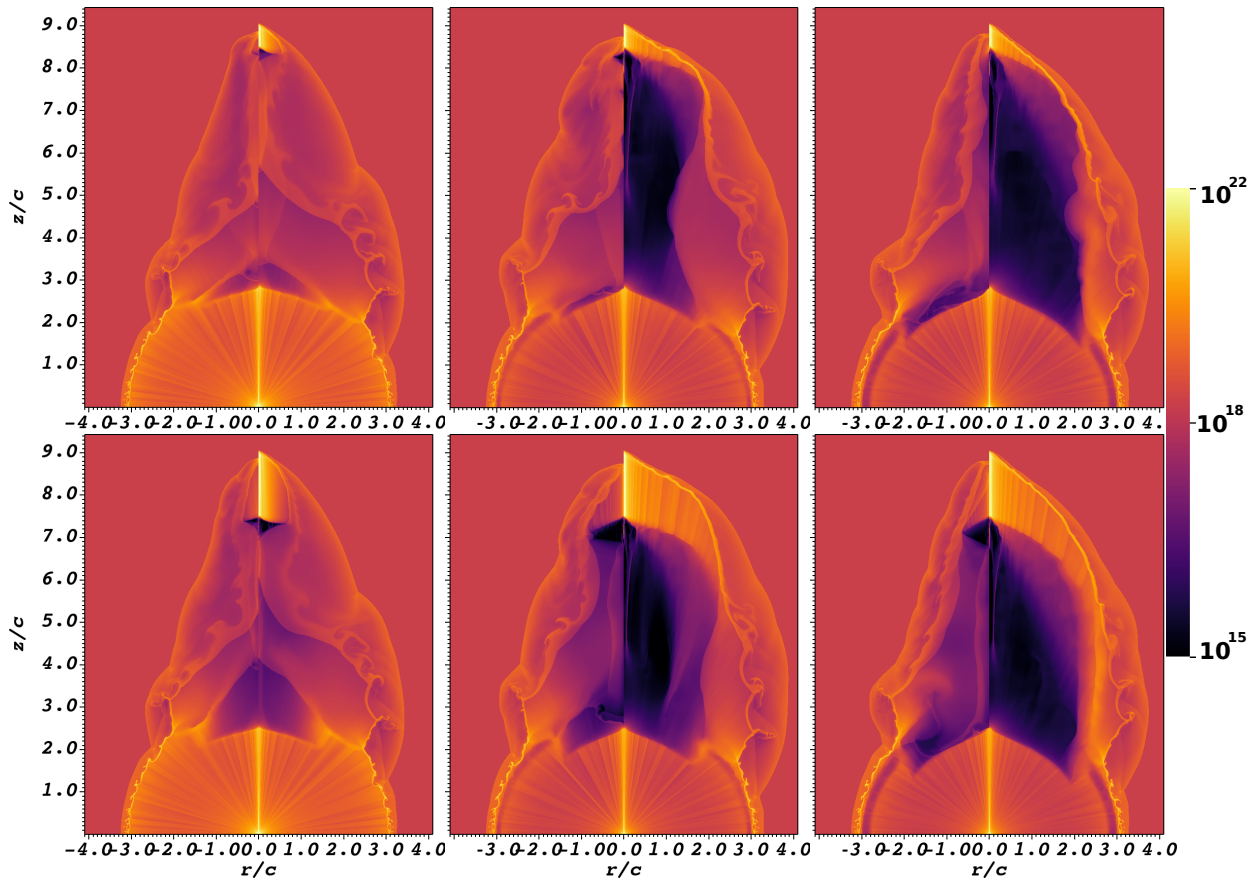

Figure 2.3: Number density maps for jets injected during a time t_j, seen at $t = 10$ s. *Left to right panels:* top-hat, gaussian and power-law jet. *Upper panels*: models with $t_j = 0.6/0.5$ s (each panel shows low L_j in the left half and high L_j in the right half). *Bottom panels*: models with jets lasting $t_j = 1.5$ s. Similar figures for the models with $t_j = 3$ s are shown in the bottom panels of figure 2.2.

component expands at lower speeds, pushing and compressing the cocoon towards larger radii. Differences between different structures are more evident for high luminosity than for low luminosity jets (see Figure 2.2).

The middle and bottom panels of Figure 2.2 show the evolution of the jet as it breaks out of the wind and propagates into the diluted environment. As soon as the jet breaks out of the dense wind, the cocoon quickly expands sideways (at the post-shock sound speed, i.e. $v \approx c/\sqrt{3}$) engulfing the wind medium. Gaussian and power-law jet cocoons expand laterally faster than the top-hat cocoon, as they are pushed from behind by the wide-angle outflow. Structured jets have also different cocoon structures, specially at intermediate angles in which Gaussian jets are more energetic than power-law jets.

The final jet structure is acquired a few seconds after the jet had drilled through the medium launched during the neutron star merger (Lee & Ramirez-Ruiz, 2007; Murguia-Berthier et al., 2014, 2017a; Murguia-Berthier et al., 2021a; Duffell et al., 2015; Bromberg et al., 2018). The final snapshot of our simulations is shown in the bottom panel of figure 2.2. As the jet is switched off, a low-density cavity[4] is formed behind the relativistic shell (with a size of $\lesssim 3$ light seconds).

Figure 2.3 shows density maps at $t = 10$ s as a function of the jet duration, structure and luminosity. As shown in Figure 2.2, the cocoon expand faster in structured jets. The cocoon shape depends on the amount of energy deposited by the jet inside the dense wind. Once the jet breaks out of it, the energy injected from the central engine ends into the jet core only. Then, jets with longer injection times (bottom vs. top panels panels) forms a more elongated and energetic shell of fast moving material, while the cocoon structure remains nearly independent on the jet duration.

The perturbations extending radially through the wind (see, e.g., the bottom left panel of Figure 2.3) are a numerical artifact resulting from injecting a ballistic (i.e., with a kinetic energy much larger than its thermal energy) spherical wind into non-spherical cylindrical coordinates. These small perturbations do not affect the jet propagation.

2.4.2 Jet structure

Once the jet/cocoon system breaks out of the wind medium, it expands and accelerates to highly (the jet) and mildly (the cocoon) relativistic speeds. Then, the jet/cocoon system will expand freely up to distances $R \approx 10^{16} - 10^{17}$ cm before decelerating. Thus, the structure of the jet coming out from our simulations

[4]Low-density, near-vacuum regions are often numerically challenging. The simulations are done by employing a second-order (quite dissipative) HLL integrator. When the integrator fails to find a physically acceptable solution, the code switches to first order.

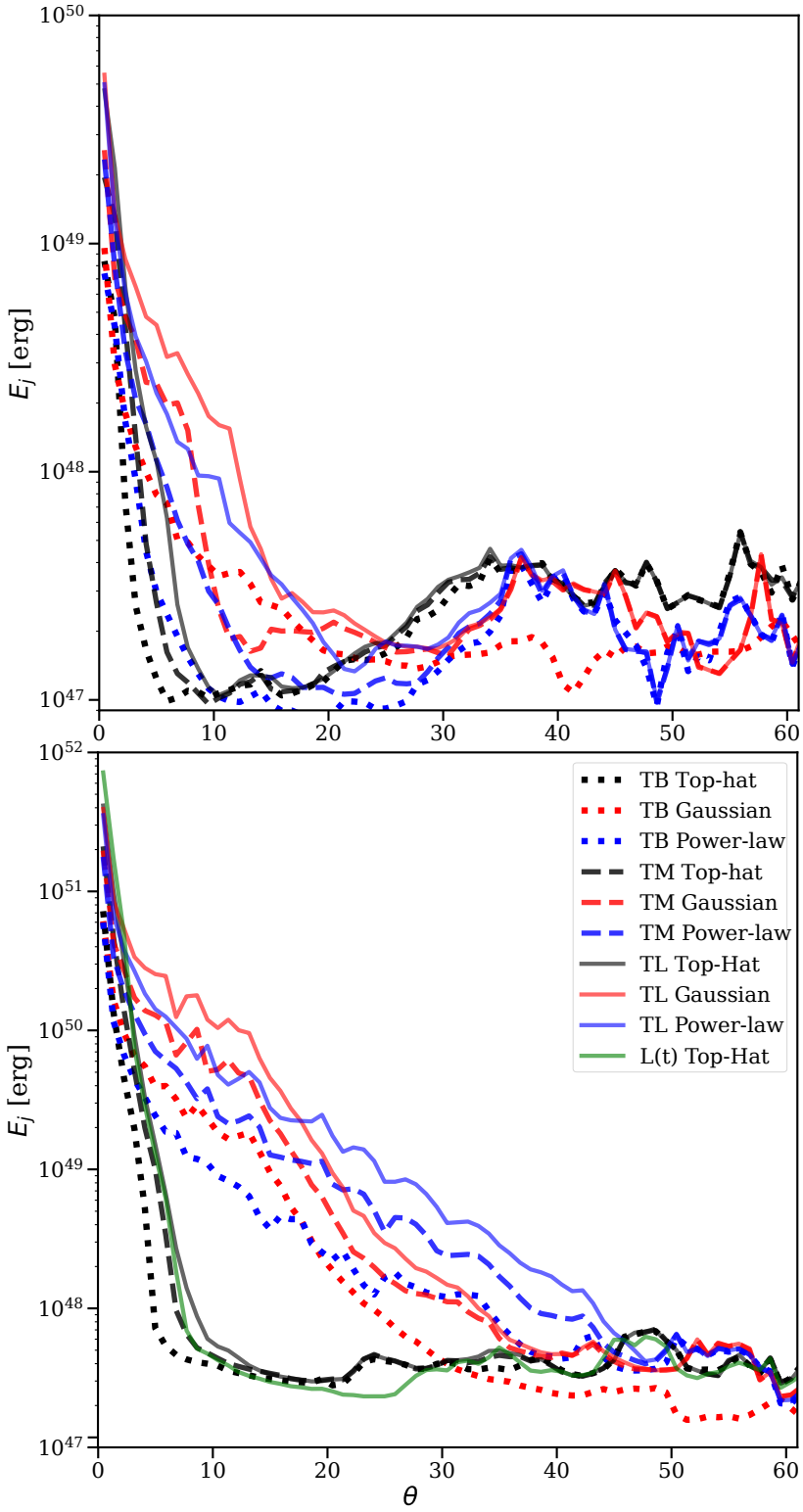

Figure 2.4: Energy of the jet/cocoon system as a function of θ (measured in the lab frame) at $t = 10$ s. *Top:* low luminosity models. *Bottom:* high luminosity models. Models TB, TM, TL correspond to $t_j = 0.5$ s, 1.5 s, 3 s respectively. Model $L(t)$ (bottom panel) corresponds to a jet with a luminosity changing with time.

will determine the structure of the jet and, as such, the afterglow emission, specially in SGRBs seen off-axis (e.g., Murguia-Berthier et al., 2014, 2017a,b; Lazzati et al., 2018; Nakar et al., 2018; Irwin et al., 2019; Murguia-Berthier et al., 2021a).

Figure 2.4 shows the energy at $t = 10$ s, as a function of polar angle θ. Each panel illustrates the dependence of E_j on the jet launching structure and duration. Here E_j includes the cocoon's contribution. Comparing the upper and bottom panels one can also see the effect of increasing the jet's luminosity. For all the models, most of the energy continues to be concentrated into the jet's core.

In all models, the increase in the jet's duration leads to an increase of E_j (which is proportional to the jet duration) and this can be as large as a factor of $\approx$ a few at angles $\gtrsim 10^\circ$. In structured, low-luminosity jets the energy deposited outside the jet core ($\approx 5^\circ - 20^\circ$) is larger than in top-hat jets by $\approx$ an order of magnitude, with the Gaussian jets being more energetic than the power-law jets. Differences between top-hat and structured jets increase dramatically for high luminosity jets (see Figure 2.4, bottom panel). While in top-hat jets most of the increase in the luminosity resides in the jet's core, in structured jets leads to a large spread in energy up to angles $\lesssim 45^\circ$. Consistent with their initial energy distribution (see Figure 2.1), Gaussian jets are slightly more energetic than power-law jets at intermediate angles, and less energetic at large angles (although the exact initial jet structure is certainly not preserved). The bottom panel of Figure 2.4 shows also that a jet with a time-variable, top-hat luminosity has a final structure nearly identical to a top-hat jet with constant luminosity. Yet, it is more energetic on-axis given its higher total power.

These results can be understood by taking into account that, as the jet moves through the wind, it dissipates part of its kinetic energy, effectively transferring energy from the collimated jet to the uncollimated cocoon. Once the jet has broken out of the wind, the energy travelling into the jet channel remains mostly collimated within the initial jet opening angle. The jet luminosity, opening angle, duration and the density structure of the environment all together determine the jet break out time and the amount of energy deposited into the cocoon. Thus, the final jet structure will tend to mimic the initial shape at injection as the jet duration increases. We conclude that on average, the structure of long-lasting SGRBs tracks the initial structure at the jet (at the launching point), while the structure of SGRBs which just barely make their way through the wind are significantly more affected by the external density stratification.

2.5 Discussion

The cocoon is important for the following reasons. First, the cocoon pressure helps collimate the jet, which then acquires a nearly cylindrical shape. This has been extensively studied in the literature (see, e.g., Ramirez-Ruiz et al., 2002; Bromberg et al., 2011b; Duffell et al., 2015). Second, once the cocoon breaks out of the wind, its structure determines the large scale angular structure of the jet. In what follows, we discuss briefly the role played by the initial jet structure in regulating the cocoon energy structure[5].

The structure of the pre-merger environment of the NS merger, shaped by the pre-collapse remnant wind (Lee & Ramirez-Ruiz, 2007; Duffell et al., 2015) is an important component in determining the jet structure (Murguia-Berthier et al., 2014, 2017a; Duffell et al., 2018; Nakar et al., 2018; Irwin et al., 2019; Murguia-Berthier et al., 2021a). A non-homogeneous wind, in particular, can also drastically change the jet dynamics (e.g., Murguia-Berthier et al., 2014, 2017a; Murguia-Berthier et al., 2021a), facilitating the propagation of the jet along the polar regions. Nevertheless, as shown in the previous section, the jet structure after breaking out of the wind depends mainly on the initial jet structure. Depending on the break out time and the jet luminosity, cocoon energies for top-hat and structured jets can drastically differ.

As mentioned before, the final jet structure after breakout has important consequences for the afterglow radiation, as clearly illustrated in the case of GRB 170817A (Lazzati et al., 2018; Mooley et al., 2018; Nathanail et al., 2020). To determine how the jet's structure affects the SGRB emission, we computed the afterglow emission by extrapolating analytically the results of our numerical simulations up to distances[6] $\gtrsim 10^{18}$ cm. This is done by assuming synchrotron emission and considering a one-dimensional evolution at each polar angle, i.e. neglecting lateral expansion. The flux is computed by considering the contribution of each angular slice, which evolves independently in time (i.e., we neglect lateral expansion). Given an energy $E_j(\theta)$ and an initial Lorentz factor $\Gamma_0(\theta)$, we assume that the shock front propagates with constant velocity up to the deceleration radius $R_d \approx (E_j(\theta)/\rho\Gamma_0^2(\theta))^{1/3}$, then decelerating and following the Blandford & McKee (1976) self-similar solution[7]. We assume that a distribution $N(\gamma) \propto \gamma^{-p}$ of electrons are accelerated in the shock front and that a fraction ϵ_e of the post-shock thermal energy resides in the population of accelerated electrons while a fraction ϵ_B resides in the post-shock magnetic field (responsible for the synchrotron radiation). At

[5]Jet rotation can also affect the cocoon structure, as shown in the context of AGN jets (e.g., Keppens et al., 2008; Walg et al., 2013).

[6]We note that we have assumed a constant density ISM, yet the structure of the medium at large radii might be altered if the binary NS hosts a pulsar (Holcomb et al., 2014; Ramirez-Ruiz et al., 2019).

[7]The late time emission is independent of $\Gamma_0(\theta)$ as the late self-similar dynamics depends only on the explosion energy and density of the environment.

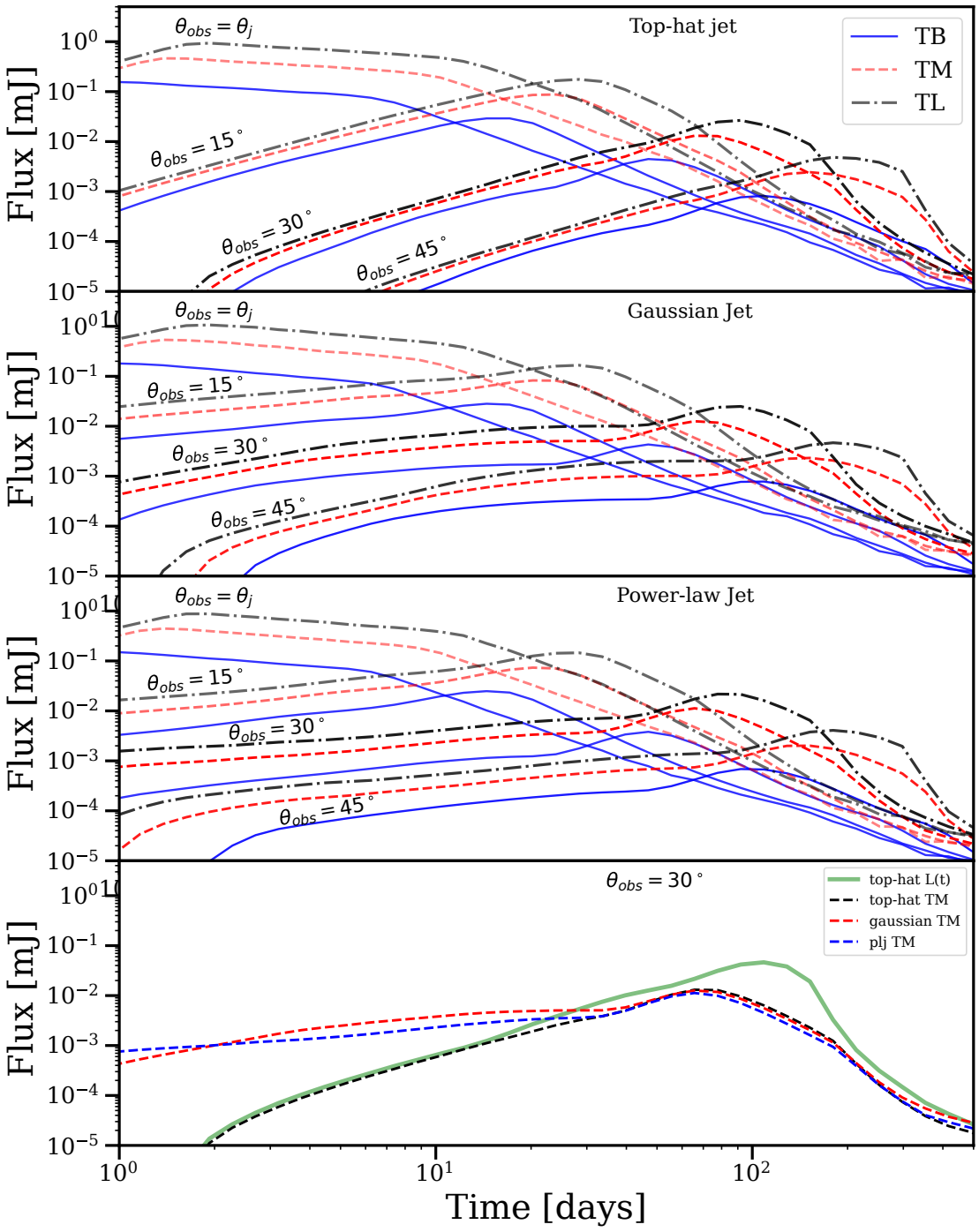

Figure 2.5: Light curves at 3 GHz for the top-hat, gaussian and power-law jet models (from top to bottom), as a function of observing angle. The bottom panel shows a direct comparison between the different jet structures at $\theta_{\rm obs} = 30°$. The light curves have been computed by assuming a constant density stratification, with $n = 1$ cm^{-3}, $\epsilon_e = 0.1$, $\epsilon_B = 0.1$, $p = 2.16$ and $D = 40$ Mpc. The jet luminosity is 10^{51} erg s^{-1}.

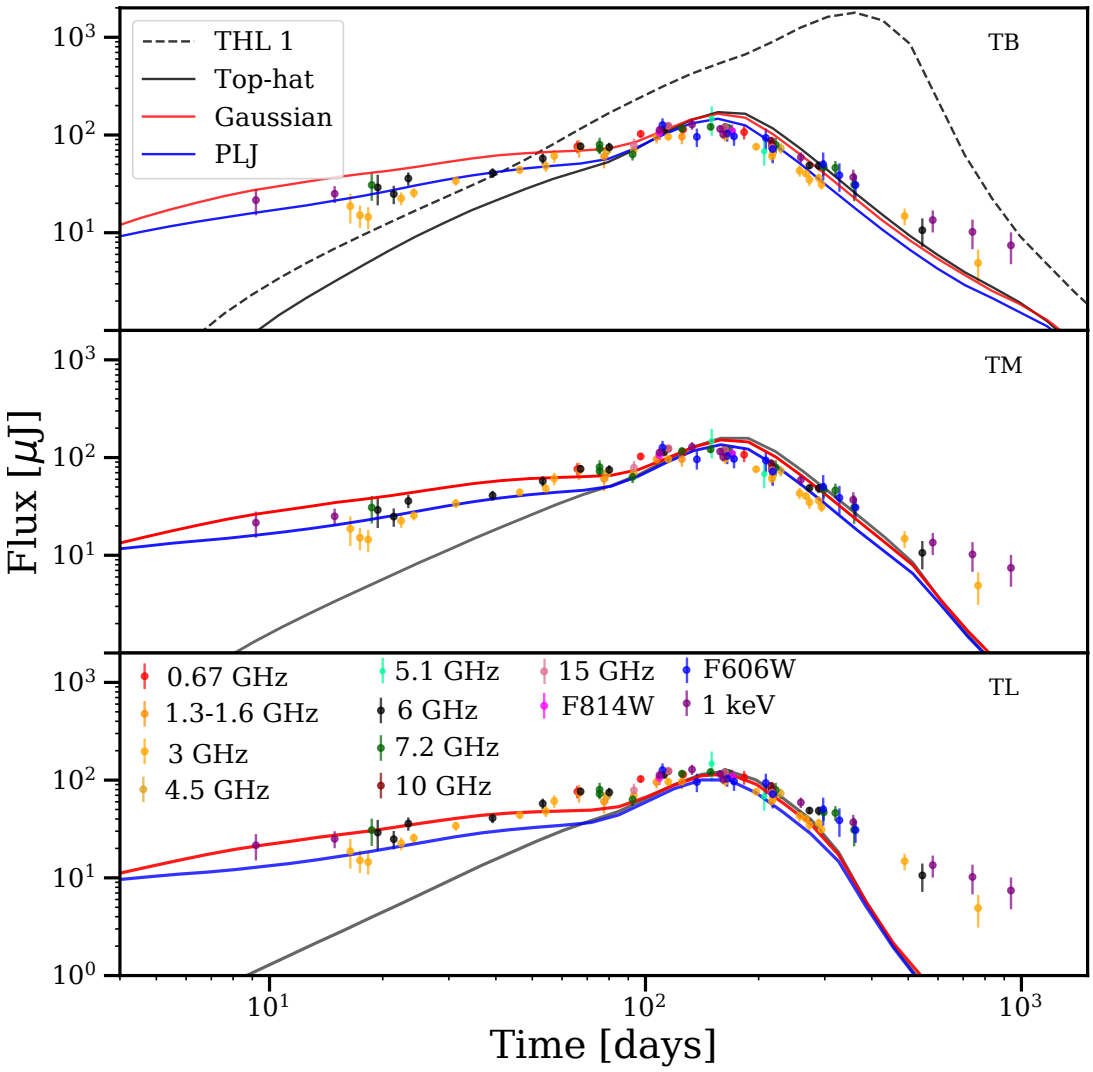

Figure 2.6: Comparison between observations of GRB 170817A and light curves computed by considering different jet structures viewed $\theta_{\rm obs} = 22.5°$. The light curves have been computed by assuming a constant density stratification, with $n = 10^{-3} - 10^{-2}$ cm^{-3} (depending on the model), $\epsilon_e = 0.01$, $\epsilon_B = 0.001$, $p = 2.16$, and $D = 40$ Mpc. Observations are rescaled at 3 GHz (Makhathini et al., 2020). We stress that there is a large degeneracy into the choice of the microphysical parameters (see the text for discussion).

a fixed time (measured in the lab frame), we consider the emission of the post-shock region, assigning it to the corresponding time bin in the observer frame (De Colle et al., 2012a). We caution that these results are not perfectly accurate at late times when the flow becomes mildly-relativistic and lateral expansion strongly affects the flow dynamics. Yet, these calculations clearly illustrate the effects of changing the jet structure on the early time emission.

Figure 2.5 shows light curves at 3 GHz. At $\theta_{\rm obs} \approx 0°$ (i.e., for on-axis jets), the emission is dominated by the highly beamed jet core and the cocoon emission is negligible at all times. Thus, all models produce very similar light curves. For jets with lower luminosity, the cocoon emission can become dominant at late times. As expected, differences between the models are more evident for off-axis light curves (at $\theta_{\rm obs} \gtrsim \theta_j$). At early time the observer detects emission coming directly from the cocoon, as the core of the jet is beamed away from the observer. Then, the early time ($\approx 1 - 10$ days in the figure) flux is much larger in structured jets than in top hat jets. While top-hat jets show the flux increasing as t^3, the increase is slower for Gaussian and power-law jets[8]. At later times (i.e. at the peak of the light curves, see Figure 2.5), the jet core decelerates and enters into the observer's field of view, dominating the afterglow emission. As in the on-axis case, the emission thereafter is nearly independent on the initial structure of the jet.

Figure 2.6 shows a comparison between our model and observations of the GRB 170817A (observations are taken from Makhathini et al. 2020). For a jet injected initially with a top hat structure, the amount of energy at large angles is not sufficient to explain the observations, while the agreement is good for Gaussian and power-law jet models. Denser winds might be able to produce more extended and energetic cocoon for top-hat models which could in principle explain the observations as well. This certainly illustrates the large degeneracy present when trying to deduce the original structure of the jet from afterglow emission (see also, Gill et al., 2019; Takahashi & Ioka, 2020; Takahashi & Ioka, 2021).

Finally, we notice that differences between model and observations at $t_{\rm obs} \gtrsim 300$ days might be due to the fact that we are not considering lateral expansion.

Our analytical calculations describes well the afterglow emission which occurs in an optically thin medium. In this medium, the re-emission effects can be depreciated (e.g., Granot & Sari, 2002). An emission calculations integrated by ray-tracing is not necessary in the absence of re-emission effects that need a history of interactions. Then, one can estimate the flux (light curves) through the contribution of each cell in the domain within history. Our flux calculations evolves independently for each angle and it reduces the problem to one

[8]The $F(t) \propto t^3$ increase is flatter when considering the lateral expansion, see Gill et al. (2019).

dimension. However, information about lateral expansion is forgotten. In future work, we will present the calculus emission from large-scale simulations which will contain information about lateral expansion and instabilities in the front of the shock.

Light curves computed for one set of microphysical parameters can be rescaled if, as in the case of GRB 170817A, they all land in the same spectral range (Granot, 2012; van Eerten & MacFadyen, 2012). Given a set of parameters $E_j, n, \epsilon_e, \epsilon_b$, a flux F_ν and an observer time t, a new set of parameters is given by

$$\frac{t'}{t} = \left(\frac{k}{\lambda}\right)^{1/3}, \tag{2.8}$$

$$\frac{F'}{F} = k\lambda^{(1+p)/4}\left(\frac{\epsilon'_e}{\epsilon_e}\right)^{p-1}\left(\frac{\epsilon'_B}{\epsilon_B}\right)^{(1-p)/4}, \tag{2.9}$$

being $E' = kE$ and $n' = \lambda n$. Inverting this equations, we get

$$n = n_0\left(\frac{\epsilon_e}{0.01}\right)^{4\frac{1-p}{p+5}}\left(\frac{\epsilon_B}{0.001}\right)^{\frac{p-1}{p+5}}, \tag{2.10}$$

$$E = E_0\left(\frac{\epsilon_e}{0.01}\right)^{4\frac{1-p}{p+5}}\left(\frac{\epsilon_B}{0.001}\right)^{\frac{p-1}{p+5}}, \tag{2.11}$$

with $n_0 = 1.7\times10^{-3}$ cm^{-3}, 5.6×10^{-3} cm^{-3} and 1.5×10^{-2} cm^{-3} for the models shown in Figure 2.6 (from top to bottom panel), and where $E_0 = 2.9\times10^{50}$ erg, 3.6×10^{50} erg and 4.2×10^{50} erg.

2.6 Conclusions

In this paper we presented numerical simulations of relativistic jets associated with SGRBs. We explored different initial jet structures, duration and luminosities. The numerical simulations show that the initial jet structure plays a pivotal role on its final structure once it breaks out from the dense wind medium expected around the NS merger at the time of jet triggering. As such, the initial jet structure, which needs to be deduced from global simulations of neutrino-cooled disks, impacts the jet afterglow emission observed in SGRBs.

We show that high luminosity structured jets can have significantly more energy at large observing angles than jets injected with a top-hat structure. The final distribution of the jet depends on the density stratification of the environment and on the jet duration, with the initial jet structure better preserved in tenuous media and for long-lasting jets. We also show that the afterglow emission strongly depends on the initial jet structure. Although a large degeneracy is observed in the determination of the physical parameters, our results

have highlighted the importance of understanding the initial structure of jet given its expected imprint in observations of afterglow emission from SGRBs.

2.7 Appendix: On the "plug" instability in two-dimensional jet simulations

Two-dimensional simulations are prone to a numerical instability known as the "plug" instability. The plug instability is an artifact that appears frequently in simulations of relativistic and non-relativistic jets, and corresponds to a large accumulation of material at the shock front. This instability is not numerical. Indeed, it represents the correct numerical solution to a 2D problem, but not the correct physical solution. This instability is not present in three dimensional simulations when the symmetry with respect to the direction of propagation of the jet is broken (e.g., López-Cámara et al., 2013; Lazzati et al., 2015; López-Cámara et al., 2016). In 3D simulations, the extra degree of freedom makes possible for the material in front of the shock to move laterally, while this is more difficult in 2D simulations

In our 2D simulations in cylindrical coordinates, the jet velocity in the top-hat jet is defined at the inner boundary as

$$v_r = v_j \frac{r - r_0}{R} \qquad v_z = v_j \frac{z}{R} \,, \tag{2.12}$$

being $R = \sqrt{r^2 + z^2}$. When setting $r_0 = 0$, the jet velocity is radial and the simulation presents the "plug" instability. By implementing a small change into the direction of propagation of the jet (i.e. by assuming that the jet velocity is not perfectly radial), this instability is suppressed (see Figure 2.7). Substantially, this is equivalent to considering a jet with a velocity intermediate between radial and cylindrical (with $v = v_z$), i.e. making the jet "sharper".

Specifically, we choose

$$r_0 = r e^{-\left(\frac{r}{\eta r_w}\right)^2} \tag{2.13}$$

being r_w the radius of the inner boundary ($= 10^9$ cm in our case) and $\eta < 1$ a small value (we choose, somehow arbitrarily, $\eta = 1/3$), such that the velocity is approximately radial at $r = 0$ and $r = r_w$, but it slightly differs from radial otherwise.

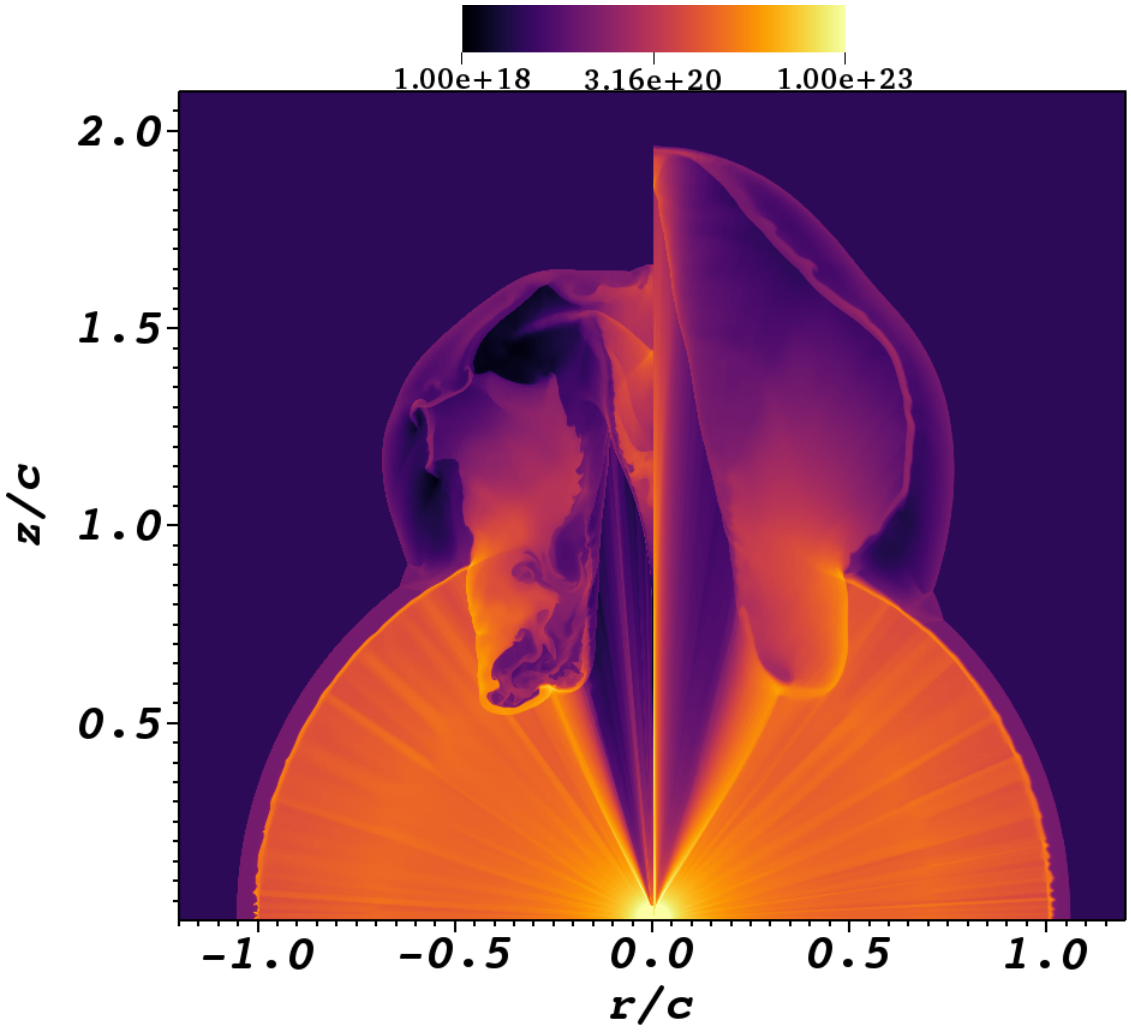

Figure 2.7: Density map. *Left*: Jet with a top-hat, radial injection velocity. The "plug" instability forms an extended, dense region close to the $r = 0$ axis. *Right*: jet simulations done by changing the direction of the jet velocity at the inner boundary (see the text for details). The plug instability is largely suppressed.

Chapter 3

Three-dimensional numerical simulations of structured GRB jets

Este capítulo tiene como contenido el artículo enviado a Monthly Notices of the Royal Astronomical Society como: **Urrutia, G.**, De Colle, F., & López-Cámara, D., "Three-dimensional numerical simulations of structured GRB jets", MNRAS, Submitted, July 2022. El árbitro ha mandado sus comentarios con cambios menores recomendando la publicación en la revista. La respuesta al árbitro está siendo elaborada.

Since the detection of first unambiguous off-axis GRB (the GRB 170817A), it is clear that the structure of the jet plays an important role in determining the dynamics and emission of GRBs (e.g., Granot et al., 2018; Beniamini et al., 2020). Several works explored numerically a large range of jet parameters and different structures from the dynamical ejecta of neutron stars. Actually, most of these studies were performed in the context of short GRBs (e.g., Lazzati et al., 2018; Murguia-Berthier et al., 2021a; Pavan et al., 2021; Urrutia et al., 2021; Nativi et al., 2021)

In the case of long GRBs, the jet dynamics and structure were studied for example by López-Cámara et al. (2013, 2016); Gottlieb et al. (2020b); Gottlieb et al. (2020c); Matsumoto & Masada (2019). These works study the dynamics of the jet by changing different parameters, but employing a simple top-hat structure for the jet. As discussed in chapter 2, the central engine is expected to produce jets with a complex structure. Thus, in this chapter, we study structured jets in the context of long GRBs. The aim of this work is to study the dynamics and structure evolution of jets which are imposed with a wide range of structure and parameters.

We performed numerical simulations with The *Mezcal* code for different jet scenarios, in the context of long GRB. A $10M_{\odot}$ star progenitor was imposed by considering an analytical profile with a density which decreases as r^{-3}. We follow the dynamics of the jets until it reaches the edge of the star ($r \lesssim 10^{11}$ cm). We imposed top-hat and Gaussian structure for jets dominated by pressure or by kinetic energy. Furthermore, we change the jet luminosity and study the propagation of a structured Gaussian jet propagating through a supernova.

For pressure dominated jets, we show that its initial structure is washed out by the presence of recollimation shocks. For kinetic dominated jets, the structure vanishes due to high density progenitor environment. The progenitor contributes to the preservation of the final structure if the density is low (specially in the case of short GRBs) or the luminosity of the jet is high (in kinetic dominated jets).

3.1 Article abstract

After the detection of GRB 170817A, the first unambiguous off-axis gamma-ray burst (GRB), several studies tried to understand the structure of GRB jets. The initial jet structure (directly produced by the central engine) can be partially preserved, or can be completely modified by the interaction with the environment. In this study, we perform three-dimensional, special relativistic hydrodynamics simulations of long GRB jets evolving through a massive progenitor star. Different jet scenarios were considered: Top-hat, Gaussian jets dominated by pressure or by kinetic energy, as well as a model of a supernova (SN) plus a jet both propagating through the progenitor. We found that, while propagating inside the progenitor star, jets with different initial structures are nearly indistinguishable. Kinetic dominated jets are faster and more collimated than pressure dominated jets. The dynamics of jets inside the progenitor star strongly depends on the presence of an associated SN, which can strongly decelerate the jet propagation. We show that the initial structure of GRB jets is preserved, or not, mainly depending on the jet collimation. The initial structure is preserved in uncollimated jets, while the interaction with the medium may shape jets which move through dense environments, and may remain collimated.

3.2 Introduction

Gamma-Ray Bursts (GRBs) are bright, high-energy transients emitted by highly relativistic jets (see, e.g., Kumar & Zhang, 2015; Levan, 2018). GRBs are classified as short and long (SGRBs and LGRBs, respectively) based on their duration. SGRBs are associated with neutron star mergers and, possibly, neutron star-black hole mergers, while LGRBs are associated with the collapse of stripped envelope, massive stars, and the production of energetic supernovae.

In both short and long GRBs a pair of relativistic, collimated jets are launched from the central engine (i.e., the system composed by a compact object and an accretion disk) and produce the prompt gamma-ray emission. In addition, GRBs are accompanied by a long-lasting afterglow emission (over timescales of $\sim$ yrs in radio bands), produced by the deceleration of the relativistic blast wave. At distances $\gtrsim 10^{16}$ cm, the relativistic jet is decelerated by the large amount of ambient medium piled up by the jet head, and emits a multi-wavelength spectrum extending over most of the electromagnetic spectrum, from X-ray to radio bands (e.g., Sari et al., 1998; Granot & Sari, 2002; Zhang & MacFadyen, 2009; van Eerten & MacFadyen, 2012; De Colle et al., 2012a,b; Duffell et al., 2015; Gill et al., 2019).

The afterglow emission depends strongly on the angular structure of the jet (e.g., Granot & Kumar, 2003; Kumar & Granot, 2003; Granot, 2005; Salafia et al., 2015; Salafia et al., 2016), specially in GRBs seen off-axis as GRB170817A (e.g., Granot et al., 2018; Ghirlanda et al., 2019; Makhathini et al., 2020), while it is unclear if this is the case also for the prompt emission (see the review by Salafia & Ghirlanda 2022).

The structure of the jet launched from the central engine depends on several ingredients such as the presence of a black hole (and its spin) or a neutron star, the structure, mass and angular momentum of the accretion disk, the geometry and intensity of the magnetic field, and the neutrino transport and energy deposition (e.g., Kathirgamaraju et al., 2019; Nathanail et al., 2020; Janiuk et al., 2021; Gottlieb et al., 2022a; Gottlieb et al., 2022c,b).

Several authors have studied the interaction of the jet and the environment (i.e., the progenitor star in LGRBs and the debris of the compact object merger in SGRBs) by employing numerical simulations (e.g., Morsony et al., 2007; Lazzati et al., 2010; Bromberg et al., 2011b; Mizuta & Ioka, 2013; López-Cámara et al., 2013, 2016; De Colle et al., 2018a,b; Harrison et al., 2018; Lazzati et al., 2018; Gottlieb et al., 2020c; De Colle et al., 2021; Nativi et al., 2021; Urrutia et al., 2021). These works have explored how this interaction depends on the jet properties (luminosity and Lorentz factor) and its magnetization, on the jet opening angle and on the density stratification and velocity of the ambient medium. In all cases, the interaction of the jet with the dense surrounding medium decelerates the jet. The hot shocked material then expands laterally forming a cocoon, which in turn can collimate the jet. Three-dimensional (3D) simulations have shown that the amount of mixing between the jet and the ambient material determines the jet dynamics. Thus, low-density media reduce the jet deceleration and the amount of mixing, allowing the jet channel to remain more stable (Duffell et al., 2018; Hamidani et al., 2020; Nathanail et al., 2020; Murguia-Berthier et al., 2021a; Urrutia et al., 2021; Pavan et al., 2021; Lazzati et al., 2021; Gottlieb & Nakar, 2021; Nativi et al., 2021).

While the initial jet structure is most likely modified by the interaction with the environment, it remains to be fully understood if different jet structures produced by the central engine lead to different structures at the location where the jet emits electromagnetic radiation. If that is the case, future observations of a large sample of off-axis GRBs, coupled with detailed modeling, will give us insights on the structure of the jet at the launching point (i.e., information on the central engine itself). If not, it will remain impossible to recover this information by electromagnetic signatures alone[1].

[1]Future gravitational wave detectors as the Big Bang Observer or the DeciHertz Interferometer Gravitational wave Observatory may be able to detect gravitational waves produced directly by the relativistic jets, thus providing us information on the jets while they move inside the dense, optically thick environment (see Urrutia et al. 2022b).

In the case of SGRBs, Nativi et al. (2021) found that Top-hat or Gaussian jets are indistinguishable after evolving through a high-density medium (the ejecta of a neutron-star merger). Urrutia et al. (2021), though, found that while the initial structure of the jets (e.g., Top-hat, Gaussian, and power-law) is not preserved, the jets present different structures even after breaking out of the dense ambient medium.

In addition to the initial conditions of the jet and the environment, three key factors can affect the final structure of the jets. 1) The nature of the energy of the jets, that is, if the jets are pressure dominated (PD) or kinetically dominated (KD) (Martí et al., 2016; Matsumoto & Masada, 2019). 2) The magnetization of the jet. (Komissarov et al., 2007; Gottlieb et al., 2020b; Nathanail et al., 2020; Gottlieb et al., 2022c). 3) The presence of the accompanying type Ic supernova (SN) typically associated to LGRBs (see, e.g., Galama et al., 1998; Hjorth et al., 2003; Malesani et al., 2004; Pian et al., 2006a). Although the process leading to the formation of the jet and the SN is not fully understood, they are most likely produced by the same central engine (Woosley, 1993; MacFadyen & Woosley, 1999a). The interaction between the jet and the SN is not usually considered in numerical simulations, in which it is assumed that the jets propagate through the unperturbed progenitor star. Previous studies have shown that jets propagating through the cavity left from an expanding SN lead to a variety of possible outcomes (Komissarov & Barkov, 2007; De Colle et al., 2021).

In this paper we study the structure resulting from the propagation of 3D relativistic jets associated to LGRBs with 3D special relativistic hydrodynamical simulations (SRHDs). We run a series of models varying whether the jets are initially PD or KD, the jet structure (Top-hat or Gaussian), and the jet luminosity. We also consider the propagation of jets associated to a SN and show how the jet structure is strongly affected by this interaction.

The paper is structured as follows: in Section 3.3 we describe the code and the initial conditions employed in our simulations. In Section 3.4 we present the results of the numerical simulations. Finally, in Section 3.5 we discuss the results as well as their implications. In Section 3.6 we present the conclusions.

3.3 Methods

We run a set of 3D numerical simulations by using the adaptive mesh refinement code *Mezcal* (De Colle et al., 2012a), which solves the SRHD equations. The SRHD equations are integrated by employing a second-order solver (in space and time). The flux calculation is based on the HLLC Riemman solver (Mignone & Bodo, 2005), which low numerical dissipation at the contact discontinuity allows the development of instabilities

during the jet propagation (with respect to more diffusive methods, e.g. the HLL method).

We follow the dynamics of the jet during the first few seconds of propagation through the progenitor star, before the jet breaks out of the stellar surface. The computational domain extends between $x, y \in [-1.5, 1.5] \times 10^{10}$ cm and $z \in [0, 4.5] \times 10^{10}$ cm and is resolved (in Cartesian coordinates) by using $72 \times 72 \times 144$ cells along the x, y, z axis at the coarsest level of refinement. The progenitor through which the jet evolves has a radius of $R_\star = 10^{11}$ cm, and the jet is launched from a spherical boundary (mapped over the Cartesian grid) located at $r_j = 10^9$ cm with an opening angle θ_j, being $r = \sqrt{x^2 + y^2 + z^2} \leq r_j$ and $\theta = \arctan\left(\sqrt{x^2 + y^2}/z^2\right) \leq \theta_j$. In a cylindrical region, centered at the origin of the coordinate system, extended along the z-axis and with a radius of 5×10^8 cm, we set a maximum number of 6 levels of refinement. This corresponds to a minimum cell size $\Delta l \sim 10^7$ cm. Outside this high-resolution region, we set a maximum of 2 levels of refinement, corresponding to $\Delta l \sim 2 \times 10^8$ cm. The refinement criterion is based on density gradients. If $|\nabla\rho|/\rho \geq 0.4$ the mesh is refined, while the mesh is derefined for $|\nabla\rho|/\rho \leq 0.1$. Reflecting boundary conditions are used at the bottom boundary (i.e., the $z = 0$ plane). All other boundaries are set as outflow boundary conditions. The jet propagation is followed during a maximum of 13 s or until the jet arrives to the upper boundary of the computational box.

The progenitor ($M_\star = 10 M_\odot$), crossed by the jet during its propagation, is set by the following density profile (Harrison et al., 2018)

$$\rho(r) = \frac{A_0}{r^2}\left(1 - \frac{r}{R_\star}\right)^3 , \tag{3.1}$$

where $A_0 = 6 \times 10^{22}$ g cm^{-1} is a normalization constant, and $R_\star = 10^{11}$ cm is the stellar radius. The pressure of the progenitor was assumed as $P = 10^{-5}\rho(r)c^2$.

For PD jets, we consider the luminosity of the jet expressed as a function of the total energy (kinetic and thermal) per unit volume (ΔV) and unit time (Δt), i.e.

$$L_j = \left[\rho_j \Gamma_j^2 c^2 (\Gamma_j - 1) + 4\Gamma_j P_j\right] \Delta V/\Delta t , \tag{3.2}$$

where we assume an adiabatic index $\Gamma_{\rm ad} = 4/3$ for a relativistic gas. The jet luminosity is given by

$$L_j = \Gamma_\infty \dot{M} c^2 , \tag{3.3}$$

being Γ_∞ the asymptotic Lorentz factor and the mass injected in the jet per unit time is

$$\dot{M} = \left[\Gamma_j \rho_j\right] \Delta V / \Delta t \ . \tag{3.4}$$

By substituting expressions (3.3) and (3.4) in equation (3.2), the pressure of the jet takes the form

$$P_j \simeq \frac{\rho_j c^2}{4} \left(\frac{\Gamma_\infty}{\Gamma_j} - 1\right) \ . \tag{3.5}$$

Since the unit volume can be expressed as $\Delta V = v_j \Delta t \Delta S$, being ΔS the surface crossed by the jet and v_j its velocity, we can combine equations (3.3) and (3.4) and obtain the jet density

$$\rho_j = \frac{L_j}{\Gamma_\infty \Gamma_j v_j \Delta S c^2} \ . \tag{3.6}$$

For KD jets, we assume that the kinetic energy dominates the jet luminosity such that $L_j = \left[\rho_j \Gamma_j c^2 \left(\Gamma_j - 1\right)\right] v_j \Delta S$. In this case, the jet density is given as

$$\rho_j = \frac{L_j}{\Gamma_j \left(\Gamma_j - 1\right) c^2 v_j \Delta S} \ . \tag{3.7}$$

In this case, the jet pressure is assumed negligible, i.e. $P_j \sim 10^{-10} \rho_j c^2$. For both PD and KD jets we have $\Delta S = 4\pi(1 - \cos\theta_j) r_j^2$.

Also, the jets may either be defined with a Top-hat angular structure, or a Gaussian angular structure. In the Top-hat case the energy, density, and luminosity do not depend on the polar angle (except for the random perturbations described below), i.e. $f(\theta) = 1$ for $\theta \leq \theta_j$ and $f(\theta) = 0$. Meanwhile, in the Gaussian case $f(\theta) = \exp\left[-0.5(\theta/\theta_j)^2\right]$. The initial pressure angular profile of Top-hat and Gaussian jets (in the PD models, $P_{\rm PD}(\theta)$) is shown in Figure 3.1 (the pressure in the KD models is negligible). For either case, the luminosity and jet Lorentz factors are $L_j = L_{j,0} f(\theta)$ and $\Gamma_j = 1 + (\Gamma_{j,0} - 1) f(\theta)$, $\theta_j = 10°$, $\Gamma_{j0} = 5$, and $\Gamma_\infty = 400$. The main characteristics of the models[2] are shown in Table 3.1.

The jets are launched with either a luminosity $L_{j0} = 3.5 \times 10^{52}$ erg s^{-1} (high-luminosity, HL) or $L_{j0} = 5.3 \times 10^{50}$ erg s^{-1} (low-luminosity, LL). We also consider the effects that the presence of a supernova has on the jet dynamics. From $r = r_j$, we set a supernova explosion at $t = 0$ s. At $t_{\rm SN} = 1$ s, the jet is injected into the

[2]The jet is launched in the kinetic case with the same Lorentz factor as in the thermal jet (corresponding to a Lorentz factor $\Gamma = 5$), that is, with a Lorentz factor much smaller than what is suggested by observations. We notice that the ram pressure, which is independent of the jet Lorentz factor Γ_j, regulates the jet dynamics while the jet moves through the dense stellar medium.

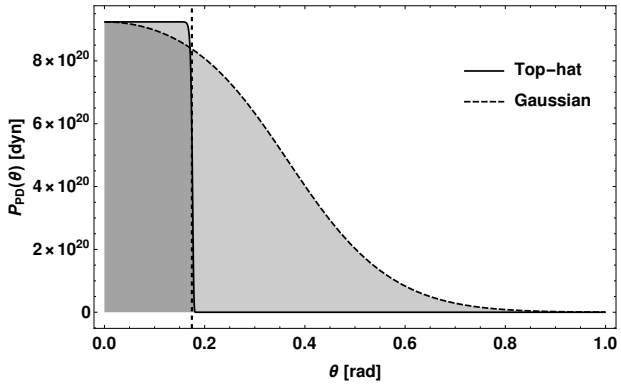

Figure 3.1: Initial pressure profile for the Top-hat and Gaussian pressure dominated jets ($P_{\rm PD}(\theta)$). The vertical dashed line corresponds to jet core angle $\theta_j = 10°$.

PD or KD	**Jet structure**	**Jet luminosity** (erg s^{-1})
PD	Top-hat	5.3×10^{50}
PD	Gaussian	5.3×10^{50}
PD + SN	Gaussian	5.3×10^{50}
KD	Top-hat	5.3×10^{50}
KD	Gaussian	5.3×10^{50}
KD	Top-hat	3.5×10^{52}
KD	Gaussian	3.5×10^{52}

Table 3.1: Jet models. Note: the jets with $L = 5.3 \times 10^{50}$ erg s^{-1} will be termed as LL while those with $L = 3.5 \times 10^{52}$ erg s^{-1} as HL.

computational box. Following De Colle et al. (2021), we inject the SN shock during $t_{\rm SN} = 1$ s, with a total energy of $E_{\rm sn} = 4 \times 10^{51}$ erg and a mass $M_{\rm sn} = 0.1 M_\odot$. We assume that 10% of the SN energy is thermal, while 90% is kinetic. The SN is assumed to be asymmetric, with an energy dependence $\propto \cos^2\theta$. The jet models analysed in this study are shown in Table 3.1.

In order to break the axial symmetry we impose small perturbations in the jet launching condition. First, we impose random perturbations of 1% in the jet density such that $\rho'_j = (1 + 0.01\Theta)\rho_j$ (being $0 \leq \Theta \leq 1$ a random number). Second, we impose a small random precession in the jet around the z-axis such that the angle between the jet and the z-axis is $\theta_0 = \Theta \times 1°$. Also, we impose a jet variability luminosity following a Heaviside step function $H(t)$, i.e., $L_{j0}(t) = L_{j0}\, H(t)$ with a period of 0.2 s as in López-Cámara et al. (2016).

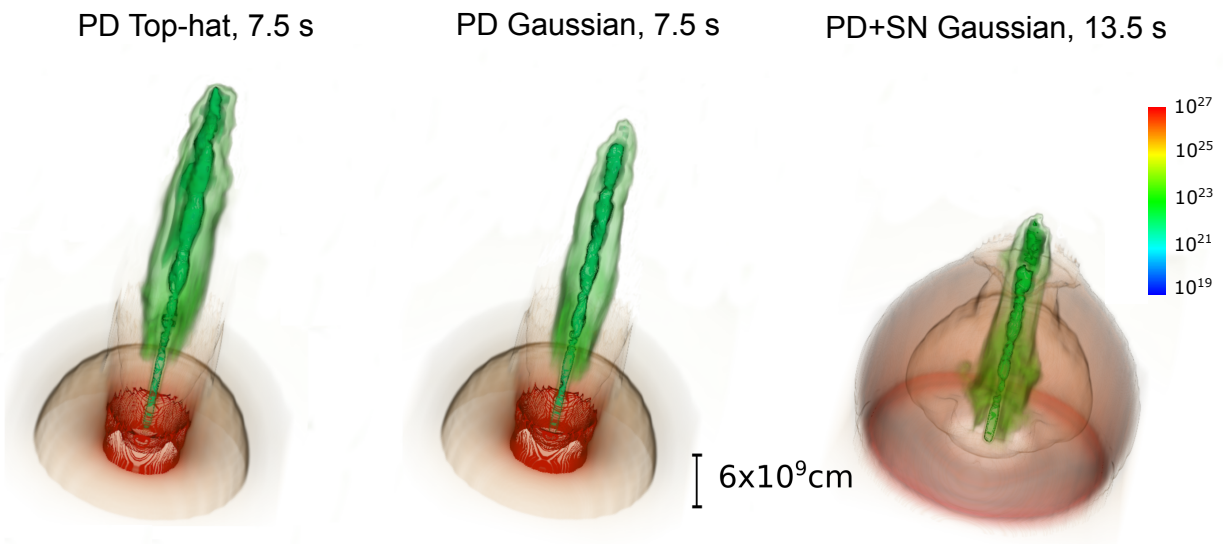

Figure 3.2: Number density (in units of cm^{-3}) volume rendering of the relativistic jets moving through the pre-SN progenitor. The PD Top-hat (left panel) and PD Gaussian (central panel) jet models are shown at $t = 7.5$ s. The case in which a PD Gaussian jet, launched with a delay of 1 s with respect to an associated SN explosion,is shown at 13.5 s (when the jet is about to break-out of the SN shock front, right panel). Note that in all cases the jet is within the progenitor ($R_\star = 10^{11}$ cm).

3.4 Results

To study the propagation of relativistic jets through the SN progenitor, we first analyzed the evolution of typical jet models employed for long GRBs (e.g., Morsony et al., 2007; Lazzati et al., 2010; Bromberg et al., 2011b; López-Cámara et al., 2013, 2016; Harrison et al., 2018; Gottlieb et al., 2020c; De Colle et al., 2021), this is, a set of models of a PD jet drilling through a massive stellar progenitor (with either a Top-hat or a Gaussian jet structure). Figure 3.2 shows the evolution of PD jets through the envelope of the progenitor (Top-hat jet: left panel, and Gaussian jet: central panel). Specifically, we show a volume rendering of the number density (cm^{-3}) of the relativistic jets moving through the massive stripped-envelope progenitor at $t = 7.5$ s. The main components are clearly seen: the progenitor (in brown), the jet and cocoon (in green), and the funnel created by the jet-cocoon as it drills through the progenitor (in red). Note that the jet and cocoon are in all cases within the envelope of the progenitor (which has $R_\star = 10^{11}$ cm and for which the breakout time is ∼11 s).

Figure 3.3 shows 2D number density stratification maps along the $y = 0$ cm plane (upper panels), and Lorentz factor stratification maps (lower panels) for different models at various times. For the PD Top-hat and PD Gaussian jets, we show the evolution of a jet (with $L = 5.3 \times 10^{50}$ erg s^{-1}) through the pre-SN progenitor at 5 s and 7.5 s (Top-hat: left-most panels, and Gaussian: center-left panels). The jet propagation depends on

the initial structure (Top-hat vs Gaussian models), being slower by $\lesssim 10\%$ the propagation of structured jets with respect to Top-hat jets. While the velocity is slightly smaller in the Gaussian jet, the general morphology remains very similar in the two models. For both the Top-hat and Gaussian models, as the pressure of the jet is larger than the pressure of the cocoon, the jet expands laterally until pressure equilibrium is achieved. Then, the material bounces back towards the axis of symmetry, producing recollimation shocks (visible at the base of the jets). The material in the PD jet is relativistic ($\Gamma \gtrsim 5$), and some acceleration is present beyond the recollimation shocks, with the jet velocity arriving to Lorentz factors of $\sim$ several tens. At larger distances, the jet Lorentz factor drops substantially, going from $\Gamma \sim 30$ below the recollimation shocks, to $\Gamma \sim 5$ at larger values of z.

As the PD jet evolves through the envelope, the head of the jet decelerates to sub-relativistic speeds due to the interaction with the dense medium of the progenitor star. The post-shock region is formed by: a) the shocked jet material, formed by material traveling along the jet channel and crossing the reverse shock; and b) the shocked stellar material, formed by stellar plasma heated and accelerated by the forward shock. The post-shock, hot material then expands laterally, forming an extended cocoon which collimates the jet. The cocoon formed by the lateral expansion is sub-relativistic ($\Gamma \gtrsim 1$) as deduced by the fact that the cocoon is not visible in the bottom panels of Figure 3.3. Due to the high velocity differences, the contact discontinuity separating the jet and the cocoon is unstable (Matsumoto et al., 2021). Then, material close to the contact discontinuity becomes turbulent, which leads to mixing of the stellar and jet material in the cocoon and in the jet. This mixing pollutes the relativistically moving material, dropping substantially its velocity. The latter is visible, for example, at $t = 5$ s for the Top-hat PD jet at $z/c \approx 0.5 - 0.6$. The small perturbations injected in the jet launching boundary lead to a wiggling of the material in the jet which decelerates the jet, and to the formation of blobs along the jet axis.

Since the relativistic jets of long-GRBs may be dominated by kinetic energy, we also analyzed how KD jets evolve through the pre-SN progenitor. Note that the luminosity of the KD jet and the progenitor were the same as those of the PD models. Figure 3.3 also shows the evolution of KD jets through the progenitor at 5 s and 7.5 s (Top-hat: center-right panels, and Gaussian: right-most panels). Once more, the Gaussian jets are slower than the Top-hat jets, recollimation shocks are present, blobs along the jet axis are formed, and the cocoon is also sub-relativistic. KD jets, though, are quite different both in morphology and dynamics (with respect to the PD jets). KD jets are denser, more collimated, and faster (covering the same distance in about ~ 0.5 of the time). The KD jets remain with basically the injected Lorentz factor ($\Gamma \approx 5$) but move

faster than the PD jets due to the higher collimation. As an obvious consequence of their low thermal energy, recollimation shocks are much less evident in KD jets. Also, the wiggling of the jet and the creation of blobs are less evident.

We also explore the (more realistic) scenario in which the GRB and the SN are present. Based on the discussion of the lag between the GRB and the SN of De Colle et al. (2021), we assume that the SN takes place 1 s before the jet. The right panel of Figure 3.2 shows the evolution of a PD jet. Specifically, we show the volume rendering of the number density (in units of cm^{-3}) of a PD Gaussian relativistic jet and its cocoon as it moves through a SN which in turn expands through the progenitor at t = 13.5 s (when it is about to break out of the SN).

As the SN expands through the progenitor, it produces a dense front which will later affect the evolution of the jet (see Figure 3.3). General features of the jets as the collimation, the presence of recollimation shocks, wiggling of the jet and blobs are common also to this model (see the central panels of Figure 3.3). On the other hand, the dynamics of jets associated with SNe is dramatically different with respect to the other cases considered. The jet, injected with the same luminosity as the PD model and with a 1 s lag after the SN, first propagates inside the SN cavity which moves through the progenitor. Thus, the jet will be affected by the density stratification produced by the SN. The PD Gaussian jet has to drill through a medium which is $\sim$ one order of magnitude larger when the SN was previously launched compared to when no SN is present (compare the case of the PD+SN Gaussian jet at t = 5 s against the PD Gaussian jet at t = 3 s). At the injection point the density of the star is $\rho_\star(r_j) \approx 37 \times 10^{27}$ cm^{-3}, dropping to $\approx 8 \times 10^{27}$ cm^{-3} at $r/c \approx 0.07$, then decreasing as $\sim r^{-3}$. On the other hand, the supernova cavity has a density $\rho_{\mathrm{SN}} \approx 5 \times 10^{27}$ cm^{-3} at $r = r_j$. After 1 s of evolution, the supernova reverse shock is located at $r/c \approx 0.07$, with a density $\rho \approx 1 \times 10^{27}$ cm^{-3} in the unshocked SN ejecta, and $10 - 40 \times 10^{27}$ cm^{-3} in the shocked ejecta and stellar SN material. That is, the jet moves at the beginning inside a cavity left from the expanding SN, then choke against the expanding SN shock front, which has a much larger density with respect to the progenitor star (at the same radius).

As a result of the density stratification produced by the SN in its way through the star, the jet propagation is faster as it moves through the SN cavity, and slower once it starts interacting with the denser SN shock front (with respect to the case without SN). Also, as a result of the larger density profile produced by the SN, more energy is deposited in the cocoon (which is slightly more extended). Mixing from the inner part of the cocoon with the jet channel leads to interruption of a continuous supply of relativistic material from the jet into the head, thus leading to a further deceleration of the jet.

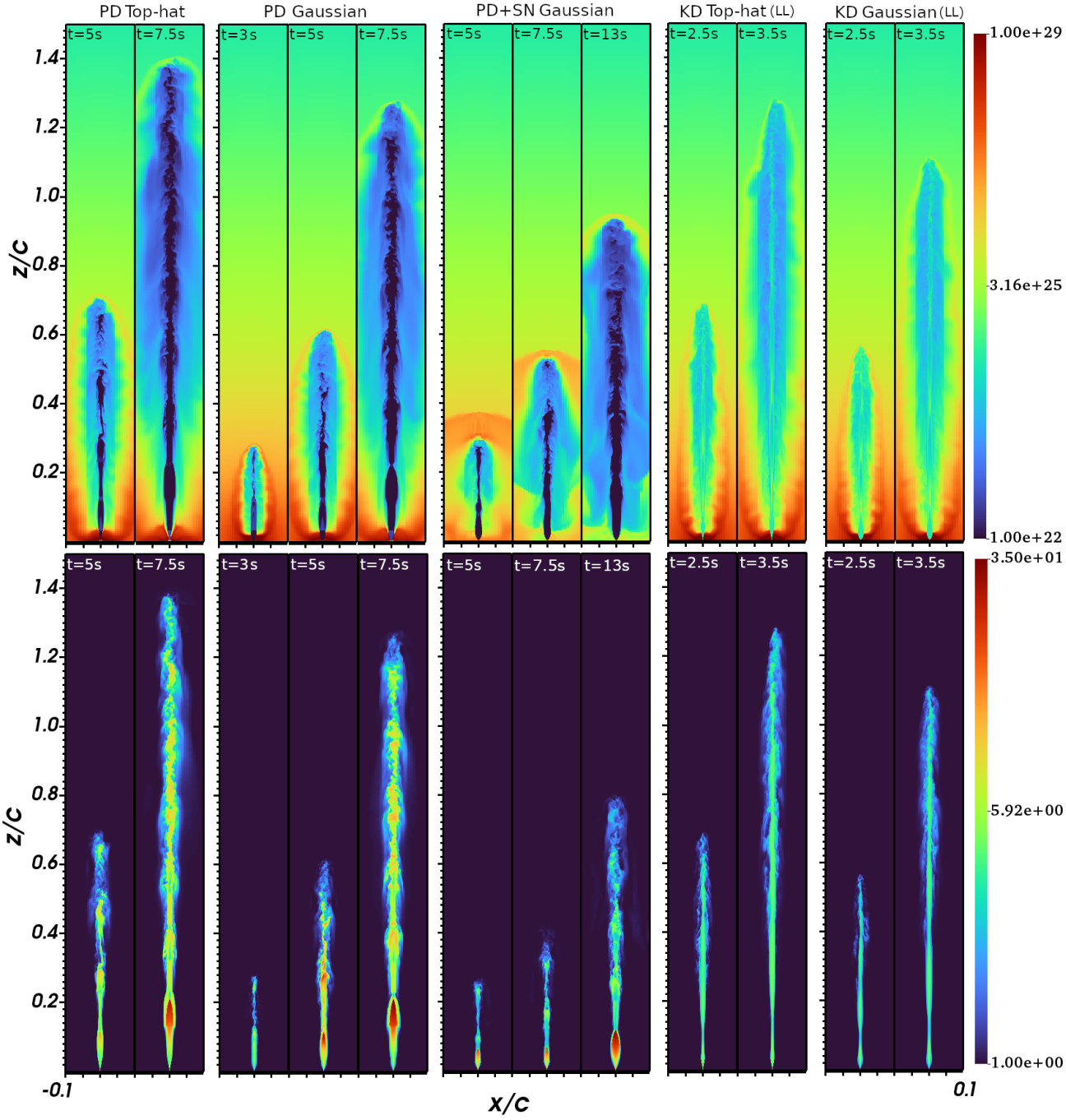

Figure 3.3: Two-dimensional number density (in units of cm^{-3}, upper panels) and Lorentz factor (lower panels) stratification maps of the models considered in this study (see Table 3.1). From left to right panels: PD Top-hat jet at 5s and 7.5s; PD Gaussian jet at 3s, 5s and 7.5s; PD Gaussian jet with a SN (ejected 1s previously than the jet) at 5s, 7.5s, and 13s; KD Top-hat jet at 2.5s and 3.5s; and KD Gaussian jet at 2.5s and 3.5s. The axis are normalized to c.

In addition to the models discussed above, we also studied the evolution of a very energetic jet (KD-HL, see Table 3.1). This jet has a luminosity much larger than the one expected for GRBs, but will guide our understanding of the dependence of the break out time and the velocity of the jet head as a function of luminosity. In this case, the jet velocity is close to the speed of light already deep inside the star. The HL jets present basically the same evolution and morphology as the LL case (same density and Lorentz values for the jet and cocoon, and collimation). As expected, the HL jets propagate faster than the LL jets.

The most notable effects on the jet head velocity are produced by: a) changing the total jet energy (i.e. more powerful jets move faster); b) if the jet is PD or KD; and c) by the presence of SN moving through the progenitor prior to the jet. To illustrate how the different conditions of the jet (PD or KD, the jet structure, presence of the SN, and the jet luminosity) modify the jet dynamics, in figure 3.4 we plot the position of the jet head ($R_{\rm jh}$) along the polar axis as a function of time. In all cases, the KD jets are much faster than the PD jets (with the Top-hat structure producing a faster evolution than a Gaussian structure). For the PD jet models with no SN the $R_{\rm jh}$ accelerate from $v_{\rm jh} \approx 0.05\ c$ to $v_{\rm jh} \approx 0.6\ c$ as they approach the stellar surface (notice that these are average velocities, which implies that the local head velocity is larger). The KD jet models accelerate faster and reach higher velocities ($v_{\rm jh} \approx 0.6 - 0.9\ c$). The case of a jet propagating into a SN looks quite different. The jet head moves behind the shock front of the SN at a $\sim$ constant velocity of $v_{\rm jh} \lesssim 0.1$ c. The jet head velocity will remain close to that of the SN until when it breaks out of the SN shock front. Then, it will accelerate as it moves through the much lower density medium.

Figure 3.5 shows the energy per solid angle computed when the jet head is located at $R_{\rm jh} = 4.47 \times 10^{10}$ cm. All curves tend to follow a power-law distribution. The PD jet models follow $dE/d\Omega \propto \theta^{-1.5}$, the KD jet models follow $\theta^{-1.8}$ and $\theta^{-2.5}$ (for the LL and HL, respectively), and the PD+SN jet model follows $\theta^{-0.5}$. Independently if the jets are PD or KD, both Top-hat and Gaussian jets have the same angular distribution. In jets associated to a SN, the energy distribution is much less asymmetric, with the SN dominating at large polar angles.

Although we simulated the propagation of the jet inside the star, we can determine the breakout times by extrapolating the expansion of shock front[3]. We found that the Top-hat PD jet has a breakout time $t_{\rm bo} = 10.6$ s, similarly to Harrison et al. (2018); Morsony et al. (2007); López-Cámara et al. (2016). We get $t_{\rm bo} = 11.2$ s for the gaussian PD models, $t_{\rm bo} = 5.8$ s and $t_{\rm bo} = 6.1$ s for the Top-hat and Gaussian KD-I models, $t_{\rm bo} = 3.5$

[3]The extrapolation was performed by fitting the curves shown in Figure 3.4 with the function $R_{\rm jh}(t) = a\, t^b + c\, t$, being t the evolution time. The parameters a, b, c were determined by employing the least square method. The breakout time $t_{\rm bo}$ is then the root of the polynomial equation evaluated at $R_{\rm jh}(t_{\rm bo}) = R_\star = 10^{11}$ cm.

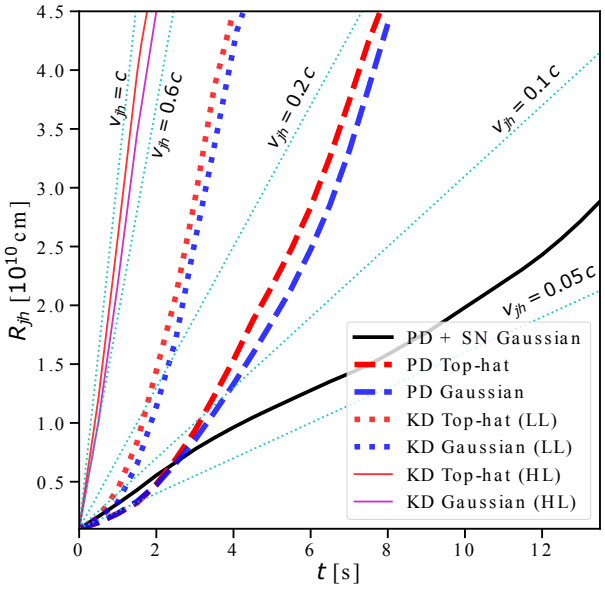

Figure 3.4: Position of the jet head ($R_{\rm jh}$) as a function of time for the different models. The thin dotted lines correspond to constant head velocities ($v_{\rm jh}$).

s and $t_{\rm bo}$ = 4.1 s for the Top-hat and Gaussian KD-II. Finally, the SN model reaches the stellar surface at $t_{\rm bo}$ = 57.3 s.

3.5 Discussion

In this section, we will discuss the differences in the jet dynamics and morphology resulting from the different jet initial conditions (Section 3.5.1). Although our simulations show that injecting Gaussian or Top-hat jets lead to a similar jet structure *inside the progenitor star*, we also discuss under which circumstances different initial jet structures are at least partially preserved *once the jet breaks out of the stellar surface and interacts with the circumstellar medium* (Section 3.5.2). If the initial jet structure is preserved to a certain degree, then, a large sample of observed off-axis GRBs, coupled with numerical calculations, could provide indirect insights on the physics of the central engine and the jet itself.

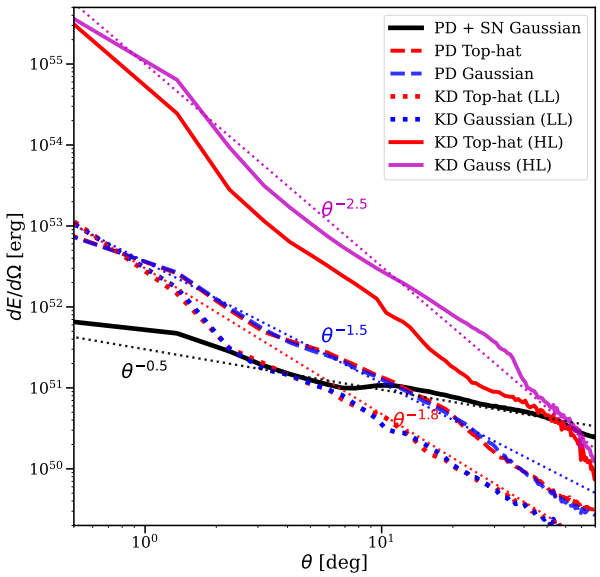

Figure 3.5: Energy per solid angle as a function of the polar angle for the models shown in Figure 3.4 when the correspondent jet head is at $R_{jh} = 4.47 \times 10^{10}$ cm. The thin dotted lines correspond to the indicated power laws ($\propto \theta^{-n}$).

3.5.1 Jet dynamics and morphology

We have performed 3D, SRHD simulations of relativistic jets propagating through a massive progenitor. The jets may have initially Top-hat or Gaussian structures, and may be either PD or KD. In addition, the jets may be linked to an accompanying SN and will propagate first through a cavity produced from the SN.

Our simulations show that as the jets evolve through the progenitor, the morphology of the jets are basically independent if their initial structure is Top-hat or Gaussian (see Figure 3.5). Gaussian jets though, are slightly slower. On the other hand, whether the jets are PD or KD does produce different morphology and dynamics, being KD jets more collimated and with less energy in the cocoon (see figures 3.3 and 3.5).

In Figure 3.5, the energy distribution for the PD top-hat model was computed at $t \approx 0.75\, t_{\rm bo}$. The jet core and power-law distributions observed in our simulations ($1.5 - 2.5$) are similar to those of Gottlieb et al. (2020c) (which find a power-law index of $1 - 3$). Based on the temporal evolution shown in Figure 4 of Gottlieb et al. (2020c), the power-law index is expected to slightly increase as the shock head approaches the surface of the star. On the other hand, the power-law energy distribution observed in the jet plus supernova case is very different to what is typically associated to isolated jets (as the energy distribution at large angles.

The dynamics of the jet head can be understood by balancing the ram pressure of the material shocked by the forward and reverse shocks, i.e. (see, e.g., Matzner, 2003)

$$\rho_j c^2 h_j \Gamma_j^2 \Gamma_h^2 (\beta_j - \beta_h)^2 + P_j = \rho_a c^2 h_a \Gamma_h^2 \beta_h^2 + P_a \ , \tag{3.8}$$

where ρ_j, h_j, Γ_j, β_j, and P_j, are the density, enthalpy, Lorentz factor, velocity and pressure of the jet (respectively); Γ_h, β_h are the Lorentz factor and velocity of the jet head; and ρ_a, h_a, and P_a are the density, enthalpy, and pressure of the ambient medium. In the case of a strong shock ($P_j \gg P_a$) the ambient mediums satisfies $\rho_a c^2 \gg P_a$ and $h_a \simeq 1$. Also, the jet pressure P_j is a factor $\sim \Gamma_j^2$ smaller than the first term in the left hand side of equation (3.8). Additionally, if the jet is not cylindrical then its ram pressure at the head location will drops by a geometrical factor $(R_{\rm j}/R_{jh})^2$ (where $R_{\rm j}$ and $R_{\rm h}$ are the sizes of the jet at its base and at the location of its head, respectively). Thus, taking into account the previous assumptions, the jet velocity will be:

$$v_h = \frac{v_j}{1 + (\rho_a/\rho_j h_j \Gamma_j^2)^{1/2} R_{\rm jh}/R_j} \ . \tag{3.9}$$

Equation 3.9 shows that jets move faster in lower density media (that is, when $\rho_a \lesssim \rho_j h_j \Gamma_j^2$) and when it is more collimated (when $R_{\rm jh} \gtrsim R_j$). Gaussian jets move slower since they have a slightly lower luminosity in the core of the jet, with respect to Top-hat jets. KD jets are faster since they are more collimated than the PD jets (as their lower thermal pressure lead to less prominent recollimation shocks).

Martí et al. (2016) studied the evolution of jets with different types of energy (PD or KD), including also magnetic contributions. In their two-dimensional special relativistic, magneto-hydrodynamic simulations they found that PD jets have a rich internal structure with several recollimation shocks, while recollimation shocks are mostly suppressed in KD jets. Our 3D SRHD simulations confirm these findings. In addition, we found that KD jets also present mixing in the jet channel (as in the simulations by Matsumoto & Masada 2019), and a larger velocity (by a factor of ~ 2) with respect to PD jets.

The mechanism leading to the jet formation is not well established. In the case of magnetohydrodynamic jets, Komissarov et al. (2007) showed that about $\sim 50\%$ of the magnetic energy has been transformed into kinetic energy at distances $r \lesssim 10^9$ cm. In an uncollimated (i.e., conical) PD jet, the acceleration process is very efficient, with a Lorentz factor $\Gamma_j \propto r$. In this case, jet material launched from the central engine with a Lorentz factor of ~ 10 close to the central engine ($\sim 10^6$ cm) will convert most of its thermal energy into kinetic once it arrives to $\sim 10^7$ cm. If the jets are collimated, the recollimation shocks limit the region where

the acceleration happens (see for example Figure 3.3 in which the jet material is accelerated from $\Gamma_j = 10$ to $\Gamma_j = 30$).

Several studies have discussed the formation and effects of instabilities near the jet core and find that the mixing can strongly decelerate the jet or even stop its propagation (e.g., López-Cámara et al., 2016; Harrison et al., 2018; Matsumoto & Masada, 2019; Gottlieb et al., 2020a,c). However, our results show that decreasing the thermal pressure in the jet makes it more collimated, stable, and faster during its propagation. Magnetic fields in the jet may also reduce the mixing and stabilize the jet (Gottlieb et al., 2020b; Nathanail et al., 2020).

We have shown that the presence of an associated SN affects strongly the propagation of the jet. At the beginning, the jet moves through a cavity (whose extension strongly affects the outcome of the system). When the cavity interacts with the SN shock front, the jet slows down dramatically. It is expected that the jet will break out of the expanding SN, nevertheless, the presence of the SN increases the breakout time and may even inhibit such break out (De Colle et al., 2021).

3.5.2 Is the jet structure determined by the ambient medium or by the central engine?

In our simulations, different initial structures may lead to different structures only for jets with very large luminosity. This does not imply necessarily that the initial jet structure is completely lost in LGRB jets once the jets break out of the star and accelerate into the low-density, external medium. At least two physical parameters must be considered to properly address this issue: the density of the environment and the jet properties (luminosity, opening angle, Lorentz factor, etc) at the launching point.

If the jet propagates through a low-density ambient medium, then the jet may remain conical during its propagation. Also, the jet head will move with constant speed, the energy deposited into the cocoon will be small, and the jet will remain uncollimated. This corresponds to the case $\tilde{L} > \theta_j^{-4/3}$ (where $\tilde{L} = \rho_j h_j \Gamma_j^2 / \rho_a$, see Bromberg et al. 2011b). This condition corresponds to $L_j/(c^3 \rho_a S)$, where S is the surface from where the jet is injected, i.e. $S = 4\pi(1 - \cos\theta_j) r_j^2 \simeq 2\pi\theta_j^2 r_j^2$. Thus, jets will be uncollimated if

$$\rho_a \lesssim 27 \text{ g cm}^{-3} \left(\frac{L_j}{10^{51} \text{ ergs s}^{-1}}\right) \left(\frac{\theta_j}{0.1}\right)^{-2/3} \left(\frac{r_j}{10^9 \text{ cm}}\right)^{-2} . \tag{3.10}$$

For densities below this value, the jet will be uncollimated, and the initial conditions will be (at least in part) preserved during the jet evolution. In the stellar progenitor used in this paper, we have $\rho_a = 6 \times 10^4$ g cm^{-3} at $r = 10^9$ cm. This result is consistent with the fact that the jets in our simulations are collimated. In LGRBs

jets, if the jet moves through the dense stellar progenitor, its velocity will be reduced and the structure of the jets at the breakout will be affected by the medium (Irwin et al., 2019; Eisenberg et al., 2022; Gottlieb et al., 2022b; Suzuki & Maeda, 2022).

For SGRBs, the jets will remain uncollimated if the wind mass-loss $\dot{M}_w$ is:

$$\dot{M}_w < 1.5 \times 10^{-3} \left(\frac{L_j}{10^{51} \text{ ergs s}^{-1}} \right) \left(\frac{\theta_j}{0.1} \right)^{-2/3} \left(\frac{r_j}{10^9 \text{ cm}} \right)^{-2} \left(\frac{v_w}{0.3c} \right), \tag{3.11}$$

where we have considered a wind velocity of $0.3c$. Envelope masses between $10^{-6} M_\odot - 10^{-2} M_\odot$ are expected in the case of SGRBs (Dudi et al., 2021; Foucart et al., 2021; Dean et al., 2021; Combi & Siegel, 2022; Murguia-Berthier et al., 2021b; Desai et al., 2022; Kullmann et al., 2022). The initial structure of the jet is not affected if it evolves through a thin medium (e.g., $10^{-4} M_\odot$) - see Urrutia et al. 2021, while the structure of the jet is affected for denser media ($10^{-2} M_\odot$, see Nativi et al. 2021).

Since the jet velocity depends non-linearly on the jet luminosity[4], then the jet dynamics will be very different if the jet is launched with different luminosities or time-luminosity histories (see for example López-Cámara et al., 2014, 2016). If the jet luminosity is very large, the jet crosses the inner regions of the stellar envelope at high speeds. While considering a constant, large luminosity is nonphysical (as the total energy will be much larger than the jet energy inferred from GRB observations, i.e. $10^{51} - 10^{52}$ erg), the same outcome can be obtained if the jet luminosity per unit solid angle varies on time (reaching larger initial luminosities then presenting a quick drop). The jet luminosity variability may be due to the varying mass accretion rate onto the compact object (from the depleting accreting disk present around it, see, e.g., Lopez-Camara et al., 2009). This kind of time-variable luminosity history has been observed e.g. in relativistic jets produced during some tidal disruption events, with an initial constant luminosity lasting ∼week, then dropping as $t^{-5/3}$ (see, e.g., De Colle & Lu 2020 and references therein). Thus, the larger initial luminosity could help the jet to propagate through the denser inner regions of the progenitor as it deposits less energy in the cocoon, reducing the jet collimation and helping to preserve the initial structure of the jet.

As shown in Figure 3.3, recollimation shocks are present along the jet channel. These recollimation shocks wash out the initial jet structure. Thus, the fate of the structure of the jet is affected by the timescale needed for jet to become uncollimated, which will eventually happen (if the jet lasts long enough) since the expanding cocoon drops its density and pressure with time. On larger timescales, the jet will inject most of its energy into a channel crossing the environment without strongly interacting with it (see, e.g., Gottlieb et al., 2020c).

[4]From $L_j \propto \rho_j$ and equation 3.8.

Most of the energy deposited during this phase will travel unperturbed towards larger distances. Future studies are needed to clarify this issue.

Finally, we notice that GRBs show a large dispersion in the isotropic energy (10^{48} – 10^{54} erg, see, e.g., Figure 1 of Perley et al. 2014). Assuming that most of these GRB jets are observed within their core opening angle θ_j, this dispersion is strongly reduced to a jet energy $E_j \sim \theta_j^2 E_{\rm iso}/2 \sim 10^{51}$ erg (Frail et al., 2001). An alternative explanation assumes that GRB jets have a "universal" angular structure $dE/d\Omega \propto \theta^{-2}$, and that GRBs with different energies are the produced by jets seen at different observing angles (see, e.g., the review by Salafia & Ghirlanda 2022 and references therein). From our findings the latter is unlikely, unless the jet structure produced by the central engine and that given by the interaction with the environment are similar for all the GRBs.

3.6 Conclusions

In this work, we study the propagation of 3D SRHD structured LGRB jets evolving through the dense envelope of a progenitor star. The jets were implemented as Top-hat or Gaussian jets whose energy was either PD or KD. In addition, we performed a simulation of a SN plus a lagged jet both propagating through the progenitor.

PD jets present strong recollimation shocks which are absent in KD jets. Then, KD jets drill faster through the progenitor, and are more stable. Also, KD jets are characterized by a lower amount of mixing. While in PD models the jet channel is polluted by cocoon material (diminishing the velocity of the jet), this is not the case in KD jets. Depending on its nature, the jets present different angular energy distribution, being steeper in the KD jet case. Jets propagating firstly through the cavity left from an accompanying SN evolve differently from when no SN is present. While the jet moves faster initially through the SN cavity, it strongly decelerates once it interacts with the SN shock front. Our simulations illustrate the need to explore further in detail the interaction of the jet with the accompanying SN.

The initial structure of the jets does not play an important role during their evolution through the progenitor, as the Top-hat and Gaussian jets end very similar to each other. The numerical simulations presented in this work, though, describe the jet dynamics as it moves through the progenitor. The structure of the jet will be preserved if the jet remains uncollimated (i.e., if the jet moves through a low-density environment), which is unlikely in LGRB jets.

As the cocoon expands through the progenitor, the density and pressure of the medium close to the base of

the jet drops. Thus, if the jets are long-lasting they can become uncollimated and preserve the initial conditions at late times. In this case, off-axis LGRBs with different times duration may show different afterglow behaviors at early times (this is, before the decelerating jet core enters into the observer field of view). The structure of short-lasting LGRBs will reflect the interaction of the jet with the dense medium, while long-lasting LGRBs will depend on the structure of the jet at the injection point. Direct observations of a large sample of GRB afterglows will help to constrain the density stratification of the environment, the initial structure of the jet, and the physics of the central engine itself.

Chapter 4

Numerical Simulations of Structured Jets at large scales

Este capítulo es la versión preliminar de un artículo que se enviará a Monthly Notices of the Royal Astronomical Society como: Urrutia et. al. (2022c), *Numerical Simulations of Structured Jets at large scales*.

Solving the complete GRB evolution in a single run, from the central engine to the end of the deceleration phase, is a very challenging task. As a consequence, the propagation of a relativistic jet is typically solved by studying, separately, different stages of the GRB evolution. Simulations of the region around the central engine study the jet launching. In this thesis, motivated by the GRB 170817A, we studied the evolution of the jet at small scales (as the jet moves into the progenitor medium) and determine its afterglow based on the final structure of the jet. Finally, the last stage of the GRB evolution corresponds to its deceleration stage. In this phase, the jet is typically solved by considering a blast wave described by the self-similar solution Blandford & McKee (1976) while the light curves are predicted on a wide range of frequencies (Sari et al., 1998; Granot & Sari, 2002). In previous calculations, the dynamics of top-hat jets and their afterglow emission has been studied in detail (e.g., Zhang & MacFadyen, 2009; De Colle et al., 2012a). However, these studies considered a simple top-hat for the jet Lorentz factor, density and pressure. The observations of GRB 170817A, on the other hand, are consistent with the deceleration of an extended cocoon. In this work, we consider the deceleration of collimated jet couple with a structured cocoon, and we calculated the resulting afterglow light curves.

We run numerical simulations of jets that start their evolution from large scales, initially $r \sim 10^{16}$ cm. We implement the structured jets following the self-similar model by Blandford & McKee (1976). Likewise, we follow the evolution during 2.6×10^6 days and compute the light curves by post-processing the results of the simulations.

We found that the structure of the jet at large scales strongly affects its dynamics, that the lateral expansion is different from the early phases of the simulation while it becomes similar once the jet becomes nearly spherical at very late times. As a consequence, the shape of the light curves are modified. These results imply that numerical simulations provide a better description than analytical models which assumes that the structure of the jet is preserved.

4.1 Abstract

So far most numerical simulations have used a conical wedge from the Blandford-McKee (BM76) spherical, ultra-relativistic, self-similar solution to model the afterglow dynamics and emission of gamma-ray bursts (GRBs). However, many physical processes could change the structure of GRB jets before the afterglow stage, making them differ from the BM76 morphology. This study investigated the dynamics of seven structured jets models and their consequences on the afterglow radiation through two-dimensional special relativistic hydrodynamics (SRHD) simulations. Our jet models were implemented by replacing a typical BM76 conical wedge with a novel implementation of structured jets described by angular profiles of energy and Lorentz factors and followed during the decelerating phase. By post-processing the simulation outputs, we calculate synthetic afterglow light curves for several off-axis observers. Our results show that: 1) our new implementation is viable to describe more realistic jet dynamics during the afterglow phase. 2) The shape of the light curves is substantially distinct in jets with different structures, under the right conditions, it is possible to distinguish the jet structure by its radiation. 3) We provide an afterglow light curve catalogue of structured jets for several viewing angles $\theta_{\rm obs} \in [0, \pi/2]$. 4) A fit with observations of GRB 170817A shows that the parameters are strongly degenerate, therefore the jet structure is still undetermined.

4.2 Introduction

Gamma-Ray Bursts (GRBs) are produced as the result of the propagation of relativistic jets. Hydrodynamic quantities such as density, pressure, and energy, play an important role in the computation of light curves radiation (e.g., Granot & Sari, 2002; Granot & Ramirez-Ruiz, 2010; De Colle et al., 2012a).

During the first milliseconds after the jet launching, in the context of Short GRBs (SGRB), the rotation of the compact object, magnetic fields and the accretion disc structure play an important role in determining the jet morphology (e.g., Rosswog et al., 2003; Rezzolla et al., 2011; Makhathini et al., 2020). Annihilation processes and rotation effects produce a toroidal neutrino-driven wind which changes in the jet dynamics (e.g., Ramirez-Ruiz et al., 2002; Aloy et al., 2005; Dessart et al., 2009; Murguia-Berthier et al., 2014; Perego et al., 2014; Murguia-Berthier et al., 2017a; Murguia-Berthier et al., 2021a). GRB jets acquire their structure as the result of the interaction between the initial jet with the surrounding medium. Then, the jet material spreads laterally, beyond its initial opening angle θ_j. When the jet reaches the edge of the neutrino-driven wind for SGRBs or the surface of the massive star for LGRBs, it breaks out into a much less dense medium. The

later expansion of entropy-rich material leads to the formation of an extended cocoon (Begelman & Cioffi, 1989; Morsony et al., 2007; Bromberg et al., 2011b; López-Cámara et al., 2013; Murguia-Berthier et al., 2014; López-Cámara et al., 2016; Murguia-Berthier et al., 2017a; Lazzati et al., 2020; Murguia-Berthier et al., 2021a; Gottlieb et al., 2020b; Gottlieb et al., 2020c; Nathanail et al., 2020).

GRBs are typically not resolved spatially in the sky, with a few exceptions in which VLBI observations provide partial information on the shape of the emitting region (i.e., GRB 030329 - see Mesler et al. 2012 - and GRB 170817A - Mooley et al. 2018). Therefore, their structure can, in general, be determined only by employing indirect methods. The relativistic velocity of GRBs jets implies that radiation is strongly beamed. Then, GRBs are mainly detected when seen *on-axis*, while they are weaker emitters for *off-axis* observers. This also implies that only a small fraction of the jet core is observed, while the region outside the jet core is not typically observed.

After, the first *off-axis* from GRB 170817A (i.e., seen at an observer angle larger than the jet core opening angle, i.e, $\theta_{\rm obs} > \theta_j$) several authors have studied the jet structure. The atypical light curve of this GRB has been well explained by different structured jet models (e.g., Granot et al., 2018; Ghirlanda et al., 2019; Lazzati et al., 2018; Gill et al., 2019; Beniamini et al., 2020; Makhathini et al., 2020; Urrutia et al., 2021). The angle of observation have been constrained as $\theta_{\rm obs} \approx 20^\circ - 30^\circ$.

The afterglow emission is typically computed by adding the contribution of each piece of fluid and assuming that it evolves as a self-similar blast wave (Blandford & McKee, 1976; Granot & Sari, 2002). Calculations of afterglow radiation have been often performed by assuming top-hat jets (e.g., van Eerten & MacFadyen, 2012; De Colle et al., 2012a). The radiation of structured jets has been computed by considering angular profiles of energy $E_j(\theta)$ and Lorentz Factor $\Gamma_j(\theta)$, and assuming that each slice of fluid evolves independently as a fraction of a spherical BM76 blast wave. Different studies have shown that the jet structure can change substantially the afterglow radiation for off-axis observers (e.g., Granot, 2005; Granot, 2012; Granot et al., 2018; Lazzati et al., 2018; Ghirlanda et al., 2019; Gill et al., 2019; Beniamini et al., 2020).

Some of the approximations usually employed in the calculation of afterglow radiation from structured jets lead to imprecise results. Analytical studies assume a simple jet dynamics, i.e. without including lateral expansion and hydrodynamic instabilities. In addition, also in the case of top-hat jets, fits to the GRB 170817A show that there is a large degeneracy in the parameters which can not be determined precisely from the observations (e.g., Gill et al., 2019).

A detailed study of the dynamics of structured jet can help us to better understand the dynamics and

radiation of GRB jets. In this work, we investigate the dynamics of seven models of structured jets along with their effects on the afterglow radiation through special relativistic hydrodynamic (SRHD) simulations, and compute a set of light curves which can be used to fit future GRBs seen off-axis.

This paper is organised as follows. In Section 4.3 we show the methodology and the initial conditions of the simulated structured jets. In section 4.4 we show the results, that is, the jet dynamics and the radiation produced by different jet models. The section 4.5 includes the discussion and the application to GRB 170817A. Finally, in section 4.6 we present our conclusions.

4.3 Methods

We run a set of two-dimensional (2D), special relativistic hydrodynamics simulations, by employing the adaptive mesh code *Mezcal* (De Colle et al., 2012a). The code employs a second order HLL Riemann solver. The equations are solved on an adaptive mesh refinement grid. The simulations were implemented in a spherical computational domain of radial and angular size $(r_{\rm max}, \theta_{\rm max}) = (2 \times 10^{19}$ cm, $\pi/2)$. The inner boundaries are located at 1.03×10^{17} cm. The basic grid contains $(100, 16)$ cells in the (r, θ) directions, and 14 levels of refinement, corresponding to a maximum resolution of $(\Delta r_{\rm min}, \Delta\theta_{\rm min}) = (2.44 \times 10^{13}$ cm, 1.20×10^{-5} rad). We initialize the simulations at $t_0 = 9.75 \times 10^6$ s corresponding to a Lorentz Factor $\Gamma_0 = 30$ on the jet-axis[1].

We assume that the flow is axisymmetric, with all quantities depending only on the polar angle θ (measured from the z-axis) and on the radial distance r defined from the origin of the coordinate system[2]. Although in the simulations we assume a constant density medium, for future reference we write all the equations of this section for the general case of a stratified medium, with a density $\rho = A_k r^{-k}$.

We studied the evolution of structured jets by assuming an initial energy $(E_j(\theta))$ and Lorentz factor $(\Gamma_j(\theta))$ profile, following the implementations presented by Granot 2005; Granot 2012; Granot et al. 2018; Gill & Granot 2018; Gill et al. 2019; Beniamini et al. 2020. We follow the dynamics both during the relativistic and the non-relativistic regimes. In a post-processing treatment, we calculate the afterglow light curves for 50 observation angles $\theta_{\rm obs}$. In addition, we fit observations of GRB 170817A with the simulated models (Granot, 2012; van Eerten & MacFadyen, 2012), to constrain the jet parameters.

[1] As described below, these initial conditions can be scaled to represent a more general set of simulations.

[2] Other effects, e.g., asymmetries along the polar direction or the presence of a dynamically important magnetic field, can be important, require three-dimensional simulations and are left for a future work.

4.3.1 Structured jet models

In our simulations, the initial angular profile of the jet/cocoon is characterised by its energy profile per solid angle

$$\mathcal{E}(\theta) = \frac{dE_j(\theta)}{d\Omega} = \frac{E_{\rm k,iso}(\theta)}{4\pi}\ , \tag{4.1}$$

where $E_{\rm k,iso}(\theta) = 4\pi\mathcal{E}(\theta)$ is the local value of the isotropic equivalent energy. The total energy of the jet is obtained by the integral over solid angle

$$E_{\rm j,tot} = \int_0^{\theta_{\rm max}} \mathcal{E}(\theta) d\Omega. \tag{4.2}$$

All simulations employ the same total energy.

Taking $\mathcal{E}_c$ and Γ_c as the values of energy and shock Lorentz factor in the jet core ($\theta \leq \theta_j$), energy and shock Lorentz factor are initialised as a function of the angular profile $f(\theta)$, as

$$\mathcal{E}(\theta) = \mathcal{E}_c\, f(\theta), \tag{4.3}$$

$$\Gamma_0(\theta) - 1 = (\Gamma_c - 1)\, f(\theta). \tag{4.4}$$

We consider the following angular functions $f(\theta)$:

- A "smooth power law jet (SPLJ)" with a uniform core (for $\theta \leq \theta_0$) and smoothly decreasing wings, defined by:

$$f(\theta) = \begin{cases} 1 & \theta \leq \theta_0 \\ (\theta/\theta_0)^{-2} & \theta > \theta_0 \end{cases}\ . \tag{4.5}$$

- A power law jet model (PLJ) (e.g., Kumar & Granot, 2003):

$$f(\theta) = \left(1 + \frac{\theta^2}{\theta_0^2}\right)^{-a/2}\ , \tag{4.6}$$

  where the parameter $\theta_0 = 0.1$ is the core angle and the exponent takes the values $a = 1, 2, 3$.

- An exponential Jet (EPJ), corresponding to

$$f(\theta) = f e^{-\frac{1}{2}(\theta/\theta_0)^{\alpha}}, \tag{4.7}$$

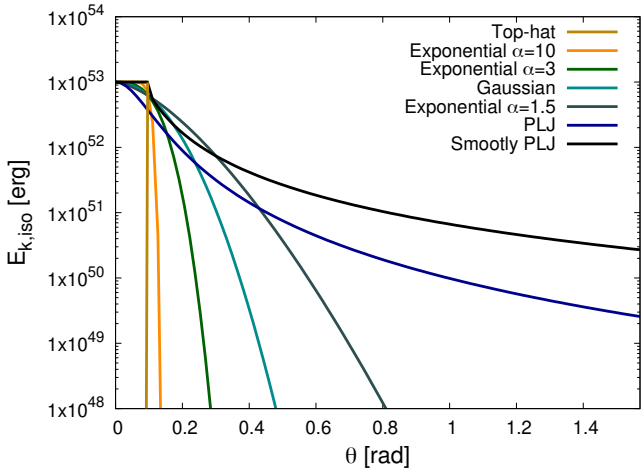

Figure 4.1: Angular dependence of $E_{\rm k,iso}(\theta)$ for seven energy profiles. Every jets started with the same total energy (10^{53} erg) on the jet-axis at $t = t_0$.

and $\theta_0 = 0.1$, with $\alpha = 1.5, 2, 3, 10$. The Gaussian profile (Granot, 2005; Kumar & Granot, 2003) corresponds to the case $\alpha = 2$.

- A "top-hat" wedge with

$$f(\theta) = \begin{cases} 1 & \theta \leq \theta_0 \\ 0 & \theta > \theta_0 \end{cases} , \tag{4.8}$$

with $\theta_0 = 0.1$.

Figure 4.1 shows the explicit angular dependence of $E(\theta)_{\rm k,iso}$ which depends on the angular profiles trough the equations 4.1 and 4.3. For each model, the initial Lorentz factor $\Gamma_0(\theta)$ have a similar dependence. More collimated jets preserve relativistic velocities at all polar angles while more extended jets/cocoon include lower (sub-relativistic) velocities in the initial conditions.

4.3.2 Numerical implementation

The evolution of a spherical blast wave with a certain energy $E_{\rm k,iso}(\theta)$ can be described by two phases: a coasting phase, in which the shock is moving with constant velocity; and a deceleration phase, in which the shock front velocity drops as a function of time as it accelerates more and more shocked material. Thus, the initial conditions can be determined once the energy profile $E_{\rm k,iso}(\theta)$, the shock Lorentz factor (during the coasting phase) $\Gamma_0(\theta)$, and the time t_0 when the simulation starts, are specified. The position of the shock front will be also a function of the polar angle, depending on the angular dependence of the shock front velocity.

The deceleration time $t_d(\theta)$ (i.e., the time when the shock stops moving with constant speed and starts decelerating) is given as

$$t_d(\theta) = \left[\frac{(17-4k)E_{\rm k,iso}(\theta)}{8\pi A_k c^{5-k} u_{\rm sh}^2(\theta)}\right]^{\frac{1}{3-k}}, \tag{4.9}$$

being $u_{\rm sh}(\theta, R) = \sqrt{\Gamma_{\rm sh}(\theta, R)^2 - 1}$ the initial shock velocity, corresponding to a Lorentz Factor $\Gamma_{\rm sh}(\theta, R)$. The fluid Lorentz factor (both during the coasting and deceleration phases) is given as (Panaitescu & Kumar, 2000; Beniamini et al., 2020)

$$\frac{\Gamma(\theta, R)}{\Gamma_0(\theta)+1} = \frac{\zeta^{k-3}}{2}\left[\sqrt{1 + \frac{4\Gamma_0(\theta)}{\Gamma_0(\theta)+1}\zeta^{k-3} + \left(\frac{2\zeta^{3-k}}{\Gamma_0(\theta)+1}\right)^2} - 1\right], \tag{4.10}$$

with $\zeta = R/R_d(\theta)$ and $R_d = ct_d(\theta)$.

The initial position of the shock front (at each angle) is then determined by integrating the equation

$$\frac{dR_{\rm sh}(t)}{dt} = v_{\rm sh}(t, R_{\rm sh})c\ , \tag{4.11}$$

where $v_{\rm sh} = \sqrt{1 - 1/\Gamma^2(\theta, R)}$ (see equation 4.10).

Once the position of the shock is determined, the values of density, pressure and velocity (in the post-shock region) are determined by using self-similar solutions. As the flow is not moving with relativistic velocities at all angles, we consider both the BM76 solution (for relativistic flows) and the Sedov solution (when at large angles the shock front is moving sub-relativistically).

The BM76 solution describes the deceleration of a relativistic explosion. The model considers the self-similar variable

$$\chi = 1 + 2(4-k)\cdot 2\Gamma_\tau^2\left(1 - \frac{r}{R_{\rm sh}}\right), \tag{4.12}$$

in order to calculate the post-shock variables

$$u_r = u_\tau \chi^{-1/2}, \tag{4.13}$$

$$\rho_r = \rho_\tau \chi^{-(10-3k)/(2-4k)}, \tag{4.14}$$

$$p_r = p_\tau \chi^{-(17-4k)/(3(4-k))}, \tag{4.15}$$

where u_τ, ρ_τ and p_τ are the velocity, density and pressure at $r = R_{\rm sh}$.

On the other hand, a sub-relativistic blast wave is described by the Sedov-Taylor self-similar solution. In this case the self-similar variable is

$$\chi = r/R_{\rm sh}, \tag{4.16}$$

and the physical variables are defined as

$$\rho_{\rm nr} = \rho_\tau \cdot f_\chi \frac{\chi^{(9-5k)/2}}{8} \exp\left[\frac{3}{8}\frac{(3-k)}{(2-k)}\left(g_\chi - 1\right)\right], \tag{4.17}$$

$$p_{\rm nr} = p_\tau \left(\frac{f_\chi}{8}\right)^{5/3} \exp\left[\frac{3\cdot(g_\chi-1)}{4(2-k)}\right], \tag{4.18}$$

$$u_{\rm nr} = u_\tau \cdot \frac{4\chi(1+g_\chi)}{f_\chi}. \tag{4.19}$$

where

$$g_\chi = \chi^{(8-4k)}, \tag{4.20}$$

$$f_\chi = 5 + 3g_\chi, \tag{4.21}$$

We define the post-shock variables by employing the following relations:

$$u_{\rm ps} = \frac{u_{\rm nr}}{\Gamma_\tau^7} + \frac{u_r(\Gamma_\tau^4 - 1)}{\Gamma_\tau^4}, \tag{4.22}$$

$$\rho_{\rm ps} = \frac{\rho_{\rm nr}}{\Gamma_\tau^7} + \frac{\rho_{\rm nr}(\Gamma_\tau^4 - 1)}{\Gamma_\tau^4}, \tag{4.23}$$

$$p_{\rm ps} = \frac{p_{\rm nr}}{\Gamma_\tau^7} + \frac{p_{\rm nr}(\Gamma_\tau^4 - 1)}{\Gamma_\tau^4}, \tag{4.24}$$

which converge to the BM76 solution when $\Gamma_\tau \gg 1$, to the Sedov-Taylor solutions when $\Gamma_\tau \gtrsim 1$. In all the runs, we take the same external density. It is assumed here that the external density is uniform, $\rho_0 = n_0 m_p = A_0 = 1.67 \times 10^{-24}$ g cm^{-3} with $n_0 = 1$ cm^{-3}.

4.3.3 Calculation of the light curves

The physical model which explains the radiation emitted from a relativistic source is described by Granot & Ramirez-Ruiz (2010) for syncrotron emission. The procedure required to calculate the radiation emitted from a relativistic blast wave from SRHD simulations is detailed by De Colle et al. 2012a. The method was development for the post-processing data obtained by numerical simulations. The outputs obtained

by our numerical simulations contain information on the physical variables (position, time, velocity, density, pressure) in each cell of the spatial domain. Each cell then contributes to the total emission. For the synchrotron emission we assume that the electrons behind the shock follow a distribution $N(\gamma_e) \propto \gamma_e^{-p}$. These electrons are accelerated behind the shock acquiring a fraction $\epsilon_e = 0.1$ of the thermal energy available, and with a magnetic field energy density given as well as a fraction of the thermal energy, i.e. $\epsilon_B = B^2/(8\pi e) = 0.01$. The spectral distribution is estimated following the method of (Granot & Sari, 2002).

4.4 Results

4.4.1 Structured jet dynamics

Figure 4.2 shows density maps for three representative simulations. In the figure, each row shows simulations of structured jets with power-law (PLJ, left panels), Gaussian (middle panels) , and exponential (with $\alpha = 10$, i.e. nearly top-hat) profiles (right panels). The rows represent three evolutionary stages, namely the initial conditions (top panels), the time when the evolution of jets present major differences between them, and the final time when all models become spherical (bottom panels).

The PLJ jet starts with a large amount of material at large polar angles, simulating the presence of an extended cocoon. In the Gaussian jet (middle panels), the wings energy and velocities quickly decrease to low values. The exponential $\alpha = 10$ jet has a structure similar to the one of a top-hat jet, with a cutoff in jet opening angle at θ_0. Every case has similar minimal and maximum values of density and starts at the same radial position on the jet-axis.

At intermediate times ($t = 5.4\times10^3$ days), the PLJ jet presents a low density cavity along the jet axis smaller than the other jets. Its lateral expansion remains pronounced. Near to the jet core, it shows a diffuse region which could present instabilities and mixing, not large enough to capture it. The hydrodynamic instabilities are evident in more collimated jets, in which Kelvin-Helmholtz instabilities develop close to the jet edge.

At the final stage the jets are nearly spherical. The final shape is still oblate, with material close to the vertical axis preserving a slightly larger energy and velocity with respect to material expanding close to the equatorial plane.

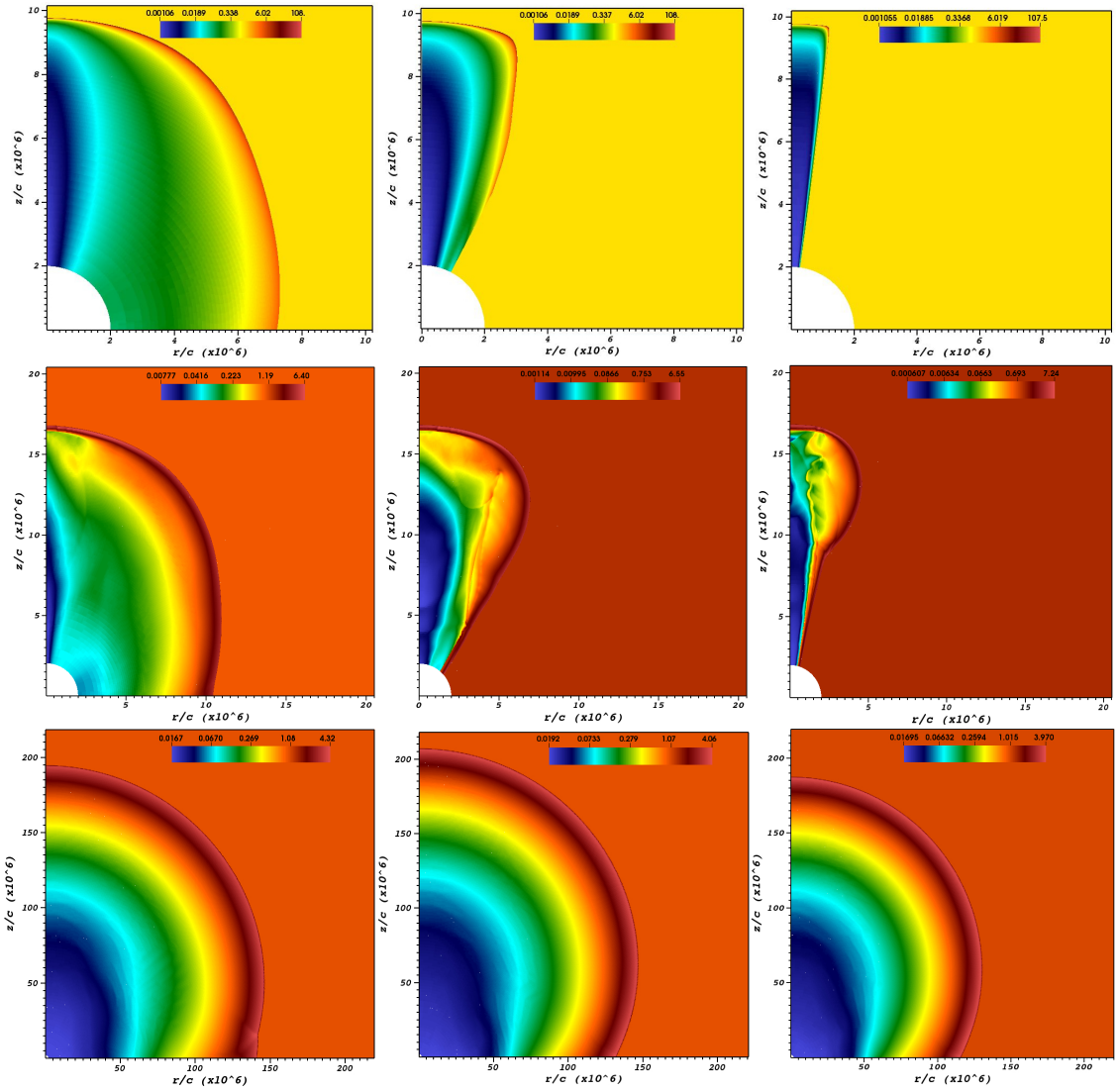

Figure 4.2: Density maps at different evolutionary times (in the lab frame). We show three representative models from less collimated to more collimated jets (PLJ, Gaussian, Exponential $\alpha = 10$, from left to right). In the top panels (first row) we show the initial conditions at t_0. The second row shows snapshots taken at 10% of the total simulation time ($t = 5.4 \times 10^3$ days). The third row (bottom panels) corresponds to the final time of the simulations ($t > 6.3 \times 10^4$ days), in which the jets are nearly spherical.

4.4.2 Evolution of jet structure and opening angle

Figure 4.3 shows the time evolution of the energy for the top-hat, Gaussian and PLJ jet models. As $d\Omega = 2\pi \sin\theta d\theta$, the initial energy distribution is given as $E(\theta) = E_{\rm k,iso} \int_0^{\theta_0} f(\theta)\cos(\theta)d\theta$, being $f(\theta)$ the function that describes the angular energy profile.

Significant changes appear at the very beginning of the simulation. At 200 days (100 days after the beginning of the simulation), the energy distributions evolve spreading laterally. We can see that as a function of time the curves resemble more and more a semi-hyperbolic form. However, they do not converge to a spherical form even at the very end of the simulation. For instance, the latest two times (shown by the red and black lines respectively) still evolve substantially.

This figure clearly illustrates that initial conditions are not preserved with time. The spreading of GRB jets as a function of time has been extensively studied in the literature, and is supposed to happen when the jet Lorentz factor is $\Gamma_j \lesssim 1/\theta_j$. These calculations show that regions with lower energies, located at high latitudes, spread laterally much before the jet break time (usually estimated by considering the Lorentz factor along the jet core). Lateral expansion in structured jets is not usually computed in analytical models. Our results show that the full evolution of the system must be considered when computing off-axis jet emission.

Figure 4.4 shows the jet opening angle vs. time, being the jet onpeing angle as the region that contains the 75% of the total jet energy of the jet. The lateral expansion begins approximately at the same time (when $\Gamma \sim 1/\theta_0$). Not even after tens of years the jets has become completely spherical. More structured jets (SPLJ and PLJ) starts with large opening. Then, their opening angle increments by a small amount, while more collimated jets present a faster increment (at about the same rate) after $\Gamma \sim 1/\theta_0$. The slope of the curve changes at $\sim 10^4$ days, increasing slowly until nearly converging to $\pi/2$. The figure also show that exponential jets (eq. 4.7).

4.4.3 Afterglow emission of structured jets

The upper panel of Figure 4.5 shows radio light curves (at 3 GHz) for an observer located on-axis. The source is at a distance of 40 Mpc. The slopes of the light curve show a characteristic power-law behaviour. More collimated jets present a lower flux at all time. At $\sim$ 10 days, the jet break produces a change in the slope of the light curve (similar for all models). In the bottom panels of Figure 4.5 (showing light curves for *off-axis*

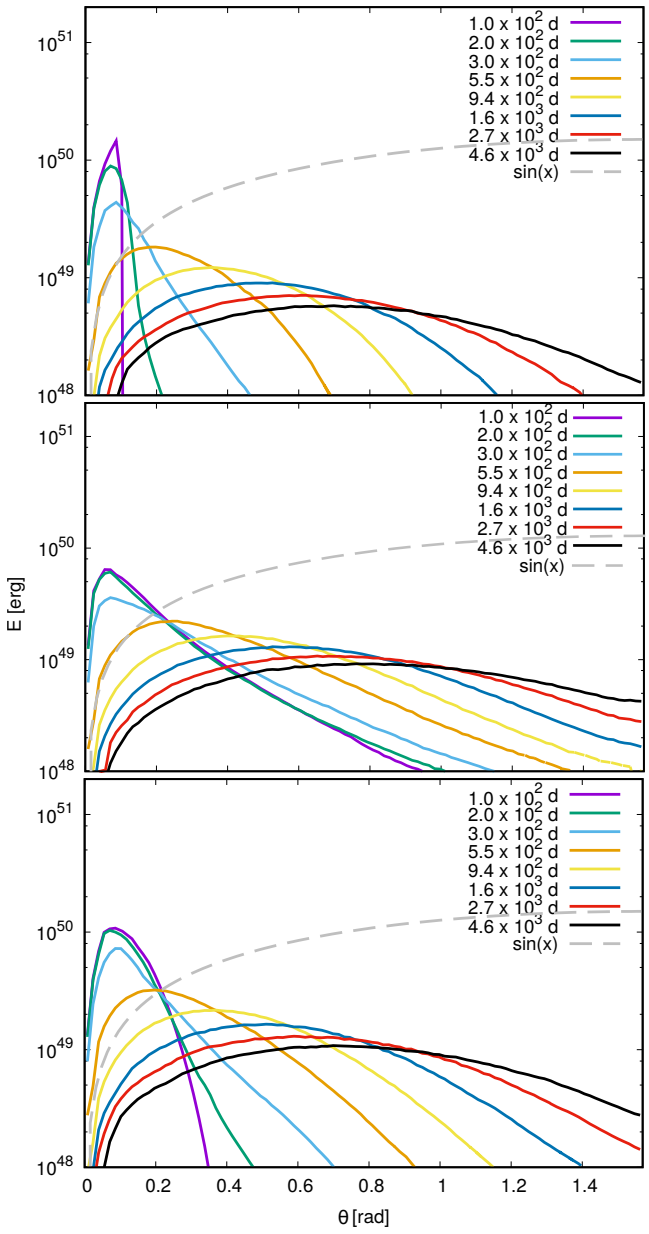

Figure 4.3: Time evolution of the angular distribution of energy. The upper panel shows the evolution of a top-hat jet, the middle panel the evolution of a Gaussian jet and the bottom panel shows the evolution of the PLJ jet. Different colors correspond to different evolutionary times.

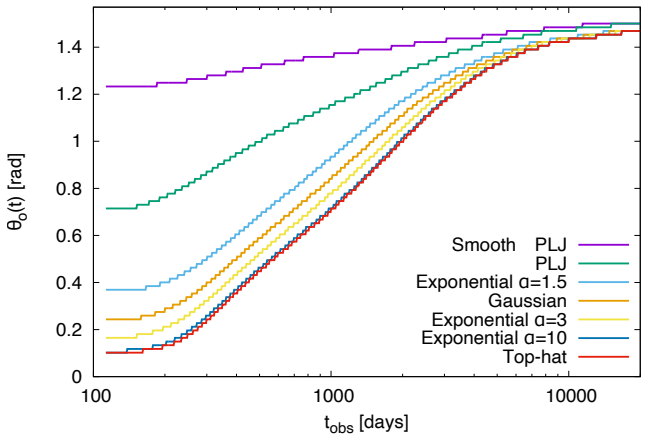

Figure 4.4: Evolution of the jet opening angle (defined as the angle including the 75% of the total jet energy, i.e. $E(\theta < \theta_j) = 0.75E_{\rm total}$) for each jet model. Lateral expansion (computed in terms of total energy) starts after the jet break, i.e. when $\theta_0 < 1/\Gamma_j$, being θ_0, Γ_j the initial opening angle and Lorentz factor of the jet.

observers) the differences among different models are more noticeable. For $\theta_{\rm obs} = 15°$, i.e close to the jet core, the light curves for structured jets have a similar behaviour while more collimated jets have a lower flux at early time (as they are completely outside the line of view of observers) before showing a fast increase. For angles $\theta_{\rm obs} \geq 30°$ the initial rise in flux begins at different times (corresponding to the time when the edge of the jet of each model becomes visible to the observer). The SPLJ model has a behaviour similar to that of a spherical jet.

4.5 Discussion

We investigated the dynamics of seven structured jet models and their implications on the afterglow radiation. In the following, we will discuss the results obtained in the previous section. Furthermore, we will fit our models to observations of GRB170817A, showing that there is a large degeneracy in the determination of the jet parameters.

At the beginning of the simulations (upper panel in Figure 4.2) a part of the jet material extends outside the jet core, i.e. at $\theta \geq \theta_j$. Our implementation of structured jets can be interpreted as a parametrization of the cocoon. The jet cocoon acquires its structure after the jet breaks from the dense environment at scales of $r \sim 10^{10} - 10^{11}$ cm. Then, considering different structures for the jet corresponds effectively to considering different structures for the cocoon at much smaller scales. The early evolution of the jet (middle panel of Figure 4.2) suggest that the angular distribution of energy and velocity contributes to a rapid lateral

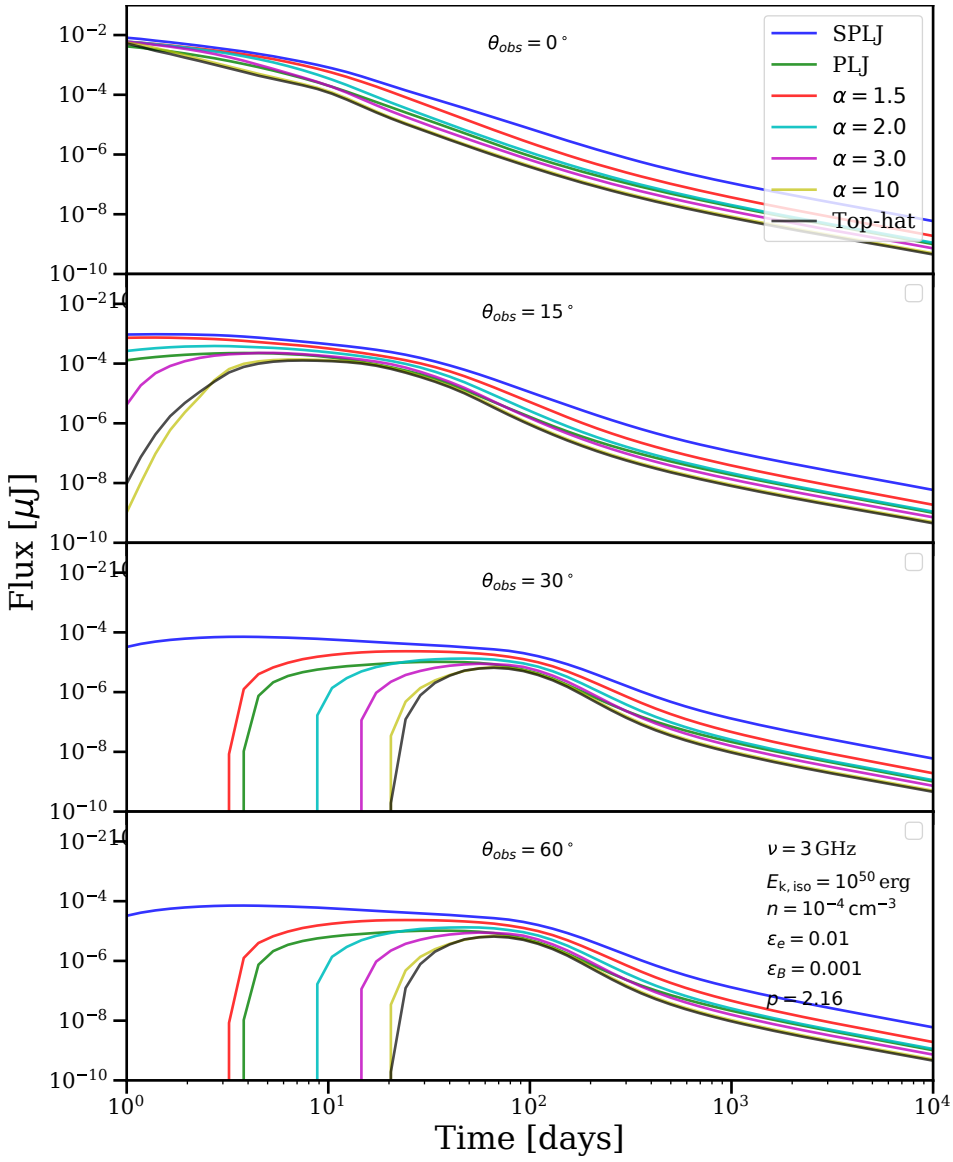

Figure 4.5: Radio light curves produced by structured jets at different observer angles.

expansion. This effect is more pronounced for more structured jets as more material is swept up by their extended wings. In addition, more collimated jets contain abrupt velocity gradients at early times which produce Kelvin-Helmholtz instabilities. Even after decades of evolution, jets do not acquire a completely spherical shape. In the final snapshot of the simulations presented in this paper, the jet core still remains more energetic and faster than the jet lateral region, allowing the core to reach larger distances than the equatorial region. According to the behaviour of the jet opening angle (Figure 4.4) the jets starts approaching a spherical shape at $t \gg 10^3$ days.

Additionally, we found that the angular distribution of energy of the jet changes its structure over time (section 4.4.2). This result means that the jet does not preserve its initial structure and does not evolve as a slice of a spherical shock during the simulations. Therefore, analytical calculations of structured GRB jets, which usually assume that each angular slice $(\theta, \theta + d\theta)$ expands as it was a spherical shock front (i.e. neglecting transfer of information along the polar directions) directions) do not properly capture the evolution of the jet's structure, and numerical simulations are necessary to properly describe the GRB dynamics.

To probe the jet structure, we fit observations of GRB 170817A (e.g., Lazzati et al., 2018; Nathanail et al., 2020; Beniamini et al., 2020; Makhathini et al., 2020). The optical, radio and X-ray data are taken from Makhathini et al. 2020. We rescaled all data to 3 GHz by using the relation $(\nu/\nu')^{(1-p)/2}$, with $p = 2.14$ (e.g., Makhathini et al., 2020). Then, the jet scaling relations allow us to determine the jet energy and density of the environment, once the microphysical parameters ϵ_e and ϵ_B are given.

Scaling relations developed by Granot 2012; van Eerten & MacFadyen 2012 allow us to adjust the jet parameters. Energy and density scale as

$$E' = kE, \tag{4.25}$$

$$n' = \lambda n. \tag{4.26}$$

Then, the observer time and the flux can be obtained as

$$\frac{t'}{t} = \left(\frac{k}{\lambda}\right)^{1/3}, \tag{4.27}$$

$$\frac{F'}{F} = k\lambda^{(1+p)/4} \left(\frac{\epsilon'_e}{\epsilon_e}\right)^{p-1} \left(\frac{\epsilon'_B}{\epsilon_B}\right)^{(1-p)/4}. \tag{4.28}$$

For each structured jet model, we compute $\sim$ 50 light curves corresponding to different observer angles

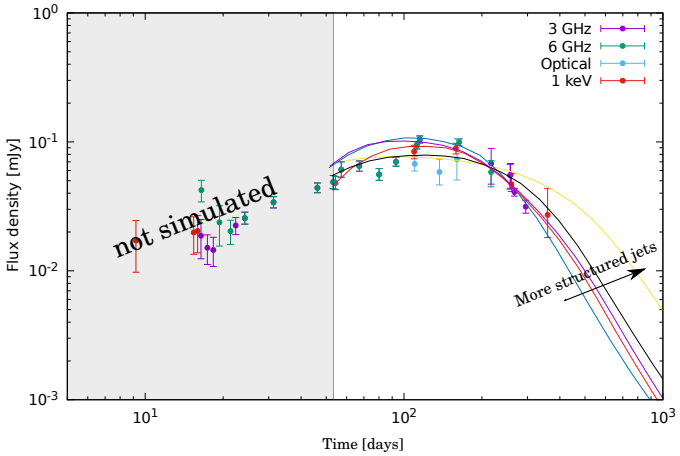

Figure 4.6: Fit of GRB 170817A by employing structured jet models at late times and Bootstrapping method. The data are scaled at 3 GHz. The fit for each model is obtained by assuming a different set of parameters showed in Table 4.1. The best fit corresponds to the Gaussian model, but the other models can not be discarded (black line).

$\theta_{\rm obs} \in [0°, 90°]$. We employ a Montecarlo optimisation method to explore different set of parameters k, λ. The micro-physics parameters have been fixed as $\epsilon_e = \epsilon_B = 0.1$. By comparing the predicted models with the observations, we determine the values of k and λ. Then, the relations above provide the values of energy and density given the values used in the numerical simulations.

Figure 4.6 shows the best choice parameters k, λ from the fitting process. We can not include the fit at times shorter than the beginning of the simulation ($t < t_0$) as the propagation of the jet at those times is not included in the simulations. The "arrival time of the first photon" for each simulation is shown in Table 4.1 and is broadly indicated by the grey region in the figure. Our models fit reasonably well the late observations. Each structured jet model fits the data with a particular choice of $\theta_{\rm obs}, E_{\rm k,iso}, n$ (see Table 4.1). This fitting procedure shows that any jet structure fits nearly equally well the data, and is not excluded. In addition, we notice that these results have been obtained by considering fixed values of ϵ_e and ϵ_B, which are in principle unknown. Including these parameters in the fitting process leads to degeneracy of the parameters. Thus, we conclude that the structure of the jet associated to GRB 170817A is still undetermined.

Figure 4.7 shows the possible densities and energies corresponding to different values of the micro-physical parameters ϵ_e and ϵ_B. In this Figure 4.7, the blue circles correspond to the values of ϵ_e, ϵ_B ($\epsilon_e \sim 0.1, \epsilon_B \sim 10^{-5} - 0.1$) determined by (see, Santana et al., 2014). By using these values, the density and energies are limited to $n_0 = 10^{-3} - 10^{-5}$ cm^{-3}, $E = 10^{51} - 10^{53}$ ergs.

Model	$\theta_{\rm obs}$ (°)	$E_{\rm k,iso}$ (erg)	n (cm^{-3})	Arrival (d)
SPLJ	38.8	4.1×10^{53}	6.2×10^{-5}	20.44
Exp $\alpha = 1.5$	29.1	6.4×10^{52}	5.7×10^{-4}	14.60
Gaussian	27.2	5.4×10^{52}	1.1×10^{-3}	20.44
Exp $\alpha = 3$	26.9	5.5×10^{52}	2.0×10^{-3}	28.60
Exp $\alpha = 10$	18.5	8.4×10^{52}	2.0×10^{-3}	40.03
Top-hat	16.7	1.0×10^{53}	1.1×10^{-4}	47.36

Table 4.1: Best parameters for GRB 170817A for every simulated structured jet model. The viewing angle ($\theta_{\rm obs}$) decreases for more collimated jets. The time of the first photon arriving to the observer changes for each structured jet.

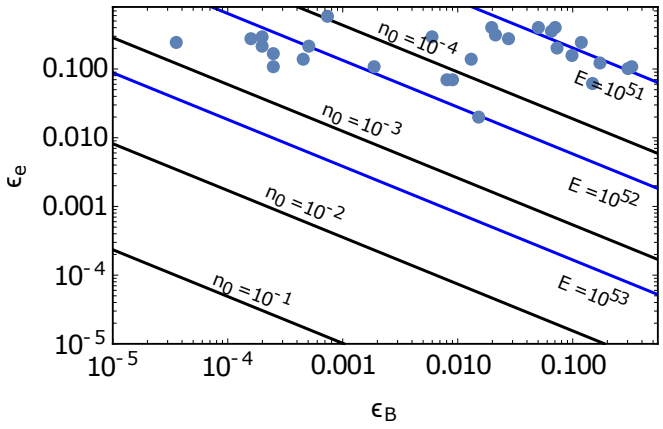

Figure 4.7: The space of micro-physical parameters obtained by employing the Gaussian model. The black and blue lines show the possible values of density and energy. The blue circles correspond to the values of ϵ_e and ϵ_B inferred by Santana et al. 2014

.

4.6 Conclusions

In the following, we list our main results.

- Structured jets expands laterally from early times. Thus, it is incorrect to neglect the lateral expansion
- The light curves can be distinguished for observers $\theta_{\rm obs} > 15^\circ$ at early times ($t < 200$ days). The final shape is similar for all jet models ($t > 200$ days).
- The structure of GRB170817A is still undetermined due to the degeneracy between the parameters. The degeneracy should be broke by the combination of the radiation produced at times $t < t_0$ before of the initial time of the large-scale simulations with the radiation $t > t_0$ presented in this work.
- Our results can be used to fit future observations of off-axis GRBs.

Chapter 5

Gravitational Waves from the Propagation of Long Gamma-Ray Burst jets

Este capítulo tiene como contenido el artículo enviado a Monthly Notices of the Royal Astronomical Society como: **Urrutia, G.**, De Colle, F., Moreno, C., Zanolin, M. "Gravitational Waves from Long Gamma-Ray Bursts and Supernovae", MNRAS, Submitted, July 2022. El árbitro ha mandado sus comentarios con cambios menores recomendando la publicación en la revista. La respuesta al árbitro está siendo elaborada.

In this chapter, I present the gravitational wave signal produced by long gamma-ray burst jets. Despite the amplitude of the signals founded in this work are lower than the signal produced by a compact merger, this should be detected by future space-based interferometers.

Since gamma-ray bursts are produced by relativistic jets, we can determine the radiation emitted directly from jet evolution (e.g., Granot & Sari, 2002; Zhang & MacFadyen, 2009; De Colle et al., 2012a). The electromagnetic counterparts can be estimated 10^3 s after the jet launching from the central engine (e.g., Piran, 1999). However, the first seconds of jet propagation take place in a high opacity environment (Mészáros & Gehrels, 2012; Kumar & Zhang, 2015). Therefore, the radiation cannot be detected at this early stage and the early properties of the jet and of the central engine can not be directly inferred by observations. The first observations of compact merger in September 2015 made of LIGO/VIRGO represented the birth of gravitational wave astronomy (Abbott et al., 2016). The first observations of LIGO/Virgo reveals high-frequency signals from compact mergers. However, these mergers are not the only events which produce gravitational waves (e.g., Abbott et al., 2017b). In this chapter we discuss how the propagation of relativistic

jets can also produce gravitational waves (Segalis & Ori, 2001; Akiba et al., 2013; Siegel et al., 2014; Leiderschneider & Piran, 2021a). The aim of this work is to present the first numerical study of gravitational waves produced by relativistic jets and on how they can provide information on the early dynamics of jets.

We run numerical simulations of 5 models of relativistic jets moving through the progenitor of LGRBs. By post-processing the results of the numerical simulations, we computed the GW signal. We found that the key parameters which determines the jet dynamics, such as luminosity, jet duration, velocity, and size of the progenitor, are all strongly related to the amplitude and shape of the signal. In addition, we show that the GW signal is formed by two characteristic peaks associated to the jet duration and to the end of the aceleration phase. The amplitude of GW signal could be detected for extragalactic sources by future space-based interferometers.

5.1 Abstract

Gamma-ray bursts (GRBs) are produced during the propagation of ultra-relativistic jets. It is challenging to study the jet close to the central source, due to the high opacity of the medium. In this paper, we present numerical simulations of relativistic jets propagating through a massive, stripped envelope star associated to long GRBs, breaking out of the star and accelerating into the circumstellar medium. We compute the gravitational wave (GW) signal resulting from the propagation of the jet through the star and the circumstellar medium. We show that key parameters of the jet propagation can be directly determined by the GW signal. The signal presents a first peak corresponding to the jet duration and a second peak which corresponds to the break-out time for an observer located close to the jet axis (which in turn depends on the stellar size), or to much larger times (corresponding to the end of the acceleration phase) for off-axis observers. We also show that the slope of the GW signal before and around the first peak tracks the jet luminosity history and the structure of the progenitor star. The amplitude of the GW signal is $h_+ D \sim$ hundreds to several thousands cm. Although this signal, for extragalactic sources, is outside the range of detectability of current GW detectors, it can be detected by future instruments as BBO, DECIGO and ALIA. Our results illustrate that future detections of GW associated to GRB jets will represent a revolution in our understanding of this phenomenon.

5.2 Introduction

Gamma-ray bursts (GRBs) are extremely luminous pulses of gamma-rays (with an isotropic energy of 10^{51} – 10^{54} ergs) lasting typically from $\sim$ a fraction of a second to $\sim$ hundreds of seconds. GRBs are classified based on their duration. Short GRB (SGRBs), lasting $\lesssim 2$ s, are typically produced during the coalescence of neutron stars (NS), while long GRBs (LGRBs), lasting $\gtrsim 2$ s, are in several cases associated to the collapse of massive stars and their explosion as type Ic supernovae (SNe) (for a review, see, e.g., Kumar & Zhang 2015). Recent observations of a kilonova associated to GRB211211a showed that the usual identification of different progenitors mainly based on the GRB duration can be misleading (Gao et al., 2022b; Troja et al., 2022).

The gamma-ray emission observed in these events is produced by highly relativistic jet, moving with Lorentz factors $\Gamma_j \sim 100$ - 1000. These jets are ejected from a black hole or a magnetar (the so-called "central-engine") formed during the collapse of a massive star (see, e.g. Hjorth & Bloom 2012; Cano et al. 2017) or as a result of the coalescence of a binary NS system (see, e.g., Berger 2014).

Once the jet is ejected from the central engine, it propagates through the dense, optically thick surrounding

medium formed by the progenitor star or the debris of the binary NS system, before breaking out at distances of $\sim 10^{10} - 10^{11}$ cm. Theoretical studies show that, during this phase, the jet moves with sub-relativistic velocities (~ 0.1 - $0.5\ c$), being c the light speed (e.g., Bromberg et al., 2011b; Nakar & Piran, 2016; De Colle et al., 2018b). When the jet breaks out from the dense environment, it accelerates to large jet Lorentz factors Γ_j ($\sim E_j/M_j c^2$ where E_j and M_j are the jet energy and mass), before emitting the observed gamma radiation at larger distances from the central engine ($\gtrsim 10^{13} - 10^{15}$ cm), once the hot plasma becomes optically thin to gamma-ray radiation.

The prompt gamma-ray emission is followed by a multi-wavelength afterglow emission covering the full electromagnetic spectrum, from radio to X-rays, and lasting from minutes to several years. Thus, the late phases of evolution of the relativistic jets (from $\sim 10^{13}$ cm to $\gtrsim 10^{18}$ cm) can be studied by analyzing these rich electromagnetic signatures (see, e.g., Kumar & Zhang 2015 and references therein). On the other hand, it is much more difficult to study the early phases of evolution of the jet, corresponding to distances $\lesssim 10^{10} - 10^{11}$ cm, as the high densities make the jet plasma optically thick to electromagnetic radiation. In particular, only neutrinos (e.g., Kimura 2022) and GWs could probe directly the behaviour of the jet while it is crossing the dense environment.

In addition to oscillating GWs signals associated to the coalescence of compact objects (Abbott et al., 2017b), the possibility of detecting non-oscillating, low frequency signals (the so-called "memory" signal produced by unbound material over timescales $\gtrsim 1$ s), has been proposed long time ago (Braginskii & Thorne, 1987). These "memory" signals have been studied extensively, e.g., in the context of supernovae (SNe) explosions (e.g. Kotake et al., 2006; Murphy et al., 2009; Müller et al., 2012; Müller et al., 2013; Wongwathanarat, A. et al., 2015; Yakunin et al., 2015; Powell & Müller, 2019; Hübner et al., 2020; Mezzacappa et al., 2020; Richardson et al., 2022).

The focus of these studies was to discuss under which circumstances (in terms of specific instrument and signal morphology) the memory component of the signal spectral density is above the interferometric noise spectral density (see, e.g., Moore et al., 2015). This is a semiquantitative measure of the detectability of the memory (in the sense that it is an important metric but it is not related to a specific alghorithm). It is also worth stressing that for detectability the whole spectrum of the memory development over time matters, not just the zero frequency component produced by the asymptotic value.

Previous studies of the GWs produced by GRB jets have focused on the propagation of the jet through the dense envelope, or to the acceleration of the jet after the break-out (Segalis & Ori, 2001; Sago et al., 2004; Sun

et al., 2012; Akiba et al., 2013; Birnholtz & Piran, 2013; Du et al., 2018; Yu, 2020; Leiderschneider & Piran, 2021b). These studies have shown that the amplitude of the GW increases with time due to the continuous injection of energy into the jet from the central engine, or due to the jet acceleration once it expands through the environment.

Previous studies (Segalis & Ori, 2001; Sago et al., 2004; Sun et al., 2012; Akiba et al., 2013; Birnholtz & Piran, 2013; Du et al., 2018; Yu, 2020; Leiderschneider & Piran, 2021b) estimating the GW memory from GRB jets were based on simple analytical and/or semi-analytical estimations. Although these calculations provide a qualitative understanding of the GW memory, quantitative estimations can be obtained only by detailed numerical calculations.

In this work, we study the propagation of relativistic jets associated to LGRBs through the progenitor star, and its propagation through the wind of the progenitor star up to large distances (10^{13} cm). We compute the resulting GW signal as a function of time and observer angle (with respect to the main axis of the jet). We also consider the possible presence of a supernova component, and how its GW signal is affected by the presence of the jet. As we will discuss below, although the simulations presented refer to the LGRB case (in which the jet is propagating through a massive progenitor star), the expected GW signal will be qualitatively similar in short GRBs.

The paper is structured as follows: in Section 5.3 we discuss the initial conditions of the hydrodynamic simulations, and the methods used to compute the GW directly from the simulations. Section 5.4 presents the results of the calculations, in particular, the jet dynamics as the jets propagate through the progenitor and its environment, and the calculation of the resulting GW. In section 5.5 we discuss our results, in the context of present and future GW detectors. Our conclusions are presented in section 5.6.

5.3 Methods

5.3.1 Numerical simulations

We study the first 300 s of evolution of relativistic gamma-ray bursts jets, associated with massive stellar collapse, by running a series of numerical simulations. The simulations employ the adaptive mesh refinement code *Mezcal* (De Colle et al., 2012a), which integrates the special relativistic, hydrodynamics equations by using a second-order (both in space and time), shock-capturing scheme.

We consider five scenarios (summarised in Table 5.1): an asymmetric supernova (the "supernova" model),

Scenario	$t_{\rm inj}$ (s)	Energy (erg)	Progenitor
Successful Jet 1	10	10^{51}	12TH
Successful Jet 2	2.5	10^{52}	16TH
Failed Jet	10	10^{51}	12TH
Supernova	1	10^{52}	12TH
Jet + Supernova	10	10^{51}	12TH

Table 5.1: Numerical simulations presented in this paper. The columns refer to: the scenarios considered, the time during which the jet/SN is injected into the computational box, its energy, and the progenitor star (see the main text for a detailed description of each model). The progenitors 12TH and 16TH correspond to 12 $M_\odot$ and 16 $M_\odot$ initial masses, respectively.

two successful jets without a SN associated (the "successful jet 1" and "successful jet 2" models), differing by their duration and total energy, a successful jet associated to a SN (the "jet + supernova" model), and a failed jet not associated to a SN (the "failed jet" model).

The numerical simulations (see Table 5.1) employ two dimensional (2D), cylindrical (axisymmetric) coordinates. In all the models, the computational box extends from $(r, z) = 0$ cm to $(r_{\rm max}, z_{\rm max}) = 10^{13}$ cm, and is resolved by employing 40×40 cells at the coarsest level of refinement and 17 levels of refinement, corresponding to a maximum resolution of $\Delta r_{\rm min} = \Delta z_{\rm min} = 3.8 \times 10^6$ cm. We set the density in the computational box by considering the pre-collapse stellar models 12TH and 16TH taken from Woosley & Heger (2006). These models[1] corresponds to stripped-envelope progenitor stars with stellar masses $M_\star = 9.23\ M_\odot$ and $11.45\ M_\odot$ and stellar radii $R_\star = 4.5 \times 10^{10}$ cm and 9×10^{10} cm for the 12TH and the 16TH models respectively. For radial distances $r > R_\star$, we consider a medium shaped by the wind of the Wolf-Rayet progenitor, i.e. with a density

$$\rho(r) = \frac{\dot{M}_w}{4\pi r^2 v_w}, \tag{5.1}$$

being $\dot{M}_w = 10^{-5}$ $M_\odot$ yr^{-1} and $v_{\rm w} = 10^3$ km s^{-1} typical values for the mass-loss rate and the velocity of the wind from a Wolf-Rayet star (e.g., Vink, 2011). The pressure in both the star and the wind is negligible (as in strong shock it does not affect the shock dynamics) and it is set as $p = 10^{-5}\rho c^2$.

In all except the "supernova" model, the relativistic jet is injected from an inner boundary located at $r_{\rm in} = 5 \times 10^8$ cm, with a jet Lorentz factor Γ_j =10. The jet energy is largely dominated by thermal energy, with the jet pressure given as,

$$p_j = \frac{\rho_j c^2}{4}\left(\frac{\Gamma_\infty}{\Gamma_j} - 1\right), \tag{5.2}$$

[1]Long GRBs are associated to broad-line, type Ic SNe, which are produced during the collapse of massive, compact Wolf-Rayet stars.

being ρ_j the jet mass density and $\Gamma_\infty = 100$ the asymptotic jet velocity, eventually achieved once the jet breaks out of the star and accelerates by converting its thermal to kinetic energy. In two of the simulations (differing by the presence of a SN and indicated in Table 5.1 as "successful jet 1" and "jet + supernova"), we inject the jet during $t_j = 10$ s, such that its total energy is $E_j = 10^{51}$ erg and its luminosity is $L_j = 10^{50}$ erg s^{-1}, while in one model (the "successful jet 2" model) we inject the jet during $t_j = 2.5$ s with a total energy of $E_j = 10^{52}$ erg, corresponding to a much larger luminosity $L_j = 4 \times 10^{51}$ erg s^{-1}. In all these cases the jet opening angle is $\theta_j = 0.1$ rad and, as we will discuss in detail below, the jet successfully breaks out of the star and accelerates to highly relativistic speeds through the progenitor wind. We also consider a simulation in which the jet also lasts for $t_j = 10$ s, with a total energy $E_j = 10^{51}$ erg, but with a larger jet opening angle $\theta_j = 0.2$ rad (the "failed jet" model). In this case, the jet will not be able to break out successfully from the star. We refer to this case as the choked or failed GRB case.

To study how the GW memory signal is affected by the presence of both a SN and a GRB, we also inject, in two of the five simulations ("supernova" and "jet + supernova" models, see table 5.1), a supernova shock front from the same inner boundary at $t = 0$ s. Following De Colle et al. (2021) and Urrutia et al. (2022a), we inject, from $r_{\rm in}$, a SN shock front during $t_{\rm sn} = 0.1$ s, with a total energy of $E_{\rm sn} = 4 \times 10^{51}$ erg and a mass $M_{\rm sn} = 0.1 M_\odot$. We assume that 10% of the SN energy is thermal, while 90% is kinetic. Type Ic, broad-line SNe associated to long GRBs present a certain degree of asymmetry (as inferred from polarization measurements, see, e.g., Maund et al. 2007; Tanaka et al. 2017, or by the analysis of line emission during the nebular phase, see, e.g., Taubenberger et al. 2009). To qualitatively reproduce this asymmetry, we set an angular dependence for the energy injected in the SN as $E_{\rm SN}(\theta) \propto \cos^2\theta$, being θ the polar angle measured with respect to the z-axis.

In the "jet + supernova" model, in which both SN and jet are present, the jet is injected with a delay of 1 s with respect to the SN. The origin of the SN associated to GRBs is debated. The models proposed include a wind from a collapsar disk (MacFadyen & Woosley, 1999b), energy ejection from a magnetar (e.g., Metzger et al., 2015), or the jittering jet mechanism (e.g., Papish & Soker, 2014); see also the discussion by De Colle et al. (2021). Thus, the time delay between the SN and the jet is uncertain.

5.3.2 Gravitational wave signals

We consider a system of reference centered on the central engine, being the z axis the main axis of propagation of the jet (see Figure 5.1). The direction of the observer is defined by the unit vector $\hat{n} = (\sin\theta_{\rm obs}, 0, \cos\theta_{\rm obs})$,

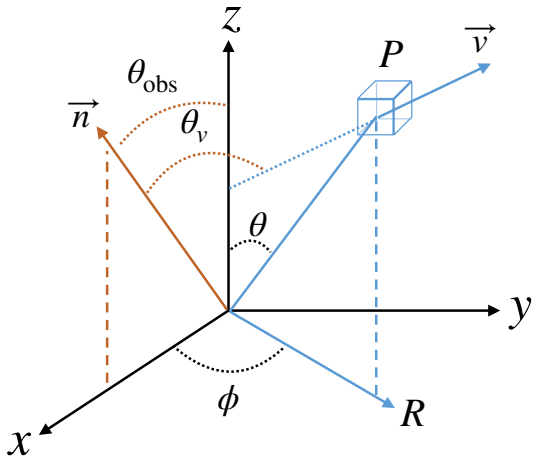

Figure 5.1: Schematic representation of the geometry of the problem. A fluid element P, located at angles ϕ, θ with respect to the x- and z-axis respectively, is moving with a velocity $\vec{v}$. The observer is located along the direction $\hat{n}$, in the plane xz and forming an angle $\theta_{\rm obs}$ with respect to the z-axis. The directions of the observer $\hat{n}$ and of the velocity vector $\vec{v}$ are separated by an angle θ_v, i.e. $\cos\theta_v = \hat{n}\cdot\hat{v}$. The simulations presented in this paper are computed in two-dimensional, axisymmetric cylindrical coordinates (the Rz plane shown in the figure), so that the three dimensional structure is reconstructed by rotating along the ϕ direction the snapshots of the numerical simulations.

where $\theta_{\rm obs}$ is the angle between the direction of the observer and the z-axis. We rotate the x and y axis such that $\hat{n}$ is located in the x, z plane. Thus, the axes $\hat{n}$, y and x' (rotated by an angle $\theta_{\rm obs}$ with respect to x) define a system of reference in the observer frame. We consider a fluid element P, at the position $\hat{r} = (\sin\theta\cos\phi, \sin\theta\sin\phi, \cos\theta)$, moving with a velocity $\vec{v} = (v_R\cos\phi, v_R\sin\phi, v_z)$, where v_R, v_z are the fluid velocities along the radial and vertical axis of the cylindrical system of reference (see Figure 5.1). While in previous studies the velocity of the fluid element has been fixed as vertical of radial, in this paper we leave it completely general, and determined directly from the numerical simulations.

Braginskii & Thorne 1987; Segalis & Ori 2001 obtained explicit expressions for the GW memory polarization components h_+ and $h_\times$ in the transverse-traceless (TT) gauge. The explicit expressions for h_+ and $h_\times$ are:

$$h_+ \equiv h^{TT}_{xx} = -h^{TT}_{yy} = \frac{2G}{c^4}\frac{E}{D}\frac{\beta^2\sin^2\theta_v}{1-\beta\cos\theta_v}\cos 2\Phi\,, \tag{5.3}$$

$$h_\times \equiv h^{TT}_{xy} = h^{TT}_{yx} = \frac{2G}{c^4}\frac{E}{D}\frac{\beta^2\sin^2\theta_v}{1-\beta\cos\theta_v}\sin 2\Phi\,, \tag{5.4}$$

where G is the gravitational constant, D the distance between the object and the observer, $\beta = v/c$ is the velocity normalized with respect to the speed of light, θ_v is the angle between the direction of the observer and the direction of the velocity vector, i.e.

$$\cos\theta_v = \hat{n}\cdot\hat{\beta} = (\beta_R \sin\theta_{\rm obs}\cos\phi + \beta_z \cos\theta_{\rm obs})/\beta\ , \tag{5.5}$$

$E = (\rho H\gamma^2 c^2 - p)\Delta V$ is the energy of the fluid element, being ρ the mass density, γ the Lorentz factor, p the pressure, $H = 1 + 4p/(\rho c^2)$ the specific enthalpy (by considering a hot plasma with an adiabatic index $\Gamma_{\rm ad} = 4/3$), ΔV the volume of the fluid element which induces the metric perturbation, and Φ is the polar coordinate, measured in the observer frame.

To find the value of Φ, we consider the following geometric relations between the angles evaluated in the observer frames (indicating the azimuthal and polar directions by the capital Greek letters Φ and Θ respectively) and those in the laboratory frame (e.g., the frame centered on the central engine; see, Akiba et al. 2013):

$$\cos\Theta = \hat{n}\cdot\hat{r} = \sin\theta\cos\phi\sin\theta_{\rm obs} + \cos\theta\cos\theta_{\rm obs}, \tag{5.6}$$

$$\sin\theta\sin\phi = \sin\Theta\sin\Phi, \tag{5.7}$$

$$\sin\theta\cos\phi = \sin\Theta\cos\Phi\cos\theta_{\rm obs} + \cos\Theta\sin\theta_{\rm obs}\ , \tag{5.8}$$

which lead to

$$\sin(2\Phi) = 2\sin\theta\sin\phi\left(\frac{\sin\theta\cos\phi\cos\theta_{\rm obs} - \cos\theta\sin\theta_{\rm obs}}{\sin^2\Theta}\right), \tag{5.9}$$

$$\cos(2\Phi) = \frac{(\sin\theta\cos\phi\cos\theta_{\rm obs} - \cos\theta\sin\theta_{\rm obs})^2 - \sin^2\theta\sin^2\phi}{\sin^2\Theta}. \tag{5.10}$$

In the case of an on-axis observer, i.e. located along the z-axis, $\theta_{\rm obs} = 0$, and we recover the obvious result $\Phi = \phi$. In this case, for the symmetry of the problem, we get $h_+ = h_\times = 0$.

On the other hand, in the case of a particle moving along the z axis, we have $\theta = 0$, which implies

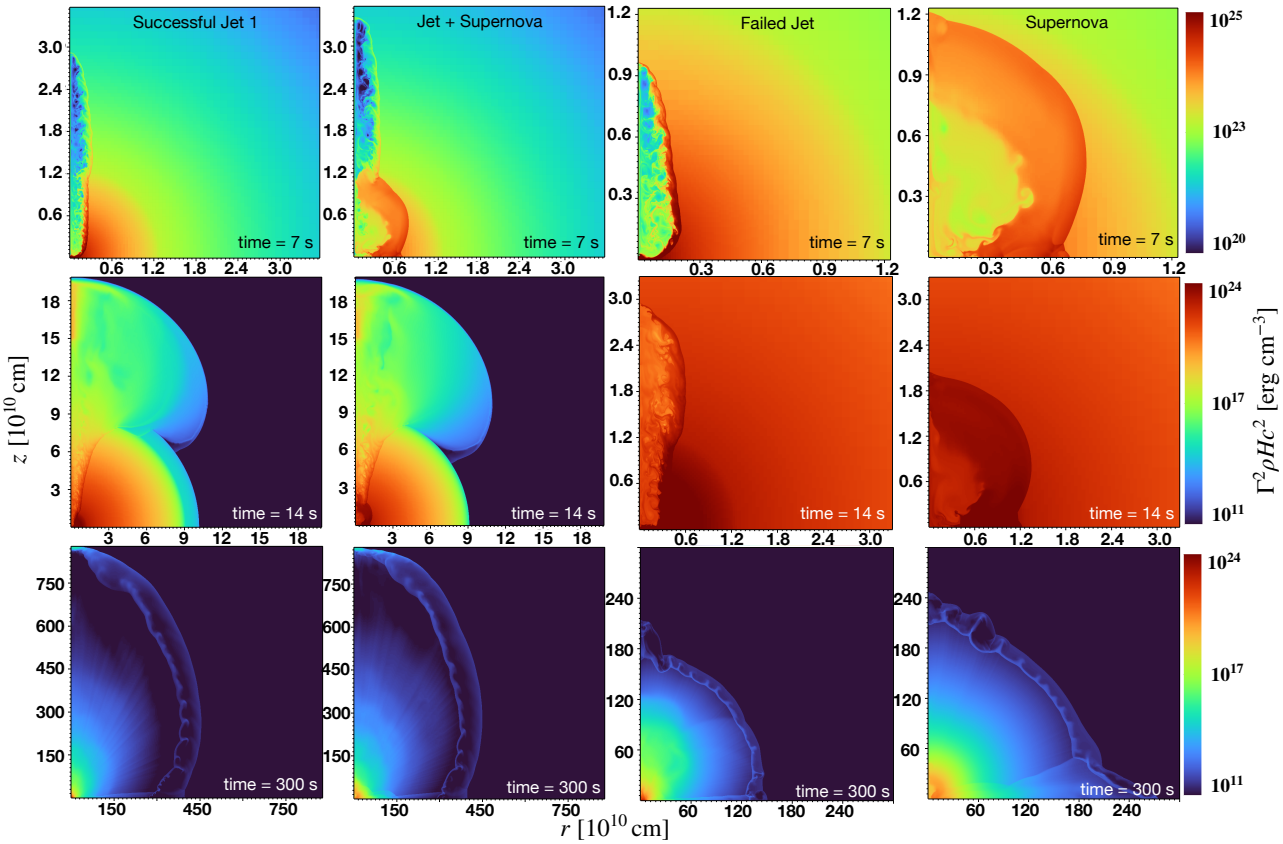

Figure 5.2: Two-dimensional plots (in cylindrical coordinates, in the r-z plane) of the energy density $\Gamma^2 \rho H c^2$. *Left to right panels:* successful jet, jet associated to a supernova, choked jet and SN explosion, respectively. *Top to bottom panels:* different evolutionary phases of the system, corresponding to 7 s (when the jet is propagating inside the progenitor star), 14 s (when successful jets have broken from the stellar surface) and 300 s (at the end of simulation).

$\sin(2\Phi) = 0$, $\cos(2\Phi) = 1$, and $h_\times = 0$. Also, being $\beta = \beta_z$ in this case, we get $\cos\theta_v = \cos\theta_{\rm obs}$, and

$$\frac{\beta^2 \sin^2\theta_v}{1-\beta\cos\theta_v} = \frac{\beta^2(1-\cos^2\theta_{\rm obs})}{1-\beta\cos\theta_{\rm obs}}. \tag{5.11}$$

This function has a maximum ($= 2(\gamma-1)/\gamma$) at $\cos\theta_{\rm obs} = \beta\gamma/(\gamma+1)$. In particular, for an ultra-relativistic flow, $\gamma \gg 1$, and the maximum ($= 2$) is at $\theta^2_{\rm obs} \sim 2/\gamma$. Thus, the GW signal determined from equation (5.3) is weakly boosted along the direction of the observer, except for observers located nearly along the jet axis (in which case $h_+ = 0$ as shown above).

In practice, the calculation of the GW signals proceeds as follows. We save a large number of snapshots of our two-dimensional, axisymmetric simulations at $t = t_i$, with $i = 1, .., 600$ (i.e., 600 outputs, spaced by 0.5 s, during the total integration time of 300 s). The data files include the positions R, z and the size ΔV of each cell, in addition to the thermal pressure, mass density and the velocity vector. Then, we remap each cell along the azimutal ϕ direction. We compute the values of h_+ and $h_\times$ (to verify that it remains ~ 0 at all times). Then, we compute the arrival time of the GW signal generated by that particular cell, that is,

$$t_{\rm obs} = t_i - (R/c)\cos\phi\sin\theta_{\rm obs} - (z/c)\cos\theta_{\rm obs}\ . \tag{5.12}$$

We divide the time-space in the observer frame in $N_{\rm obs}$ equally-spaced time-bins. Then, we add the contribution of a certain cell to the corresponding time bin to determine h_+ as a function of the observer time.

5.3.3 Calculation of the amplitude spectral density

When a GW passes through the LIGO-VIRGO (Aasi et al., 2015; Acernese et al., 2015) interferometer system, it produces a time-series data, i.e., a succession of data points measured at certain times. The data represent the strain produced by the GW signal coming from astrophysical sources (in our study, the relativistic jet and supernova). The measured data $s(t)$ is a combination of the detection noise $n(t)$ and the GW signal $h(t)$ (Moore et al., 2015):

$$s(t) = h(t) + n(t). \tag{5.13}$$

where $h(t) = \sqrt{h_+^2 + h_\times^2}$. The sensitivity of a detector to these polarizations depends upon the relative orientations of the source and detector. The challenge in the data analysis is to separate the GW signal from the noise for a given observation.

In the frequency domain f, the characteristic GW strain is defined as:

$$[h_c(f)]^2 = 4f^2|\tilde{h}(f)|^2, \tag{5.14}$$

where $\tilde{h}(f)$ is the Fourier transform of the strain $h(t)$, and the noise amplitude is:

$$[h_n(f)]^2 = f^2 S_n(f), \tag{5.15}$$

where the function $S_n(f)$ is called the Noise Spectral Density (NSD) and the signal noise ratio (SNR) can be defined by:

$$\text{SNR} = \int_0^\infty df \frac{4|\tilde{h}(f)|^2}{S_n(f)} \ . \tag{5.16}$$

This characteristic strain for an astrophysical source is the amplitude of the wave times the square root of the number of periods observed. Furthermore, the amplitude spectral density (ASD) is computed as

$$ASD = \sqrt{h_c(f) f^{-1/2}} = 2f^{1/2}|\tilde{h}(f)| \ . \tag{5.17}$$

The ASD is a crucial element for characterizing the detection strain during the data analysis.

The ASD and SNR are computed in this paper by considering the strain $h(t)$ computed as described in section 5.3.2, by computing the Fourier transform and by applying equations (5.16) and (5.17).

The SNR for binary black holes detected by the LIGO/VIRGO network is between 6 and 26, with most events detected with a SNR[2] of 10-20. Thus, in this paper we consider a conservative value SNR = 10 as detectability limit of the GW signal computed from the numerical simulations.

5.4 Results

5.4.1 Jet dynamics

In this section, we describe the dynamics of the system for the different numerical simulations. Figure 5.2 shows three different evolutionary times (at 7 s, 14 s and 300 s from the top to the bottom panels) for, from left to right, a successful jet without and with an associated SN (models "successful jet 1" and "jet + supernova", for the choked jet (the "failed jet" model) and for a SN-like explosion (the "supernova" model).

[2]See, e.g., https://www.gw-openscience.org/eventapi/html/allevents/

The "successful jet 2" model is qualitatively similar to the "successful jet 1" model (although the jet breaks out on a shorter timescale, as we will discuss below) and it is not shown in the figure.

As shown in Figure 5.2 (top panels), the "successful Jet 1" and "jet + supernova" models expands through the stellar material. At the shock front, the stellar material is heated and accelerated by the forward shock, while (in the lab frame) the jet material, launched from the central engine and propagating through the jet channel, is heated and decelerated by the reverse shock. The hot, entropy rich post-shock material expands sideways into the progenitor star, producing an extended cocoon (see, e.g., Bromberg et al., 2011b; Gottlieb et al., 2018a), which helps collimating the jet. Despite this extra collimation, the jet velocity is sub-relativistic while the jet moves through the star (see Figures 5.2 and 5.3).

Once the jet breaks out from the stellar surface (Figure 5.2, for the "successful jet 1" and "jet + supernova" models), the cocoon expands laterally quickly engulfing the low density region surrounding the progenitor star, while the entropy rich material, close to the jet axis, accelerates converting thermal to kinetic energy. The cocoon material remains strongly stratified both along the radial and the polar direction, moving at mildly relativistic speeds (close to the jet axis) and sub-relativistic speeds close to the equatorial plane.

Once the jet expands to larger distances (Figure 5.2, left-bottom panel), the fast moving material remains confined into a thin shell with size $\gtrsim t_j c$ ($\sim 3 \times 10^{11}$ in the successful jet simulations shown in the figure), where t_j is the time during which the jet is injected by the central engine. On the other hand, the cocoon begins to decelerate, specially close to the equatorial plane where the cocoon energy is lower, as indicated by the presence of Rayleigh-Taylor instabilities visible in Figure 5.2.

The simulation of the jet associated to a SN (the "jet + supernova" model) is qualitatively similar to the one without the SN (the "successful jet 1" model). In this simulation, the jet is launched with a delay of 1 s with respect to the SN. After a few seconds, the jet head reaches the SN shock front, breaking out of it and expanding through the progenitor star. The late phases are also similar to the case of a jet without a SN discussed above, except that, at large times, the SN shock front breaks out from the progenitor star into the jet cocoon.

We notice that the general outcome of the system depends on the time when the jet breaks out from the SN. If, for instance, the jet energy, opening angle and duration are such that the SN shock front breaks out first from the stellar surface, then the jet will remain trapped inside the expanding SN, depositing its energy in the deep layers of the SN ejecta. The result of the interaction between the SN, the jet and its cocoon leads to a rich landscape of scenarios which have not been studied in detail yet (see De Colle et al., 2021, for a qualitative

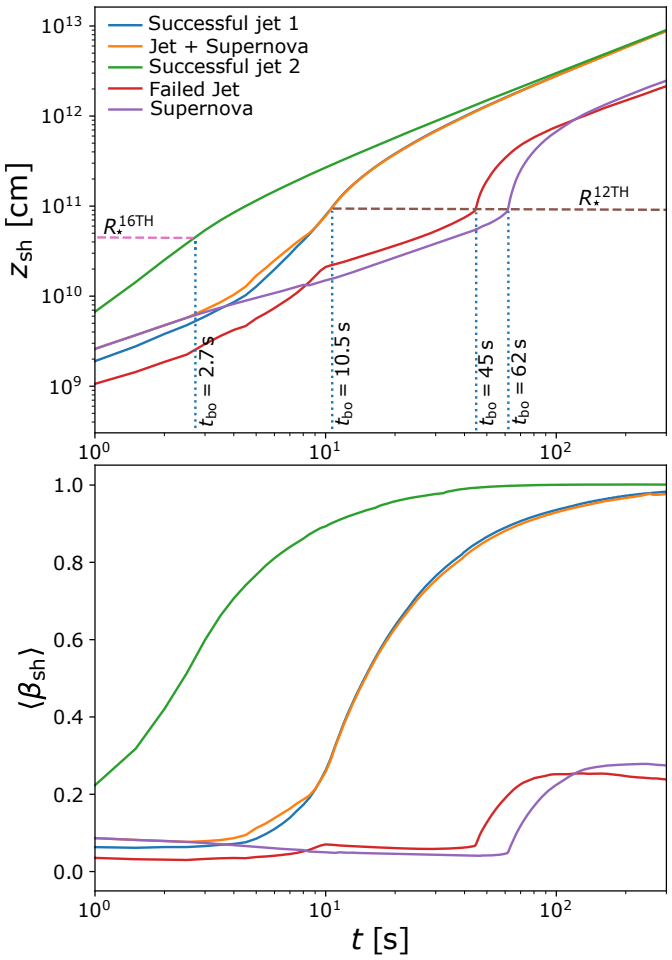

Figure 5.3: *Top panel:* Position of the head of the jet and supernova models (as indicated by the labels) as a function of time. The horizontal dotted lines represent the radius of the star for the progenitor 16TH ($R_\star^{16TH} = 4.5 \times 10^{10}$ cm) for the "successful jet 2" model (i.e., the jet with an energy $E_{jet} = 10^{52}$ erg) and 12TH for all other models (with a radius $R_\star^{12TH} = 9 \times 10^{10}$ cm). The vertical dotted lines refer to the time in which the jet or SN head break out from the progenitor star. *Bottom panel:* Average shock velocity in units of speed of light c , as a function of time.

description).

The third column of Figure 5.2 shows the case of a choked jet (the "failed jet" model). In this case, the jet opening angle is larger by a factor of ~ 2, so that the luminosity per unit solid angle drops by a factor of ~ 4. Then, the jet duration (10 s) is not large enough for the jet to break through the progenitor star. Once the jet power is switched off, the relativistic moving material crosses the jet channel in a time $R_h/c \sim \beta_h t_j$, being R_h and $\beta_h \sim 0.1 - 0.3$ c the head position and velocity, and t_j the jet injection time. Once all the jet material arrives to the head of the jet, the jet quickly expands laterally and decelerate. Then, it can break out from the stellar surface into a more spherical explosion (see the bottom panel of the figure).

The last column of Figure 5.2 shows a nearly spherical explosion, qualitatively representing a SN explosion (the "supernova" model). In this case, the shock breakout is also nearly spherical. Nevertheless, we notice that realistic 3D simulations of SN explosions show a much more asymmetric, turbulent behaviour not captured in these 2D simulations.

Figure 5.3 shows the evolution of the head of the jet ($z_{\rm sh}$ hereafter) and its average velocity, as a function of time, for the different models. As discussed above, the velocity of the shock front is sub-relativistic inside the progenitor star. Once the shock front approaches the stellar surface, it quickly accelerates due to the large density gradients. This is visible both in the top panel of Figure 5.3, where the slope of the curves showing $z_{\rm sh}$ vs t becomes steeper just after the breakout (represented by the vertical dotted lines), and in the bottom panel, where the average velocity increases quickly after the breakout. Then, the SN and the choked jet cases achieve a velocity of ~ 0.2 c, while the successful jets (with or without SN associated) continue accelerating until the end of the simulation. As mentioned before, the acceleration process is related to the conversion of thermal to kinetic energy. At the end of the process, the jet head will arrive to a terminal Lorentz factor $\Gamma_j \sim E_j/M_j c^2 \gg 1$.

Finally, we notice that the high luminosity model ("successful jet 2") is qualitatively similar to the "successful jet 1" model, with the main difference being the timescales for the different phases to occur. As the luminosity is larger, the jet duration is shorter, and the progenitor star is smaller, the jet will break out from the stellar surface in a much smaller time, and it will accelerate faster to its final velocity (see Figure 5.4).

5.4.2 GW emission

To understand where the GW signal originates from, we show in Figure 5.4 the amplitude of the GW signal h_+ as a function of z, at different times, i.e., integrating over the radial and azimuthal directions. During the

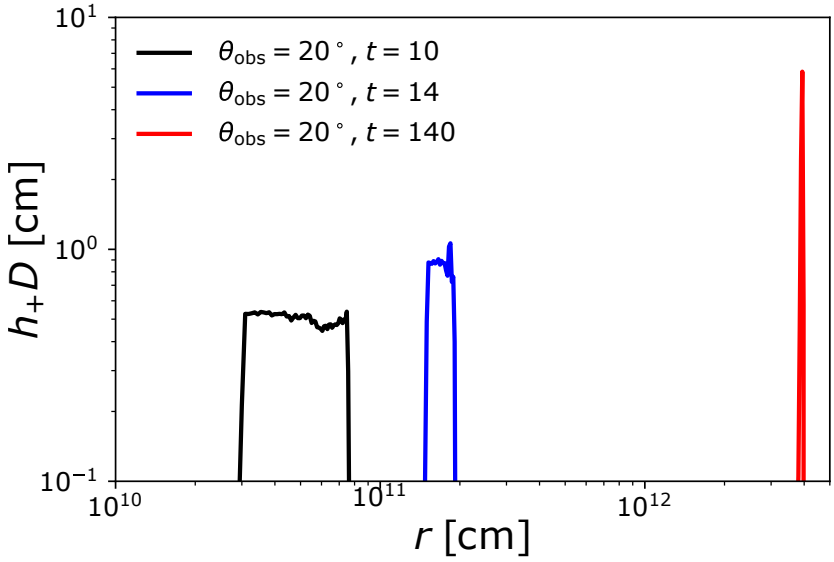

Figure 5.4: GW signal h_+ as a function of z extracted from the "jet+supernova" model, corresponding to $t = 10$ s, $t = 14$ s and $t = 20$ s (in the lab frame). The observer is located at $\theta_{obs} = 20°$. The figure shows that the GW signal is generated along all the jet channel (black, blue curves) at early times, and in a thin shell at large times (red curve), corresponding to the location of the highly relativistic material.

first 10 s, the jet is continuously injected into the computational box, and the jet energy increases along the jet channel (see Figure 5.3). As shown by the black curve, corresponding to $t = 10$ s, the GW signal is produced along most of the jet channel. The small fluctuations correspond to the presence of recollimation shocks. As the jet pressure is larger than the cocoon pressure, the jet expands laterally into the cocoon, until when both pressures are approximately equal. Then, a recollimation shock is created, pinching the jet onto the jet axis. This produces strong fluctuations in the jet velocity and energies, which lead to the observed fluctuations in the GW signal seen in Figure 5.4.

Once the jet breaks out from the star, the energy and velocity into the emitting region becomes more uniform. As discussed above, the jet velocity increases strongly achieving a Lorentz factor close to the terminal value (set to 100 in the simulation, see section 5.3). While a fraction of the total energy is stored in the cocoon, the cocoon does not contribute significantly to the GW signal, as it moves at most at mildly relativistic speeds. This can be seen in the red curve shown in Figure 5.4 (corresponding to $t = 140$ s), in which it is evident that the region emitting the GW signal is limited to the fast moving jet material.

Figure 5.5 shows h_+D as a function of time. $h_\times D$, not shown in the figure, remains close to zero (at machine precision) at all time, given that all simulations are axisymmetric. To illustrate the effect of the arrival times

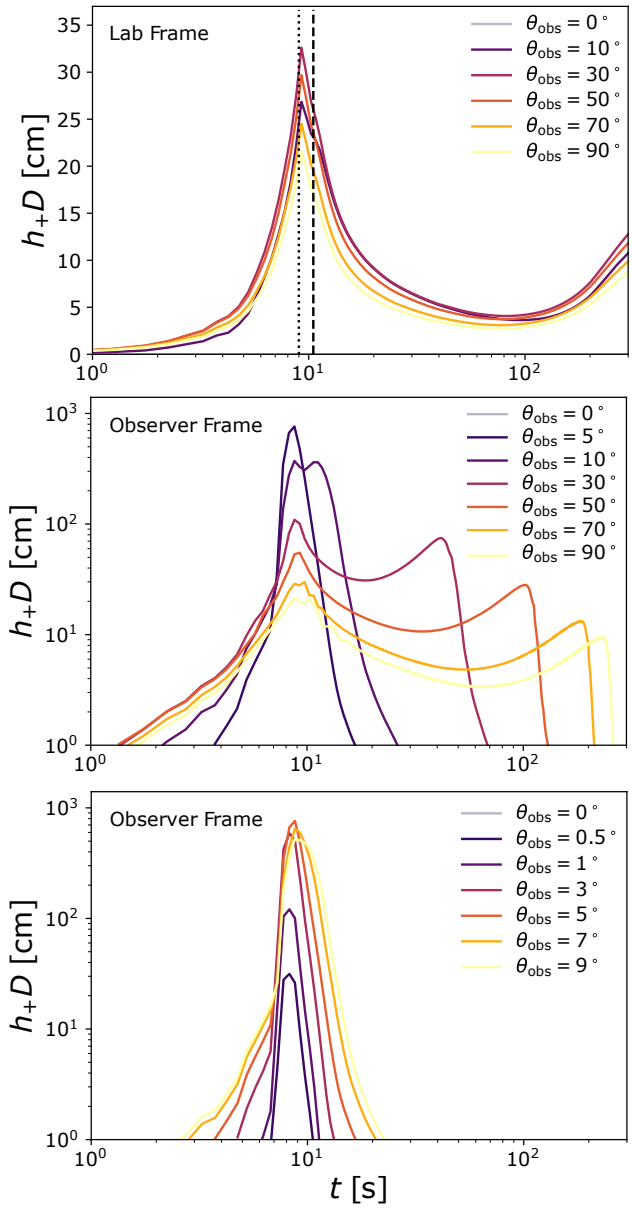

Figure 5.5: GW strain (multiplied by distance D) as a function of the lab frame time (top panel) and the observer time (center, bottom panels). The different curves correspond to different observer angles, ranging from 0° to 90° in the top panel, center panels, and from 0° to 9° in the bottom panel. The calculations correspond to the case of a successful jet with a duration of 10 s without any associated SN (model "successful jet 1). The vertical dotted and dashed lines in the top panel refer to the jet injection time (9 s) and the jet break out time (∼10.5 s).

on the shape of the GW signal, we show the GW amplitude in the lab frame (top panel), i.e., computed assuming $t_{\rm obs} = t$ in equation (5.12), and in the observer frame (center, bottom panels) for the successful jet model without an associated SN. In the lab frame, the GW signal presents two peaks, the first one at $t = t_j$, i.e., corresponding to the time when the jet power is switched off from the central engine, and the second at the very end of the simulation, corresponding to the acceleration of the jet to its terminal velocity.

Equation (5.3) implies that a constantly powered jet with constant velocity (along the z-axis) and $E_j = L_j t$, with also $L_j(t) = L_j$ constant, would produce a GW signal increasing linearly with time (see also Yu 2020). Figure 5.5 shows that the increase before the first peak is not linear, due to the jet acceleration as it approaches the stellar surface and it moves through a thinner medium (see Figure 5.3, bottom panel). As soon as the jet luminosity starts dropping[3] at $t = 9$ s, the GW amplitude quickly drops with time. At larger distances from the central engine, the GW amplitude increases again due to the acceleration of the jet material. Once the jet achieves its terminal velocity, that is, after transforming most of its thermal to kinetic energy, the GW amplitude achieves a second peak before dropping again with time. Unfortunately, the second peak is not completely resolved in our simulations, as it happens (in the lab frame) at times larger than the simulated 300 s. Then, the value of the GW signal at the second peak should then be taken as a lower limit to the real value. In the lab frame, the dependence on the observing angle is weak. Except for observer located exactly on the jet axis, for which $h_+ = 0$, there is a difference $\lesssim 2$ between the values of h_+ computed at different observer angles.

The central and right panels of Figure 5.5 show the same calculations, but in the observer frame. A qualitative understanding of the behaviour of h_+ in this case can be attained by assuming that all GW signal is coming from a region very close to the jet axis. In this case, $R = 0$, and equation (5.12) reduces to

$$t_{\rm obs} = t_n - (z/c)\cos\theta_{\rm obs} \ . \tag{5.18}$$

Then, assuming that the emission comes from a single point source moving with constant velocity β, we get

$$t_{\rm obs} = t\,(1 - \beta\cos\theta_{\rm obs}) \ . \tag{5.19}$$

For observers located at large observing angles, $\theta_{\rm obs} \gg 0$, $t_{\rm obs} \sim t$ and the GW arrival time is the same as the time when the signal is produced (except of course for the time D/c needed for the signal to propagate from

[3]The jet injection time is $t_j = 10$ s, but, to avoid numerical problems related with the strong rarefaction wave produced once the jet is switched off, we set a jet luminosity dropping linearly between 9 s and 10 s.

the source to the Earth). On the other hand, for observers located at small observing angles,

$$\cos\theta_{\rm obs} \sim 1 - \frac{\theta_{\rm obs}^2}{2}, \tag{5.20}$$

and

$$t_{\rm obs} \sim t\left(1 - \beta + \frac{\beta\theta_{\rm obs}^2}{2}\right) \sim t\ \frac{1 + \Gamma^2\theta_{\rm obs}^2}{2\Gamma^2}. \tag{5.21}$$

Then, for

$$\theta_{\rm obs} \ll \frac{1}{\Gamma} \sim 6^\circ \left(\frac{\Gamma}{10}\right)^{-1}, \tag{5.22}$$

we have

$$t_{\rm obs} \sim \frac{t}{2\Gamma^2}, \tag{5.23}$$

and the GW signal arrival time is reduced by a factor of a few hundred with respect to the GW signal as seen in the lab frame, while for $\theta_{\rm obs} \gg 1/\Gamma$, we have

$$t_{\rm obs} \sim \frac{t\theta_{\rm obs}^2}{2}. \tag{5.24}$$

As shown in Figure 5.5, the GW signal is very different in the observer frame with respect to the lab frame. Consistently with the discussion above, the second peak moves to increasingly smaller observer times for smaller observer angles. So, at $\theta_{\rm obs} = 5^\circ$, the second peak drops substantially, overlapping the first peak. As the simulations output files are saved every 0.5 s, this implies that, for this observer angle, the two peaks are separated by less than 0.5 s., while, e.g., the second peak moves at $\sim$ 12 s, $\sim$ 22 s for observers located at $\theta_{\rm obs} = 10^\circ, 20^\circ$ respectively. As more GW radiation arrives during a shorter time, the amplitude of the two peaks increase substantially, specially for small observer angles. The bottom panel shows that the maximum in the GW signal is obtained between $\theta_{\rm obs} = 3^\circ$ and $\theta_{\rm obs} = 7^\circ$, i.e., for observers located at the edge of the jet. Although it is barely visible due to the size of the bins in time (0.5 s as mentioned before), the break-out from the progenitor star produces a small change in the slope of the curves.

Figure 5.6 shows the GW amplitude h_+D for the other models considered. The "successful jet 1" and "jet + supernova" models produce similar results (compare the upper panel of Figure 5.6 with the middle panel of Figure 5.5). The GWs produced by the luminous, "successful jet 2" shown in the second panel also presents a similar behaviour, but with peaks located at shorter times, and a much larger amplitude at peak ($\sim$ 13000 cm vs $\sim$ 650 cm). In the case of the "failed jet", h_+ increases for $t \leq t_j$, to then drop on a short timescale ($\lesssim$ 0.5

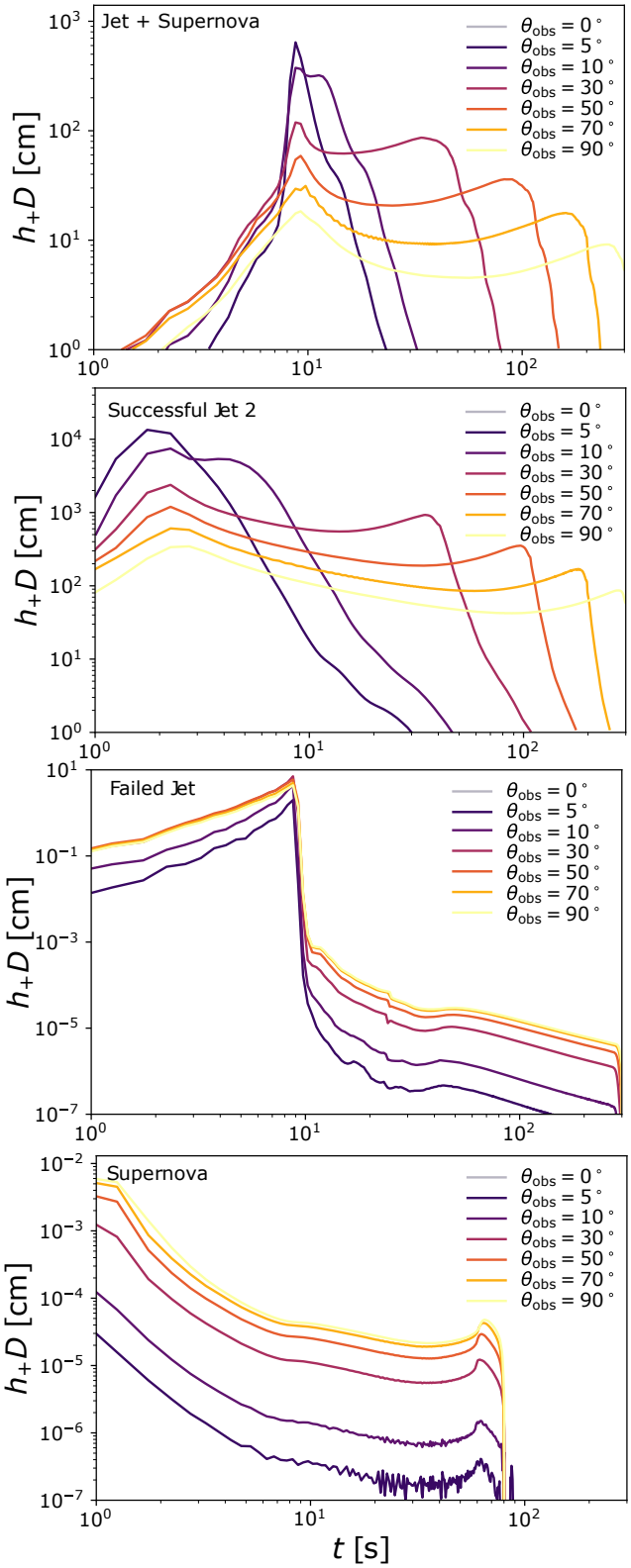

Figure 5.6: GW strain as a function of the observer time for the models considered in the paper. *From top to bottom*: successful jet associated to a SN, successful jet with a shorter duration and moving through a more compact star, choked jet and SN model. The different models are computed at different observer angles θ_{obs}.

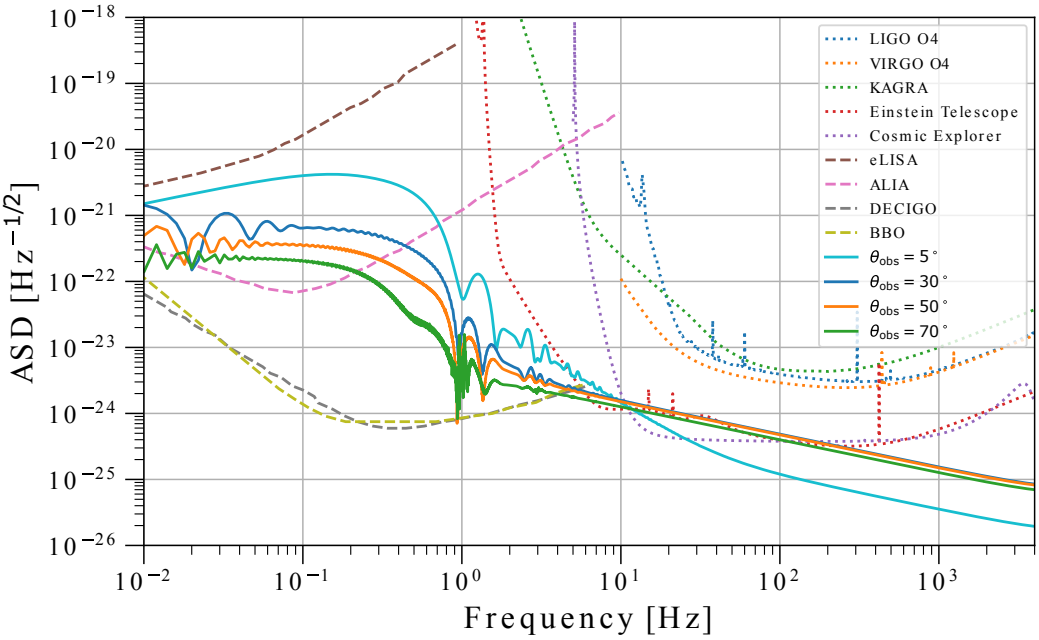

Figure 5.7: Comparison between the amplitude spectral density (ASD) GW signal computed from the "successful jet 2" (lasting $t_j = 2.5$ s) at $D = 1$ Mpc, and the ASD of the noise floor for LIGO 04, VIRGO 04, Kagra, the Einstein Telescope, eLISA, DECIGO, the Big-bang Observatory (BBO) and the Advanced Laser Interferometer Antenna ALIA. Dotted lines refer to ground-based interferometers, while dashed lines refer to space-based interferometers. The detection limits were taken from Moore et al. (2015).

s). The peak achieved for this model is $\sim 2-3$ order of magnitude smaller than in the other cases. Finally, the GW signal produced by a supernova is several orders of magnitude smaller, as the velocity of the SN shock front remains always sub-relativistic. Anyway, we note that our simulations do not capture the initial, larger GW signal produced by the early propagation of the SN shock front immediately after the collapse, because we follow the propagation far away from the central engine.

5.5 Discussion

In this paper, we have presented numerical simulations of the propagation of relativistic jets through a massive, progenitor star, the break-out and the expansion of the jet up to distances $\sim 10^{13}$ cm, and computed the resulting GW signal as a function of the observer angle.

Previous studies of GW memory from GRB jets have focused on the neutrinos produced by the central engine during the jet formation (Hiramatsu et al., 2005; Suwa & Murase, 2009; Kotake et al., 2012), on internal

shocks and shock deceleration during late stages of evolution (Akiba et al., 2013) and on the jet acceleration (Birnholtz & Piran, 2013; Yu, 2020; Leiderschneider & Piran, 2021b). These studies have used an analytic description of the jet, often taken as an accelerating point mass. In our study we compute the GW signal by using the dynamics of the jet while it crosses the progenitor star and it accelerates through the circumstellar medium. Although our results qualitatively confirm previous findings, our numerical simulations allow us to give a quantitative prediction of the expected GW signal.

Akiba et al. (2013) showed that the GW signal computed during the shock deceleration is about ~ 1000 times smaller than the one determined by our simulations, although we sample different distances, with our simulations extending up to 10^{13} cm, while Akiba et al. (2013) studied the propagation of the jet during the prompt emission, i.e. at $R_{\rm sh} \sim 10^{13} - 10^{15}$ cm.

Birnholtz & Piran (2013); Leiderschneider & Piran (2021b) studied the acceleration of the jet up to ultra-relativistic speeds. They showed that the jet acceleration produces a peak in the GW signal, which depends on the observer angle. Their study can be applied, in our context, to the acceleration of the jet when it breaks out from the star. Thus, the peak they observe in their calculations is equivalent to the second peak seen in Figure 5.5 and 5.6.

Yu (2020) employed an analytical model for the dynamics of the jet through the progenitor star (applying it also to sGRBs). They computed the acceleration of the shock front as it approaches the stellar surface. Although the results are qualitatively similar, the temporal evolution of $h_+ D$ is different (compare, e.g., their Figure 3 with our Figures 5.5 and 5.6). As they mention, observing the GW signal would probe the jet propagation and the interior of the progenitor star. Nevertheless, we argue in this paper that numerical models are needed to get a proper quantitative prediction.

The GW signal is "anti-beamed" (Segalis & Ori, 2001; Sago et al., 2004; Birnholtz & Piran, 2013; Leiderschneider & Piran, 2021b). Nevertheless, we notice that the GW signal is strongly suppressed only for observer located at $\theta_{\rm obs} \approx 0°$. As shown in the bottom panel of Figure 5.5, it increases for larger observer angles (respect to the jet opening angle θ_j), peaking at $\theta_{\rm obs} \sim \theta_j$ (e.g., the GW signal is $\sim 1/2$ of the peak at $\theta_{\rm obs} = \theta_j/2$). In contrast with the prediction obtained by considering analytical models, then, we expect to see GWs associated to GRBs seen nearly on-axis. Also, we expect than in three-dimensional numerical simulations, in which the symmetry with respect to the main axis of propagation of the jet is broken, the propagating jet would produce a GW signal also on-axis.

The other clear feature resulting from our models is the presence of a double peak structure in the GW

signal, due to two characteristic acceleration phases: a) inside the progenitor star, as the jet move through a lower density medium as it approaches the stellar surface; and b) after the breakout, as the jet accelerates converting thermal to kinetic energy. The timescales of the two peaks reflect directly the duration of the jet t_j (the first peak) and the observer angle (with larger timescales corresponding to larger $\theta_{\rm obs}$, see Figures 5.5 and 5.6).

As discussed above, the slope of the GW signal before and after the first peak (see, e.g., Figure 5.6) depends on the stellar structure and on the jet luminosity. For instance, we can expect a shallower increase for a jet with a luminosity decreasing with time. Thus, observations of h_+ by future detectors may provide direct information on the central engine activity (e.g., jet duration and luminosity history), the stellar structure, the observer angle and the acceleration process after breakout.

Figure 5.7 shows the amplitude spectral density computed from the numerical simulation of the "successful jet 2" model, by employing the methods described in Section 5.3.3 (see also Szczepańczyk et al. 2021; Richardson et al. 2022). In the figure, we can observe the range of frequency 10^{-2} – 10^{3} Hz and the ASD 10^{-26} – 10^{-10} Hz$^{-1/2}$ for several interferometers, and for the astrophysical signal analyzed in our study.

LIGO-VIRGO detectors were the first-generation detectors. They have completed science runs O1, O2, O3. They are currently being upgraded for O4 which will start to take data during February 2023. The KAGRA (Aso et al., 2013) interferometer detector will join the LIGO/VIRGO collaboration during 2023. Future interferometer include (Moore et al., 2015) the Laser Interferometer Space Antena (eLISA), the Advanced Laser Interferometer Antenna (ALIA) (Sathyaprakash & Schutz, 2009), DECIGO, the Big Bang Observer (BBO, Yagi & Seto 2011), and the Einstein Telescope (ET)/Cosmic Explorer (CE) (Hild et al., 2011). The ASD for all these interferometers are included in Figure 5.7.

Figure 5.7 shows the ASD computed from the simulation assuming a GRB jet at 1 Mpc. The signal peaks at low frequencies ($\sim$ 0.1 Hz), and depends strongly on the observer angle, with a peak between $5 \times 10^{-21}(D/1\ {\rm Mpc})^{-1}$ at $\theta_{\rm obs} = 5°$ and $2 \times 10^{-22}(D/1\ {\rm Mpc})^{-1}$ at $\theta_{\rm obs} = 70°$. At larger frequencies, the signal drops to much smaller values, being $\sim$ one order of magnitude below the ASD of LIGO/VIRGO. However, our times series is sampled each 0.5 s, corresponding to a maximum frequency of 2 Hz, so that results above this frequency should be taken carefully.

In table 5.2 we estimate the detectability of the "successful jet 2" model (i.e., a relativistic jet with a total energy of 10^{52} erg lasting 2.5 s), considering a distance of 40 Mpc (the second and third columns of table 5.2) using equation 5.16, for present and planned interferometers (first column) , at two characteristic observer

angles ($\theta_{\rm obs} = 5°, 70°$). The SNR is very low for ground-based interferometers ($\lesssim 4.4 \times 10^{-2}$), is ≈ 1 for ALIA and $\gg 1$ for DECIGO and BBO for a nearly on-axis observer (at $\theta_{\rm obs} = 5°$), and drops to smaller values for off-axis observers.

The third and fourth columns of table 5.2 show the distance (in Mpc) where SNR = 10, by using the relation Distance = $({\rm SNR}_{40\ {\rm Mpc}}/10) \times 40$ Mpc[4]. Only galactic GRBs can be detected (while crossing the progenitor star) by LIGO/VIRGO (with a SNR=10 at $1.5 - 5.1 \times 10^{-2}$ Mpc = 15-51 kpc depending on $\theta_{\rm obs}$) and Kagra (with a SNR=10 at $7.3 - 23 \times 10^{-3}$ Mpc = 7.3-23 kpc), while DECIGO and BBO can detect GRBs with an SNR=10 up to 18-600 Mpc depenging on the observer angle.

The (uncertain) expected GRB rate is 100-1000 Gpc^{-3} yr^{-1} (see, e.g., Fryer et al., 2002; Wanderman & Piran, 2010; Cao et al., 2011; Abbott et al., 2017a). The sixth and seventh columns of table 5.2 show the expected GRB/GW detection rate by assuming an (optimistic) GRB rate of 1000 Gpc^{-3} yr^{-1}. We compute the volume corresponding to a SNR of 10 for each solid angle, and the expected GRB rate within this solid angle[5]. The expected rate is very low for ground-based interferometers, while ~ 10 LGRB jets per year are expected to be detected by future spaced-based interferometers at small observer angles $\lesssim$, and ~ 1 per decade for GRB jets observed at $\theta_{\rm obs} = 40 - 90°$.

In agreement with previous estimates (Sago et al., 2004; Hiramatsu et al., 2005; Suwa & Murase, 2009; Kotake et al., 2012; Sun et al., 2012; Akiba et al., 2013; Birnholtz & Piran, 2013; Du et al., 2018; Yu, 2020; Leiderschneider & Piran, 2021b), the LGRB memory from jets crossing the progenitor stars are expected to be undetectable with LIGO/VIRGO and KAGRA. Given the (uncertain) expected GRB rate of 100-1000 Gpc^{-3} yr^{-1} (see, e.g., Fryer et al., 2002; Wanderman & Piran, 2010; Cao et al., 2011; Abbott et al., 2017a), the GW memory from jet/shock propagation in very rare galactic GRB jets is eventually detectable with LIGO/VIRGO. Future space-based low-frequency instruments, as DECIGO and BBO, will easily detect the GW memory from GRB jets located up to distances $\lesssim 600$ Mpc, as shown Table 5.2.

In addition to successful jets, producing the observed gamma-ray emission, other high energy transients are likely associated to a central engine activity and to the propagation of a relativistic jets, including low-luminosity GRBs (Campana et al., 2006; Soderberg et al., 2006; Starling et al., 2011; Margutti et al., 2013), relativistic SNe (Soderberg et al., 2010; Margutti et al., 2014; Milisavljevic et al., 2015), and X-ray flashes (Pian et al., 2006b; Bromberg et al., 2011a; Nakar & Sari, 2012). In addition, it has been suggested that SNe

[4]It is easy to rescale the detectability range for different SNR thresholds as the SNR is inversely proportional to distance.

[5]This is an order magnitude estimation. A more precise calculation would require to include the GRB energy and time duration distribution. We leave it for a future study.

Detector	SNR		Distance [Mpc]		Rate [yr^{-1}]		
	5°	70°	5°	70°	0° – 10°	10° – 40°	40° – 90°
LIGO O4	3.8×10^{-3}	1.3×10^{-2}	1.5×10^{-2}	5.1×10^{-2}	1.5×10^{-12}	1.9×10^{-10}	4.2×10^{-10}
VIRGO O4	2.0×10^{-3}	5.5×10^{-3}	2.2×10^{-2}	2.2×10^{-2}	7.3×10^{-13}	1.8×10^{-11}	3.6×10^{-11}
KAGRA	8.9×10^{-3}	2.8×10^{-3}	7.3×10^{-3}	2.3×10^{-2}	1.6×10^{-14}	2.1×10^{-12}	5.0×10^{-12}
Einstein Telescope	4.4×10^{-2}	6.2×10^{-2}	3.5×10^{-1}	5.0×10^{-1}	3.9×10^{-10}	2.3×10^{-8}	5.3×10^{-8}
Cosmic Explorer	3.8×10^{-2}	6.7×10^{-2}	3.0×10^{-1}	5.3×10^{-1}	3.4×10^{-10}	2.8×10^{-8}	6.4×10^{-8}
eLISA	2.1×10^{-2}	3.9×10^{-3}	8.5×10^{-2}	1.5×10^{-2}	5.5×10^{-11}	3.7×10^{-10}	4.0×10^{-11}
ALIA	1.6	9.3×10^{-2}	6.4	3.7×10^{-1}	1.3×10^{-5}	1.2×10^{-5}	4.5×10^{-7}
DECIGO	1.5×10^{2}	4.7	6.0×10^{2}	1.8×10^{1}	7.5	2.2	1.0×10^{-1}
BBO	1.5×10^{2}	5.4	6.0×10^{2}	2.1×10^{1}	7.9	2.5	1.2×10^{-1}

Table 5.2: The columns refer to: the observatories considered (see Figure 5.7), the signal-to-noise ratio (SNR) for a jet seen at an observer angle $\theta_{\rm obs} = 5°, 70°$ and at a distance of 40 Mpc, the distance where SNR = 10, and the number of events detected per year along different solid angles. The values refer to the "successful jet 2" model.

(in particular, broad-line type Ic) could be produced by the propagation of a choked jet (e.g., Piran et al., 2019; Soker, 2022).

These events could be detectable at shorter distances. Our results show that the GW strain h_+ depends mainly on the jet luminosity and the jet velocity. Jets choked while deep inside the progenitor stars, as the one simulated in this paper, will have a very low signal (see Figure 5.6, third panel) as their velocity is only mildly relativistic when the jet is switched-off from the central engine. Nevertheless, jets lasting for longer times, i.e. arriving closer to the stellar surface before being choked, will accelerate to relativistic speeds producing signals similar to those of successful jets.

Finally, we notice that, while we have simulated relativistic jets leading to LGRBs (i.e., associated to the collapse of massive stars), a similar outcome is expected for SGRBs, associated to the coalescence of massive stars. These jets are expected to last for shorter times, to have smaller total energies and can move through smaller density media, so than they could achieves relativistic velocities on shorter timescales. Detailed numerical simulations are needed to understand whereas the expected signal would be larger for jets associated to LGRBs or SGRBs.

5.6 Conclusions

In this paper, we have presented numerical simulations of relativistic jets associated to long GRB. We have computed the resulting GW signal for successful jets, choked jets, and jets associated to a SN. In successful

jets (accompanied or not by a SN), the GW signal is characterised by a double peak structure, with amplitudes h_+D ranging from hundreds to several thousand. The first peak corresponds to the jet injection from the central engine, while the second peak corresponds to the jet acceleration while it breaks out from the star. In addition, the slope of the GW signals track directly the luminosity history of the GRB jets, and the structure of the progenitor star.

As GRBs are the product of collimated jets seen nearly on-axis, given the detected GRB rate, the volumetric rate depends on the jet angle and on the jet structure. Thus, the GRB volumetric rate is highly uncertain ($\sim$ 100-1000 Gpc^{-3} yr^{-1}). As illustrated in Figures 5.5 and 5.6, the GW signal presents a second peak which strongly depend on the observer angle. Thus, the observer angle can be determined precisely by observing the GW signal. In addition, by observing the associated multi-wavelength afterglows, the jet structure can be determined. Thus, observations of the GW signal may provide us with a precise estimate of the volumetric rate of GRBs.

The predicted GW signal is below the detection limits of LIGO/VIRGO, KAGRA and similar Earth-based detectors, and is expected to be seen by lower-frequency space-based detectors as BBO and DECIGO. Future detections of GWs from GRBs may provide information on optically thick regions impossible to explore by electromagnetic radiation, clarifying the jet duration, the structure of the progenitor star and the jet acceleration process. It is also worth pointing out that the GW detectability can be improved with a network of interferometers. With the rough rule that, the SNR achievable with a network of identical interferometers is the single interferometer SNR multiplied by the square root of the number of interferometers in the network.

Chapter 6

Conclusions

This thesis focused on performing numerical simulations SRHD to study how the structure of the jet of a GRB can modify the jet dynamics and its afterglow emission, as well as the emission of GWs from long GRBs. The simulations 2D and 3D SRHD explored multiple jet structures and different ambient media, that is, a neutrino driven wind, or the massive star progenitor. Since GRBs present a very different behaviour at small distances from the central engine, i.e. $r \lesssim 10^{13}$ (corresponding to the prompt emission), vs. at large distances from the source, i.e. $r \gtrsim 10^{16}$ (corresponding to the afterglow emission), in this thesis the two stages of the jet dynamics are studies separately. Then, I write my conclusions according to the scale of the jet.

Small scale simulations of short GRBs: In Chapter 2, we discussed the dynamics of structured jets associated to short GRBs. The jets propagate through a spherical wind with a mass-loss $\dot{M}_w = 10^{-4} M_\odot$ s^{-1}. We follow the jet dynamics until 10^{11} cm. The main results are the following:

- The initial jet structure plays an important role in the jet dynamics when the density of the environments is low. The final structure (after breakout) is different when different structures are assumed at the injection point.

- We supposed that the jet structure is preserved during the free expansion phase, between $r \in [10^{13}, 10^{16}]$ cm. Then, extrapolating the structure of the jet to $r \sim 10^{16}$ cm, the afterglow radiation can be calculated. The light curves are different for different structured jet models. Structured jet light curves increase slowly before the peak for off-axis jets, while top-hat jet light curves increase quickly as $F \propto t^3$. The early time of the observed lightcurve of GRB 170817A is well fitted by our models, while late observations are not fitted due to the lateral expansion of the jet (not present in our analytical estimations).

- The $L(t)$ history modifies the structure: Since the energy is injected during a shorter period of time, the jet accelerates faster while moving through the environment.

- Jet parameters: as long as the jet duration is larger than the break-out time, i.e. $t_j \gtrsim t_{\rm bo}$, the jet is successful and the jet structure is preserved after the breakout. Changing t_j modifies the angular structure of the jet by increasing the energy close to the jet core. The jet luminosity at the launching point L_{0j} also modifies the angular structure of the jet since more luminous jets go through the environment at a larger speed. As a consequence, the jet structure is preserved for larger jet luminosities.

Small scale, long GRBs. In chapter 3, we present the results of 3D numerical simulations of long GRBs. The effect of the initial structure of the jet in a dense progenitor media was studied. The dense progenitor was a massive star of $M = 10 M_\odot$. Top-hat and Gaussian jet were studied with low and high luminosities. In addition, the dynamics of a Gaussian jet crossing a supernova (launched 1 s before the jet) was studied.

- Effects due to the initial jet structure: In a very dense media, the initial structure of the jet is quickly washed out. The final structures of the initial Gaussian and top-hat jets are indistinguishable. Nevertheless, the bow shock of structured jets is different with respect to the one of top-hat jets, being less sharp. Then, more structured jets drill less efficiently the dense medium. The final structure of the jet is dominated by the jet core. Also, the jet structure is substantially modified in jets with a very large (possibly unphysical) luminosity.

- Effects of the previously launched supernova on the jet dynamics: long GRBs are usually accompanied by a supernova. The supernova pushes up the dense material near the centre of the star. The shock front of the supernova forms a dense shell. When the jet head reaches this shell, the interaction leads to a deceleration of the jet and to a fragmentation of the jet head. Then, the break out time is much larger in jets interacting with a supernova.

- When is the initial structure important? Guided by the simulations presented in chapters 2 and 3, I conclude that the initial jet structure is preserved in lower density environment, luminous jets, or jets lasting longer times.

Gravitational Wave emissions from GRBs

- GW signals provide information on the jet dynamics in high opacity environment (when the electromagnetic counterparts can not be observed). So far, every observational constraint on the jet comes from electromagnetic signatures, in particular from the GRB light curves properties as, e.g., duration, energy, and fluctuations. In chapter 5, we show that GW signals produced by a long GRB follow the central engine activity and the interaction of the jet with the progenitor environment, i.e., GW radiation provides direct information of the jet in high opacity regions when electromagnetic radiation is not observed. When the jet is switched off at t_j, the GW signal presents a first peak. A second peak is produced just when the jet breaks out from the progenitor star and reaches its maximum velocity of propagation. Detection of GW signals could be very important to constrain the jet dynamics, in particular the jet energy injection, and the size of the progenitor.

- The amplitude of the GW signal: Since the GW signal is proportional to total energy and head velocity $h(t) \propto E\beta_h$, luminous jets (lasting $\lesssim 2.5$ s), produce a GW signal with an amplitude one order of magnitude larger than a jet lasting $\gtrsim 10$ s.

- Off-axis observers: The peak in the GW signal is observed at $\theta_{\rm obs,\,max} = \theta_j/2$. The amplitude decreases for larger values of $\theta_{\rm obs}$ and near to the jet axis $\theta_{\rm obs} < \theta$.

- Is the initial structure of the jet changing the GW emission? No! The jet core, where the material is faster and more energetic, is where most of the GW radiation is produced. Mildly relativistic jet wings do not contribute significantly to GW radiation.

- Future observation: Future Space based telescopes as BBO and DECIGO should be able to observe observe GRB signals at 1 Gpc for slightly off-axis GRBs and 40 Mpc for GRBs at large observing angles.

Large scales

- The afterglow radiation can be computed by extrapolating analytically the results of small scale simulations (see chapter 2). This approximation has limited applications (although is extensively employed in the literature) as it does not include the jet lateral expansion. The lateral expansion produces a slower decrease in the GRB light curves (see chapter 4)

- Lateral expansion: Chapter 4 shows that the jet structure changes abruptly as a function of time. Thus, analytical approximations not considering lateral expansion are not valid in general.

- Parametrisation of the jet cocoon: The cocoon always present around relativistic jets can be parametrised by different analytical functions (chapter 4). Chapters 2 and 3 show that the jet acquires a power-law distribution of energies as a function of polar angle as a result of their interaction with the environment. However, it is important to remark that numerical simulations are needed to reproduce the lateral expansion.

Appendix A

Integrating the SRHD equations

The *Mezcal* code (De Colle et al., 2012a) solves the hydrodynamic evolution of a relativistic fluid, by integrating the special relativistic hydrodynamics (SRHD) equations (1.1)-(1.2), i.e., the equations of mass ($D = \Gamma\rho$), momentum ($\vec{m} = \Gamma D h \vec{v}$) and energy ($E = Dh\Gamma c^2 - p$), conservation, being the density ρ, the thermal pressure p, the enthalpy h and Lorentz factor Γ. Defining a vector $\vec{U} = (D, m_x, m_y, m_z, E)$, the SRHD equations take the form

$$\frac{\partial U}{\partial t} + \frac{\partial F^x(U)}{\partial x} + \frac{\partial F^y(U)}{\partial y} + \frac{\partial F^z(U)}{\partial z} = 0, \tag{A.1}$$

being,

$$F^x(U) = \begin{pmatrix} Dv_x \\ m_x v_x + p \\ m_y v_x \\ m_z v_x \\ m_x \end{pmatrix}, \quad F^y(U) = \begin{pmatrix} Dv_y \\ m_x v_y \\ m_y v_y + p \\ m_z v_y \\ m_y \end{pmatrix}, \quad F^z(U) = \begin{pmatrix} Dv_z \\ m_x v_z \\ m_y v_z \\ m_z v_z + p \\ m_z \end{pmatrix}. \tag{A.2}$$

The solution of the system of equations (A.1) in one dimension (the extension to higher dimensions is straightforward) is:

$$U_i^{n+1} = U_i^n - \frac{\Delta t}{\Delta x_i}\left(F_{i+1/2}^{n+1/2} - F_{i-1/2}^{n+1/2}\right), \tag{A.3}$$

where x_i is the position of the center of the cell i, and the volume of each cell is $\Delta x_i = x_{i+1/2} - x_{i-1/2}$. The space and time-average of the conserved variables and fluxes are defined as

$$U_i^n = \frac{1}{\Delta x_i} \int_{x_{i-1/2}}^{x_{i+1/2}} u_i(t^n, x_i) dx, \tag{A.4}$$

$$F_{i\pm1/2}^{n\pm1/2} = \frac{1}{\Delta t} \int_{t_n}^{t_{n+1}} f(t, x_{i\pm1/2}) dt. \tag{A.5}$$

To determine the fluxes in (A.5), the *Mezcal* code employs the relativistic extension (Schneider et al., 1993) of the Harten, Lax, and van Leer (HLL) method (Harten, 1983). The HLL method is a high dissipation method, very rarely producing unphysical results such as negative pressures or imaginary Lorentz factors. In addition, a low dissipation method may produce undesirable effects, such as a carbuncle artefact along the axis of propagation of strong shocks (see the discussion by Wang et al., 2008). The code also employs the HLLC method which is a less dissipative method useful for the study of turbulence (Mignone & Bodo, 2005), as it properly reconstructs the contact discontinuity, producing results with significantly lower dissipation. In Urrutia et al. (2021) we employed the HLL method, while in Urrutia et al. (2022a); Urrutia et al. (2022b) we used the HLLC method.

The system of equations (A.1) is closed by the equation of state. Defining $\Theta = p/\rho c^2$, the enthalpy (1.4) can be expressed as,

$$h = 1 + \frac{\gamma}{\gamma - 1}\Theta \,, \tag{A.6}$$

being the density ρ, the pressure p, the speed velocity c, and the specific heat ratio γ. In concordance with relativistic kinetic theory, the enthalpy equation has to satisfy the Taub (1948) inequality

$$(h - \Theta)(h - 4\Theta) \leq 1. \tag{A.7}$$

Instead of using the general solution for Θ, the *Mezcal* code uses the Ryu et al. (2006) approximation which is less expensive and obeys the inequality (A.7), i.e.,

$$h = 2\frac{6\Theta^2 + 4\Theta + 1}{3\Theta + 2}. \tag{A.8}$$

Given the energy $e = Dh\Gamma c^2 - p - Dc^2$, it is easy to show that

$$f(\Theta) = \Gamma\, h(\Theta) - \frac{\Theta}{\Gamma} - \frac{e}{Dc^2} - 1 = 0. \tag{A.9}$$

This equation is solved by the Newton-Rapson method to determine the pressure from the energy.

Appendix B

Apendice B: GRB afterglow from *Mezcal* code

As discussed in the previous section, the hydrodynamics evolution of a blast wave provides the main parameters for the *afterglow* emission estimated through the standard synchrotron model. Now, I focus on the emission from an optically thin source. The main idea is to estimate the observed flux density $F_\nu = dE/dAd\nu dt$, which is the energy per unit area, per frequency, and time in the normal direction $\hat{n}$, perpendicular to dA. In the observer frame, the flux density is given by (De Colle et al., 2012a)

$$F_\nu(t_{\rm obs,\hat{n}}) = \frac{(1+z)}{4\pi d_L^2(z)} \int dt_z \delta\left(t_z - \frac{\hat{n}\cdot\vec{r}}{c} - \frac{t_{\rm obs}}{1+z}\right) \int \frac{dL'_{\nu'}}{\Gamma^3\left(1-\hat{n}\cdot\vec{\beta}\right)^3}, \tag{B.1}$$

being $\nu' = (1+z)\Gamma(1-\hat{n}\cdot\vec{\beta})\nu$, the Redshift z, the luminous distance d_L, and the observer time $t_{\rm obs} = (1+z)(t_z - \hat{n}\cdot\vec{r}/c)$. The luminosity is given by $dL'_{\nu'} = 4\pi(dE'/d\Omega' d\nu' dt')$, and t_z is the time coordinate in the cosmological frame. For 2D jet simulations, which assume an axisymmetric flow, the jet symmetry axis is the z-axis. The x-axis is defined along the $\hat{n}$-$\hat{z}$ plane, so that $\hat{n}$ may be easily expressed in terms of the viewing angle $\theta_{\rm obs}$, where $\theta_{\rm obs} = \hat{n}\cdot\hat{z}$, and

$$\hat{n} = \hat{x}\sin\theta_{\rm obs} + \hat{z}\cos\theta_{\rm obs}. \tag{B.2}$$

Assuming azimuthal symmetry[1] $\beta_\phi = 0$, the dot products, respectively for spherical and cylindrical coordinates are,

$$\hat{n} \cdot \vec{r} = r(\sin\theta\cos\phi\sin\theta_{\rm obs} + \cos\theta\cos\theta_{\rm obs}) = \rho\cos\phi\sin\theta_{\rm obs} + z\cos\theta_{\rm obs}, \tag{B.3}$$

$$\hat{n}\cdot\vec{\beta} = (\beta_r\sin\theta+\beta_\theta\cos\theta)\cos\phi\sin\theta_{\rm obs}+(\beta_r\cos\theta-\beta_\theta\sin\theta)\cos\theta_{\rm obs} = \beta_\rho\cos\phi\sin\theta_{\rm obs}+\beta_z\cos\theta_{\rm obs}. \tag{B.4}$$

De Colle et al. (2012a) proposed an approximated solution to equation (B.1), which consists in dividing $t_{\rm obs}$ in a finite number N_t of observed times $t_{\rm obs}$ for $i = 1, \ldots, N_t$. Then, the flux coming from a certain region of space (a cell of the numerical simulation) gives the contribution of the observed flux in a certain time interval. Each cell of the computational box contributes with a flux ΔF_ν, such that the total flux is $F_\nu \approx \sum_{l=1}^{N_{\rm cells}} F_{\nu,l}$. In equation (B.1) the 4-volume is expressed by taking the time as a vector multiplied by the 3-dimensional volume of each cell l. The 4-volume depends on the directions jk, then $l \rightarrow jk$, such that $\Delta V^{(4)}_{jk} = \Delta t_{z,jk}\Delta V^{(3)}_{jk}$. Taking $\Delta L'^{(4)}_{\nu'} = 4\pi j'_{\nu'}\Delta V'^{(4)}$, then the contribution of each cell to the flux is,

$$\Delta F_{\nu,i,jk}(\hat{n}) = \frac{(1+z)^2}{d_L^2(z)}\frac{\Delta V^{(4)}_{jk}}{\Delta t_{\rm obs,i}}\frac{j'_{\nu',jk}}{\Gamma^2_{jk}(1-\hat{n}\cdot\vec{\beta}_{jk})^2}. \tag{B.5}$$

Now, I will describe the connection between the flux calculation and the spectral breaks, such that $F_{\nu,max} \approx P_{\nu,max}N_e/4\pi D^2$. We assume that the emission is isotropic in the proper frame, i.e., $j'_{\nu'} = P'_{\nu'}/4\pi$. The spectral breaks DGH are defined in the proper frame as,

$$\frac{P'_{\nu'}}{P'_{\nu',\rm max}} = \begin{cases} (\nu'/\nu'_c)^{1/3} & \text{if} \quad \nu'_c > \nu' \quad \textbf{(PLS D)}, \\ (\nu'/\nu'_c)^{-1/2} & \text{if} \quad \nu_m > \nu' > \nu'_c \quad \textbf{(PLS G)}, \\ (\nu'_m/\nu'_c)^{-1/2}(\nu'/\nu'_m)^{-p/2} & \text{if} \quad \nu' > \nu'_m \quad \textbf{(PLS H)}, \end{cases} \tag{B.6}$$

which are consistent with Granot & Sari (2002). The contribution of each spectral region to the total light curve is given by

$$F_\nu(t) \approx \sqrt{F^2_{\nu,\rm PLS\,D}(t) + F^2_{\nu,\rm PLS\,G}(t) + F^2_{\nu,\rm PLS\,H}(t)}. \tag{B.7}$$

An example of the calculation of a light curve is shown in Figure B.1.

It is important to notice that the jet dynamics can scaled by considering different energies, densities and

[1]We can assume azimuthal symmetry due to the propagation of the fluid is on z-direction. The fluid is spread to the sides, along the z-x and z-y planes. Since the ambiance of propagation is uniform and isotropic, this means that the azimuthal symmetry can be preserved.

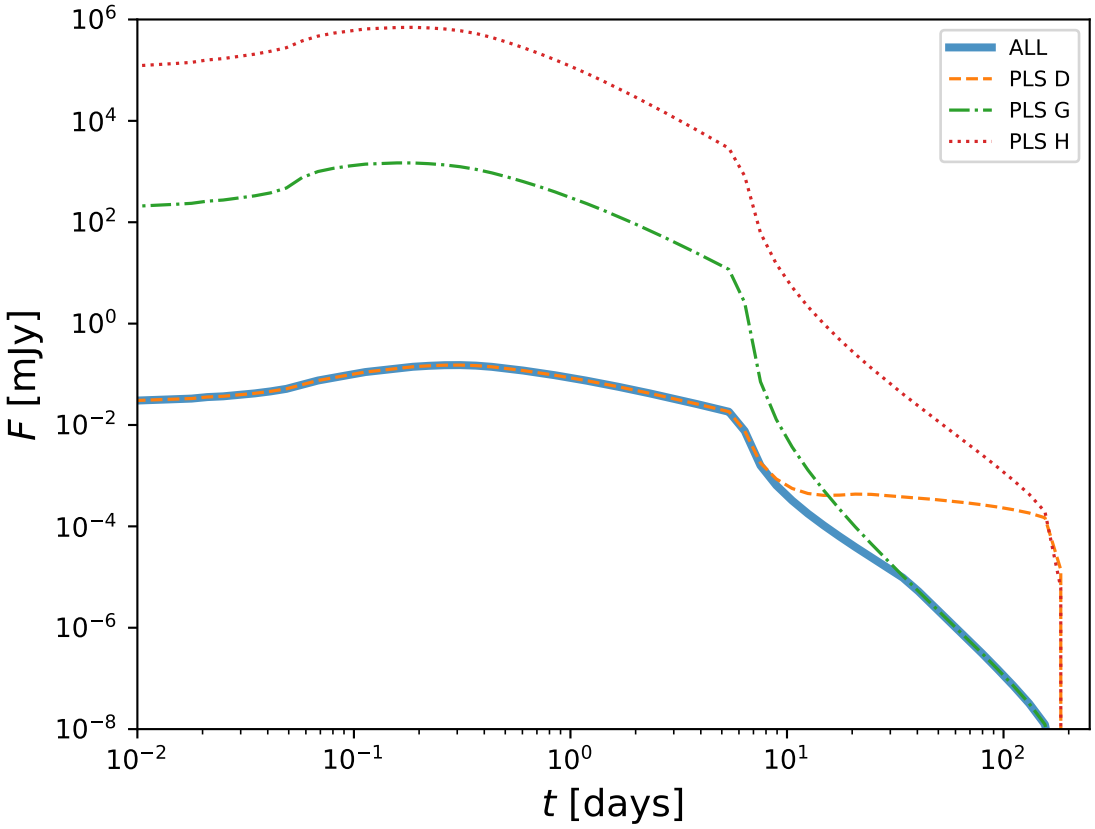

Figure B.1: Afterglow radiation produced by the propagation of a top-hat jet. The light curves were calculated for different power law spectral regions (dashed and dotted lines). The total light curve is denoted by the full continuous line.

times (Granot, 2012; van Eerten & MacFadyen, 2012) as

$$E' = kE, \tag{B.8}$$

$$n' = \lambda n \tag{B.9}$$

$$\frac{t'}{t} = \left(\frac{k}{\lambda}\right)^{1/3}. \tag{B.10}$$

Then, the light curve itself computed for a single simulation can be also be scaled as described by Granot (2012); van Eerten & MacFadyen (2012). This means that trough one single run is possible to describe the light curves of several jet scenarios by a variation of energy ρ and the density of external ambiance ρ.

Bibliography

Aasi J., et al., 2015, Class. Quant. Grav., 32, 074001

Abbott B. P., et al., 2016, Classical and Quantum Gravity, 33, 134001

Abbott B. P., et al., 2017a, Phys. Rev. Lett., 118, 121101

Abbott B. P., et al., 2017b, Phys. Rev. Lett., 119, 161101

Acernese F., et al., 2015, Class. Quant. Grav., 32, 024001

Akiba S., Nakada M., Yamaguchi C., Iwamoto K., 2013, Publications of the Astronomical Society of Japan, 65

Aloy M. A., Janka H.-T., Müller E., 2005, A&A, 436, 273

Aso Y., Michimura Y., Somiya K., Ando M., Miyakawa O., Sekiguchi T., Tatsumi D., Yamamoto H., 2013, Phys. Rev. D, 88, 043007

Baiotti L., Giacomazzo B., Rezzolla L., 2008, PRD, 78, 084033

Batta A., Lee W. H., 2013, Monthly Notices of the Royal Astronomical Society, 437, 2412

Becerra R. L., et al., 2019, The Astrophysical Journal, 887, 254

Becerra R. L., et al., 2021, The Astrophysical Journal, 908, 39

Begelman M. C., Cioffi D. F., 1989, APJL, 345, L21

Beniamini P., Granot J., Gill R., 2020, Monthly Notices of the Royal Astronomical Society, 493, 3521

Berger E., 2014, ARAA, 52, 43

Birnholtz O., Piran T., 2013, PRD, 87, 123007

Blandford R. D., McKee C. F., 1976, Physics of Fluids, 19, 1130

Blandford R. D., Znajek R. L., 1977, Monthly Notices of the Royal Astronomical Society, 179, 433

Braginskii V. B., Thorne K. S., 1987, NATURE, 327, 123

Bromberg O., Nakar E., Piran T., 2011a, The Astrophysical Journal, 739, L55

Bromberg O., Nakar E., Piran T., Sari R., 2011b, APJ, 740, 100

Bromberg O., Tchekhovskoy A., Gottlieb O., Nakar E., Piran T., 2018, MNRAS, 475, 2971

Campana S., et al., 2006, NATURE, 442, 1008

Cano Z., Wang S.-Q., Dai Z.-G., Wu X.-F., 2017, Advances in Astronomy, 2017, 8929054

Cao X.-F., Yu Y.-W., Cheng K. S., Zheng X.-P., 2011, Monthly Notices of the Royal Astronomical Society, 416, 2174

Ciolfi R., 2020, Frontiers in Astronomy and Space Sciences, 7, 27

Ciolfi R., Kastaun W., Giacomazzo B., Endrizzi A., Siegel D. M., Perna R., 2017, PRD, 95, 063016

Combi L., Siegel D., 2022, arXiv e-prints, p. arXiv:2206.03618

De Colle F., Lu W., 2020, NAR, 89, 101538

De Colle F., Granot J., López-Cámara D., Ramirez-Ruiz E., 2012a, APJ, 746, 122

De Colle F., Guillochon J., Naiman J., Ramirez-Ruiz E., 2012b, APJ, 760, 103

De Colle F., Lu W., Kumar P., Ramirez-Ruiz E., Smoot G., 2018a, MNRAS, 478, 4553

De Colle F., Kumar P., Aguilera-Dena D. R., 2018b, APJ, 863, 32

De Colle F., Kumar P., Hoeflich P., 2021, arXiv e-prints, p. arXiv:2105.09376

Dean C., Fernández R., Metzger B. D., 2021, Astrophys. J., 921, 161

Desai D., Siegel D. M., Metzger B. D., 2022, APJ, 931, 104

Dessart L., Ott C. D., Burrows A., Rosswog S., Livne E., 2009, APJ, 690, 1681

Du S., Li X.-D., Hu Y.-M., Peng F.-K., Li M., 2018, Monthly Notices of the Royal Astronomical Society, 480, 402

Dudi R., et al., 2021, Investigating GW190425 with numerical-relativity simulations (arXiv:2109.04063)

Duffell P. C., Quataert E., MacFadyen A. I., 2015, APJ, 813, 64

Duffell P. C., Quataert E., Kasen D., Klion H., 2018, APJ, 866, 3

Eisenberg M., Gottlieb O., Nakar E., 2022, arXiv e-prints, p. arXiv:2201.08432

Foucart F., Moesta P., Ramirez T., Wright A. J., Darbha S., Kasen D., 2021, Phys. Rev. D, 104, 123010

Frail D. A., Kulkarni S. R., Nicastro L., Feroci M., Taylor G. B., 1997, Nature, 389, 261

Frail D. A., et al., 2001, APJL, 562, L55

Fryer C. L., Holz D. E., Hughes S. A., 2002, The Astrophysical Journal, 565, 430

Galama T. J., et al., 1998, NATURE, 395, 670

Gao H.-X., et al., 2022a, Monthly Notices of the Royal Astronomical Society, 516, 453

Gao H., Lei W.-H., Zhu Z.-P., 2022b, APJL, 934, L12

Gehrels N., Ramirez-Ruiz E., Fox D. B., 2009, ARAA, 47, 567

Ghirlanda G., et al., 2019, Science, 363, 968

Gill R., Granot J., 2018, MNRAS s, 478, 4128

Gill R., Granot J., De Colle F., Urrutia G., 2019, APJ, 883, 15

Gottlieb O., Nakar E., 2021, arXiv e-prints, p. arXiv:2106.03860

Gottlieb O., Nakar E., Piran T., Hotokezaka K., 2018a, Monthly Notices of the Royal Astronomical Society

Gottlieb O., Nakar E., Piran T., Hotokezaka K., 2018b, MNRAS, 479, 588

Gottlieb O., Nakar E., Piran T., 2019, Monthly Notices of the Royal Astronomical Society, 488, 2405

Gottlieb O., Levinson A., Nakar E., 2020a, Monthly Notices of the Royal Astronomical Society, 495, 570

Gottlieb O., Bromberg O., Singh C. B., Nakar E., 2020b, MNRAS, 498, 3320

Gottlieb O., Nakar E., Bromberg O., 2020c, Monthly Notices of the Royal Astronomical Society, 500, 3511

Gottlieb O., Liska M., Tchekhovskoy A., Bromberg O., Lalakos A., Giannios D., Mösta P., 2022a, arXiv e-prints, p. arXiv:2204.12501

Gottlieb O., Lalakos A., Bromberg O., Liska M., Tchekhovskoy A., 2022b, Monthly Notices of the Royal Astronomical Society, 510, 4962

Gottlieb O., Moseley S., Ramirez-Aguilar T., Murguia-Berthier A., Liska M., Tchekhovskoy A., 2022c, The Astrophysical Journal Letters, 933, L2

Granot J., 2005, The Astrophysical Journal, 631, 1022

Granot J., 2012, MNRAS, 421, 2610

Granot J., Kumar P., 2003, The Astrophysical Journal, 591, 1086

Granot J., Ramirez-Ruiz E., 2010, arXiv e-prints, p. arXiv:1012.5101

Granot J., Sari R., 2002, The Astrophysical Journal, 568, 820

Granot J., Gill R., Guetta D., De Colle F., 2018, MNRAS, 481, 1597

Hamidani H., Kiuchi K., Ioka K., 2020, MNRAS, 491, 3192

Harrison R., Gottlieb O., Nakar E., 2018, Monthly Notices of the Royal Astronomical Society, 477, 2128

Harten A., 1983, Journal of Computational Physics, 49, 357

Hild S., et al., 2011, Class. Quant. Grav., 28, 094013

Hiramatsu T., Kotake K., Kudoh H., Taruya A., 2005, Monthly Notices of the Royal Astronomical Society, 364, 1063

Hjorth J., Bloom J. S., 2012, The GRB–supernova connection. Cambridge University Press, p. 169–190, doi:10.1017/CBO9780511980336.010

Hjorth J., et al., 2003, NATURE, 423, 847

Holcomb C., Ramirez-Ruiz E., De Colle F., Montes G., 2014, APJL, 790, L3

Hübner M., Talbot C., Lasky P. D., Thrane E., 2020, Phys. Rev. D, 101, 023011

Irwin C. M., Nakar E., Piran T., 2019, MNRAS, 489, 2844

Janiuk A., James B., Palit I., 2021, The Astrophysical Journal, 917, 102

Kathirgamaraju A., Barniol Duran R., Giannios D., 2017, Monthly Notices of the Royal Astronomical Society: Letters, 473, L121

Kathirgamaraju A., Tchekhovskoy A., Giannios D., Barniol Duran R., 2019, MNRAS, 484, L98

Keppens R., Meliani Z., van der Holst B., Casse F., 2008, A&A, 486, 663

Kimura S. S., 2022, arXiv e-prints, p. arXiv:2202.06480

Komissarov S. S., Barkov M. V., 2007, Monthly Notices of the Royal Astronomical Society, 382, 1029

Komissarov S. S., Barkov M. V., Vlahakis N., Königl A., 2007, Monthly Notices of the Royal Astronomical Society, 380, 51

Kotake K., Sato K., Takahashi K., 2006, Reports on Progress in Physics, 69, 971

Kotake K., Takiwaki T., Harikae S., 2012, The Astrophysical Journal, 755, 84

Kullmann I., Goriely S., Just O., Ardevol-Pulpillo R., Bauswein A., Janka H. T., 2022, MNRAS, 510, 2804

Kumar P., Granot J., 2003, APJ, 591, 1075

Kumar P., Zhang B., 2015, PhysRep, 561, 1

Lamb G. P., Kobayashi S., 2018, Monthly Notices of the Royal Astronomical Society, 478, 733

Lamb G. P., et al., 2019, The Astrophysical Journal, 883, 48

Lazzati D., Perna R., 2019, The Astrophysical Journal, 881, 89

Lazzati D., Morsony B. J., Begelman M. C., 2010, The Astrophysical Journal, 717, 239

Lazzati D., Morsony B. J., López-Cámara D., 2015, Journal of High Energy Astrophysics, 7, 17

Lazzati D., Perna R., Morsony B. J., Lopez-Camara D., Cantiello M., Ciolfi R., Giacomazzo B., Workman J. C., 2018, PRL, 120, 241103

Lazzati D., Ciolfi R., Perna R., 2020, The Astrophysical Journal, 898, 59

Lazzati D., Perna R., Ciolfi R., Giacomazzo B., López-Cámara D., Morsony B., 2021, The Astrophysical Journal Letters, 918, L6

Lee W. H., Ramirez-Ruiz E., 2007, New Journal of Physics, 9, 17

Lee W. H., Ramirez-Ruiz E., Page D., 2005, APJ, 632, 421

Leiderschneider E., Piran T., 2021a, Physical Review D, 104

Leiderschneider E., Piran T., 2021b, PRD, 104, 104002

Levan A., 2018, Gamma-Ray Bursts. 2514-3433, IOP Publishing, doi:10.1088/2514-3433/aae164, https://dx.doi.org/10.1088/2514-3433/aae164

Levan A. J., et al., 2013, The Astrophysical Journal, 781, 13

Levan A., Crowther P., de Grijs R., Langer N., Xu D., Yoon S.-C., 2016, SSR, 202, 33

Lopez-Camara D., Lee W. H., Ramirez-Ruiz E., 2009, APJ, 692, 804

López-Cámara D., Morsony B. J., Begelman M. C., Lazzati D., 2013, APJ, 767, 19

López-Cámara D., Morsony B. J., Lazzati D., 2014, MNRAS, 442, 2202

López-Cámara D., Lazzati D., Morsony B. J., 2016, APJ, 826, 180

MacFadyen A. I., Woosley S. E., 1999a, APJ, 524, 262

MacFadyen A. I., Woosley S. E., 1999b, The Astrophysical Journal, 524, 262

Makhathini S., et al., 2020, arXiv e-prints, p. arXiv:2006.02382

Malesani D., et al., 2004, APJL, 609, L5

Margutti R., et al., 2013, The Astrophysical Journal, 778, 18

Margutti R., et al., 2014, The Astrophysical Journal, 797, 107

Margutti R., et al., 2018, The Astrophysical Journal, 856, L18

Martí J. M., Perucho M., Gómez J. L., 2016, The Astrophysical Journal, 831, 163

Matsumoto J., Masada Y., 2013, The Astrophysical Journal, 772, L1

Matsumoto J., Masada Y., 2019, Monthly Notices of the Royal Astronomical Society, 490, 4271

Matsumoto J., Komissarov S. S., Gourgouliatos K. N., 2021, MNRAS, 503, 4918

Matzner C. D., 2003, MNRAS, 345, 575

Maund J. R., Wheeler J. C., Patat F., Baade D., Wang L., Höflich P., 2007, MANRAS, 381, 201

McKinney J. C., Tchekhovskoy A., Blandford R. D., 2012, Monthly Notices of the Royal Astronomical Society, 423, 3083

Mesler R. A., Pihlström Y. M., Taylor G. B., Granot J., 2012, APJ, 759, 4

Mészáros P., Gehrels N., 2012, Research in Astronomy and Astrophysics, 12, 1139

Mészáros A., Bagoly Z., Horváth I., Balázs L. G., Vavrek R., 2000, APJ, 539, 98

Metzger B. D., Margalit B., Kasen D., Quataert E., 2015, Monthly Notices of the Royal Astronomical Society, 454, 3311

Mezzacappa A., et al., 2020, Phys. Rev. D, 102, 023027

Mignone A., Bodo G., 2005, Monthly Notices of the Royal Astronomical Society, 364, 126

Mignone A., Ugliano M., Bodo G., 2009, Monthly Notices of the Royal Astronomical Society, 393, 1141

Mignone A., Striani E., Tavani M., Ferrari A., 2013, Monthly Notices of the Royal Astronomical Society, 436, 1102

Milisavljevic D., et al., 2015, The Astrophysical Journal, 799, 51

Mizuta A., Ioka K., 2013, The Astrophysical Journal, 777, 162

Mooley K. P., et al., 2018, Nature, 561, 355

Moore C. J., Cole R. H., Berry C. P. L., 2015, Class. Quant. Grav., 32, 015014

Morsony B. J., Lazzati D., Begelman M. C., 2007, APJ, 665, 569

Müller E., Janka H. T., Wongwathanarat A., 2012, AAP, 537, A63

Murguia-Berthier A., Montes G., Ramirez-Ruiz E., De Colle F., Lee W. H., 2014, APJL, 788, L8

Murguia-Berthier A., et al., 2017a, APJL, 835, L34

Murguia-Berthier A., et al., 2017b, APJL, 848, L34

Murguia-Berthier A., Ramirez-Ruiz E., Colle F. D., Janiuk A., Rosswog S., Lee W. H., 2021a, The Astrophysical Journal, 908, 152

Murguia-Berthier A., et al., 2021b, APJ, 919, 95

Murphy J. W., Ott C. D., Burrows A., 2009, APJ, 707, 1173

Müller B., Janka H.-T., Marek A., 2013, The Astrophysical Journal, 766, 43

Nakar E., 2007, Physics Reports, 442, 166

Nakar E., Piran T., 2016, The Astrophysical Journal, 834, 28

Nakar E., Sari R., 2012, The Astrophysical Journal, 747, 88

Nakar E., Gottlieb O., Piran T., Kasliwal M. M., Hallinan G., 2018, APJ, 867, 18

Nathanail A., Gill R., Porth O., Fromm C. M., Rezzolla L., 2020, arXiv e-prints, p. arXiv:2009.09714

Nativi L., Lamb G. P., Rosswog S., Lundman C., Kowal G., 2021, Monthly Notices of the Royal Astronomical Society, 509, 903

Panaitescu A., Kumar P., 2000, APJ, 543, 66

Papish O., Soker N., 2014, Monthly Notices of the Royal Astronomical Society, 443, 664

Pavan A., Ciolfi R., Kalinani J. V., Mignone A., 2021, Monthly Notices of the Royal Astronomical Society, 506, 3483

Perego A., Rosswog S., Cabezón R. M., Korobkin O., Käppeli R., Arcones A., Liebendörfer M., 2014, MNRAS, 443, 3134

Perley D. A., et al., 2014, APJ, 781, 37

Pian E., et al., 2006a, NATURE, 442, 1011

Pian E., et al., 2006b, NATURE, 442, 1011

Piran T., 1999, Physics Reports, 314, 575

Piran T., Nakar E., Mazzali P., Pian E., 2019, The Astrophysical Journal, 871, L25

Powell J., Müller B., 2019, Monthly Notices of the Royal Astronomical Society, 487, 1178

Qian Y.-Z., Woosley S. E., 1996, The Astrophysical Journal, 471, 331

Ramirez-Ruiz E., Celotti A., Rees M. J., 2002, MNRAS, 337, 1349

Ramirez-Ruiz E., Andrews J. J., Schrøder S. L., 2019, ApjL, 883, L6

Rezzolla L., Giacomazzo B., Baiotti L., Granot J., Kouveliotou C., Aloy M. A., 2011, APJL, 732, L6

Richardson C. J., Zanolin M., Andresen H., Szczepań czyk M. J., Gill K., Wongwathanarat A., 2022, Physical Review D, 105

Rosswog S., Liebendörfer M., 2003, MNRAS, 342, 673

Rosswog S., Ramirez-Ruiz E., 2002a, Monthly Notices of the Royal Astronomical Society, 336, L7

Rosswog S., Ramirez-Ruiz E., 2002b, MNRAS, 336, L7

Rosswog S., Ramirez-Ruiz E., 2003, MNRAS, 343, L36

Rosswog S., Ramirez-Ruiz E., Davies M. B., 2003, MNRAS, 345, 1077

Ryu D., Chattopadhyay I., Choi E., 2006, The Astrophysical Journal Supplement Series, 166, 410

Sago N., Ioka K., Nakamura T., Yamazaki R., 2004, Physical Review D, 70

Salafia O. S., Ghirlanda G., 2022, arXiv e-prints, p. arXiv:2206.11088

Salafia, O. S. Barbieri, C. Ascenzi, S. Toffano, M. 2020, A&A, 636, A105

Salafia O. S., Ghisellini G., Pescalli A., Ghirlanda G., Nappo F., 2015, Monthly Notices of the Royal Astronomical Society, 450, 3549

Salafia O. S., Ghisellini G., Pescalli A., Ghirland a G., Nappo F., 2016, MNRAS, 461, 3607

Santana R., Barniol Duran R., Kumar P., 2014, APJ, 785, 29

Sari R., Piran T., Narayan R., 1998, The Astrophysical Journal, 497, L17

Sathyaprakash B. S., Schutz B. F., 2009, Living Rev. Rel., 12, 2

Schneider V., Katscher U., Rischke D., Waldhauser B., Maruhn J., Munz C.-D., 1993, Journal of Computational Physics, 105, 92

Segalis E. B., Ori A., 2001, Physical Review D, 64

Shibata M., Taniguchi K., 2006, PRD, 73, 064027

Siegel D. M., Ciolfi R., Rezzolla L., 2014, APJL, 785, L6

Soderberg A. M., Nakar E., Berger E., Kulkarni S. R., 2006, The Astrophysical Journal, 638, 930

Soderberg A. M., et al., 2010, NATURE, 463, 513

Soker N., 2022, arXiv e-prints, p. arXiv:2205.09560

Starling R. L. C., et al., 2011, Monthly Notices of the Royal Astronomical Society, 411, 2792

Sun M.-Y., Liu T., Gu W.-M., Lu J.-F., 2012, The Astrophysical Journal, 752, 31

Suwa Y., Murase K., 2009, Phys. Rev. D, 80, 123008

Suzuki A., Maeda K., 2022, APJ, 925, 148

Szczepańczyk M. J., et al., 2021, PRD, 104, 102002

Takahashi K., Ioka K., 2020, Monthly Notices of the Royal Astronomical Society, 497, 1217–1235

Takahashi K., Ioka K., 2021, MNRAS, 501, 5746

Tanaka M., Maeda K., Mazzali P. A., Kawabata K. S., Nomoto K., 2017, The Astrophysical Journal, 837, 105

Taub A. H., 1948, Phys. Rev., 74, 328

Taubenberger S., et al., 2009, Monthly Notices of the Royal Astronomical Society, 397, 677

Taylor P. A., Miller J. C., Podsiadlowski P., 2011, Monthly Notices of the Royal Astronomical Society, 410, 2385

Thorne K. S., 1973, APJ, 179, 897

Troja E., et al., 2018, Monthly Notices of the Royal Astronomical Society: Letters, 478, L18

Troja E., et al., 2022, arXiv e-prints, p. arXiv:2209.03363

Urrutia G., De Colle F., Murguia-Berthier A., Ramirez-Ruiz E., 2021, Monthly Notices of the Royal Astronomical Society, 503, 4363

Urrutia G., De Colle F., López-Cámara D., 2022a, Three-dimensional numerical simulations of structured GRB jets, doi:10.48550/ARXIV.2207.07925, https://arxiv.org/abs/2207.07925

Urrutia G., De Colle F., Moreno C., Zanolin M., 2022b, arXiv e-prints, p. arXiv:2208.00129

Vink J. S., 2011, APSS, 336, 163

Walg S., Achterberg A., Markoff S., Keppens R., Meliani Z., 2013, Monthly Notices of the Royal Astronomical Society, 433, 1453

Wanderman D., Piran T., 2010, Monthly Notices of the Royal Astronomical Society, 406, 1944

Wang P., Abel T., Zhang W., 2008, The Astrophysical Journal Supplement Series, 176, 467

Wongwathanarat, A. Müller, E. Janka, H.-Th. 2015, A&A, 577, A48

Woosley S. E., 1993, APJ, 405, 273

Woosley S. E., Heger A., 2006, The Astrophysical Journal, 637, 914

Wu Y., MacFadyen A., 2019, The Astrophysical Journal, 880, L23

Xie X., Zrake J., MacFadyen A., 2018, The Astrophysical Journal, 863, 58

Yagi K., Seto N., 2011, Phys. Rev. D, 83, 044011

Yakunin K. N., et al., 2015, Phys. Rev. D, 92, 084040

Yu Y.-W., 2020, The Astrophysical Journal, 897, 19

Zhang W., MacFadyen A., 2009, APJ, 698, 1261

van Eerten H. J., MacFadyen A. I., 2012, APJL, 747, L30